Mechanical Properties of Soft Interfaces

A DISSERTATION
SUBMITTED TO THE FACULTY OF THE GRADUATE SCHOOL
OF THE UNIVERSITY OF MINNESOTA
BY

Matthew Goertz

IN PARTIAL FULFILLMENT OF THE REQUIREMENTS
FOR THE DEGREE OF
DOCTOR OF PHILOSOPHY

Xiaoyang Zhu Advisor

April 2009

Acknowledgments

I would like to first thank my advisor, Dr. Xiaoyang Zhu. Not only has his knowledge and expertise been key in my success as a graduate student, his constant quest for discovery has been a daily refresher and motivator. I would also like to thank Dr. Jack Houston for giving me the opportunity to work with him at Sandia National Labs. It is not often that one gets to work with the inventor of the scientific equipment they use on a daily basis. Jack's guidance with both the unique technical issues of the IFM and with the underlying physics of thin films and soft interfaces has helped me immensely. I am also grateful for the opportunity to work with Dr. Ben Stottrup. Ben's expertise in physics of lipids has broadened my horizons into the world of biophysics. In the few short years we worked together I have observed Ben's passion for his work and will certainly try to mimic that in my career. The daily support, both intellectually and motivationally of the fellow Zhu group members has always helped me through the rough stretches of graduate school. Finally, I am extremely indebted to my parents and my wife whose support throughout my entire education has been invaluable.

Abstract

As the trend of miniaturization in devices and systems continues, it is important to understand their mechanical properties at the nanometer scale. In Micro-Electro-Mechanical Systems (MEMs) and implantable biomedical devices, interfacial forces (friction and adhesions) responsible for device failure are a major concern. Molecular films as thin as a monolayer are being actively explored to reduce adhesion and friction. However, many questions remain about the tribological properties of these systems.

This thesis summarized the use of Interfacial Force Microscopy allows us to reliably create single asperity contacts and study the associated tribological properties on the nano and microscale. We have used this tool to study the mechanical properties of confinement of molecular films, including water, liquid-like-layer (on ice), alkyl monolayers, and phospholipid monolayers and bilayers. We find that the interfacial water created by premelting of ice or nanoconfinement between hydrophilic surfaces exhibit significant increase in viscosity. In the cases of alkyl or phospholipid thin films, mechanical properties, particularly friction, are strong functions of film structure and density. Results from these model systems are starting to form a foundation for our understanding of mechanical properties of soft interfaces at the nanometer scale.

Table of Contents

List of Figures

List of Tables

Chapter 1. Introduction

1.1 Motivation

Studying the mechanical properties of soft surfaces and interfaces has been going on for many years. However, only in the last ~20 years has the invention of scanning probe techniques allowed for the creation of single asperity contacts to study these interfaces on the molecular level. By first understanding the properties of each single asperity contact we can begin to understand the response of a macroscale interface, which usually involves multiple asperity contacts. The work in this thesis summarizes the use of the Interfacial Force Microscope (IFM)[1,2] to create single asperity contact of a hard probe with a soft material, such as water or a thin film of phospholipids.

One underlying question that motivates this work is the comparison of nanoscale material properties to bulk properties. At times this is a difficult question to answer as ultra-thin films such as self assembled monolayers often do not possess a comparable bulk phase. Further complicating analysis is the lack of appropriate models to extract properties such as elastic modulus, yield stress, viscosity and friction. While models may work well for larger contacts, they usually break down on the nanoscopic level, but this is the area we are most interested in. Because of this, it is often quite useful to compare results obtained by scanning probe instruments to those obtained through other techniques such as spectroscopy, simulation and theory. These techniques can be quite surface sensitive and offer information on the physical properties, usually changes in bonding, that contribute

to any differences between nanoscale and bulk mechanical properties. One example of this is the work on interfacial water (Chapter 3). In this work, I found that the viscosity of a few monolayers of water confined between two hydrophilic surfaces was ~10^6 larger than that of bulk water. This was verified by spectroscopy and simulation, which showed that water molecules on a hydrophilic surface had bonding similar to that of ice.[3]

Understanding the mechanical properties of soft interfaces is becoming increasingly relevant for designing reliable nanoscale and microscale devices. As mechanical devices scale down to smaller sizes, the forces that cause them to fail also scale down. At these size scales, sliding friction, stiction (static friction) and adhesion often limit the reliability of moving parts. Fortunately the use of boundary lubricants, even as thin as one monolayer, can improve device performance.

Microscale devices with moving parts such as Microelectromechanical systems (MEMS) are actively being researched for use in a wide range of fields.[4] Common examples of MEMS are accelerometers, inkjet printers and optical displays. These devices are usually made from sacrificial etching of polycrystalline silicon or aluminum and have very large surface area to volume ratios. Translation and rotational motion of parts in these devices is usually accomplished through the use of electrostatic motors that drive a series of gear and spring elements. If the forces generated by the motor cannot overcome surface forces, the part becomes stuck and the device has effectively failed. The most common cause of stiction and adhesion in a MEMS device is the capillary force on the hydrophilic native oxide of

silicon and is usually reduced by use of a soft hydrophobic boundary lubricant. These lubricants are also used to reduce the friction of interlocking asperities of rough sliding surfaces in MEMS.[5] Unfortunately thin film boundary lubricants often exhibit wear and the lubricants fail after repeated stressing. Knowing how much stress these lubricants can take before failing highlights the importance of understanding the mechanical properties of soft interfaces. Recently there has also been much research into improving the wear properties of boundary lubricants by ultrahard films such as diamond-like carbon[6] and by self-healing soft boundary lubricants.[7]

Devices with soft interfaces, but without moving parts are also being actively studied. These technologies include, but are not limited to, bio-membranes, lab-on-a-chip devices, polymers, self assembled monolayers (SAMs) and liquid interfaces. As with the boundary lubricants for hard contacts mentioned above, understanding the mechanical properties of these systems is essential to designing better devices.

In this thesis, I focus on simple models for complex soft systems. An example of this is supported lipid monolayers and bilayers (SLBs) as models of a cell membrane[8] (Chapters 5&6). Cell membranes are dynamic composite fluids that form a barrier for the contents of the cell and act as a host to a variety of biomolecules.[9] By varying the deposition condition and length of the phospholipid alkyl-chain tails, I was able to form both 2-d gel and fluid phase films and correlate their mechanical properties (elastic modulus, plastic threshold and friction

properties) with structure of the films. While these results oversimplify the mechanics of a real cell membrane, they are essential for designing devices that mimic this membrane such as lab-on-a-chip devices and protein microarrays. In these devices, transmembrane proteins are often imbedded in supported lipid films to maintaining their activity. [10] Understanding the mechanics of SLBs helps to create these biosensing devices that are stable under a wide range of environmental conditions and resist dehydration and delamination.

Beyond making useful devices, soft interfaces can be used as models to study the origins of surface forces on the molecular level. By creating well defined surfaces one can begin to understand the nature of adhesion, friction, wear, plasticity and elastic properties at nanometer separations. While understanding these forces is a common theme to this thesis, my study of the density dependent friction of lipid monolayers (Chapter 5) highlights one method of determining the molecular origins of friction. In this work, I systematically varied the packing density of Langmuir-Blodgett (LB) deposited lipid monolayers and measured the amount of friction per unit area of contact. The results showed that as the packing density of the lipid films decreased the friction increased. This helped verify the theory that the major energy dissipation process creating friction in boundary lubricants with alkyl chains is the ability to form intramolecular trans to gauche defects.[11] While this had been previously observed with chemisorbed SAMs, my use of LB monolayers expanded the range of packing densities that could be studied. Packing density of chemisorbed SAMs such as alkanethiols on Au is

controlled by the headgroup/surface bonding and van der Waals forces between neighboring alkyl chains. In contrast, LB films can be deposited over a wide range of packing densities by simply changing the surface pressure at the air/LB film/water interface.

By far the most common tools used to probe soft interfaces are spring based cantilever instruments such as the Atomic Force Microscope (AFM)[12] and the Surfaces Forces Apparatus (SFA).[13] These devices quantify force applied to a probe by measuring the displacement of a spring and multiplying the displacement by the spring constant of the cantilever. While the AFM often uses nanometer size probes, the SFA uses two crossed mica cylinders as contacts with contact area approaching $1cm^2$. As a result, the AFM excels at measuring forces down to picoNewtons (using advanced dynamic techniques)[14] and imaging surfaces at the nanometer level. This is in comparison to the SFA which cannot image surfaces and is limited to mica surfaces that are atomically flat on the size scale of the contacts used. While these tools are extremely useful in measuring surface forces, problems are encountered when one attempts to measure adhesive forces. When the adhesive force applied to a spring cantilever overcomes the spring restoring force there is a mechanical instability and the two surfaces uncontrollably jump into contact. The opposite of this process is repeated as the two surfaces are separated. When the spring restoring force overcomes the adhesions, the two surfaces are uncontrollably separated. It is customary to use the maximum adhesive force when the two surfaces are separated ("pull-off-force") to characterize the adhesion between the surfaces. Fortunately the

force-feedback scheme used by the IFM creates an effectively compliance free sensor that is able to measure both adhesive and repulsive forces without any mechanical instabilities. The IFM allows for the true work of adhesion for removing two surfaces from each other to be calculated by integrating the adhesive portion of a force curve. This is in contrast to using the "pull-off-force" and contact mechanics to estimate the work of adhesion per unit area.

1.2 Surface Forces

The work in this thesis primarily uses the measurement of surface forces to characterize the mechanical properties of soft interfaces. While this thesis is not meant to be an extensive review of surface forces, I will now discuss a few common forces and there origins. Readers should see the works of Israelachvili,[15] Persson,[16] Bowden[17] and Butt[18] for extensive reviews and derivation of these force laws.

Non-contact adhesive forces usually result from at least one of three possible sources: van der Waals, electrostatic, and capillary. These forces can be distinguished by their force (F) vs. distance (d) behavior. For a sphere on plate geometry, as commonly used with scanning probe microscopes, van der Waals forces[15] follow:

$$F = -\frac{A}{6R(d - d_0)^2} \qquad 1.1$$

where A is the combined Hamaker Constant for the system, R is the tip radius and d_0 is the point of contact. Electrostatic forces[19] can be estimated from the Derjaguin approximation[20] as:

$$F = -\frac{2\pi R K \varepsilon_0 V^2}{(d - d_0)} \qquad 1.2$$

where K is the dielectric constant of the material between the surfaces, V is the potential difference of the surfaces and ε_0 is the free-space permittivity. Finally capillary forces,[15] while in thermodynamic and mechanical equilibrium, follow:

$$F = -\frac{4\pi R \gamma_{LV} \cos(\theta)}{\left(1 + \frac{d}{h}\right)} \qquad 1.3$$

where γ_{LV} is the surface tension of the liquid, θ is the contact angle of the liquid on the probe and h is the height of the liquid on the probe. Capillary forces occur from both the Laplace pressure[15] inside the curved meniscus and the surface tension at the vapor/liquid/probe contact line. Out of these two contributions, usually the Laplace pressure dominates. Unfortunately, it is rarely the case that capillary condensate is in equilibrium and significant hysteresis is observed between approach and retraction force curves. Finally there is still significant debate about adhesive "hydrophobic" forces. This is seen as two hydrophobic surfaces approach each other while underwater.[21] At micrometer to nanometer separations the confined water can undergo cavitation to form unstable bubbles that lead to adhesive forces.

Of course, not all non-contact forces are attractive. Non-contact repulsive forces can also have several origins such steric hindrance,[15] solvation forces,[15] electrostatic repulsion and viscous drainage. Steric hindrance occurs when two polymer covered surfaces come into contact. Upon compression, the polymers are forced to occupy the same space leading to entanglement and removal of polymer

solvent. Solvation forces occur between two surfaces that are wetted with a good solvent, such as hydrophilic polymer surfaces in water. As the two surfaces approach the equilibrium, molecular structure of the solvent near the two surfaces is disrupted. The energy it takes to do this process creates a repulsive force. Electrostatic repulsion follows the same force laws as electrostatic attraction, but with two similarly charged surfaces. The only not-contact repulsive force that is speed dependent is viscous drainage.[22] As two surfaces approach each other in a viscous fluid there is a speed dependent force required to squeeze out the interfacial fluid. The force vs. distance relationship for drainage for a fluid of constant viscosity (η) at a constant speed (ν) is:

$$F = \frac{6\pi\eta\upsilon R^2}{d} \qquad 1.4.$$

For a thin viscous film the equations of Feibelman[23] are more appropriate, these equations have proved useful in my analysis of the viscosity of interfacial water (Chapter 3). Finally, it is often found that non-contact forces are a sum of many of these forces and it may be difficult to isolate the magnitude of each component. One can understand the sources of these forces from knowledge of the two contact surfaces and dependences of forces on experimental variables, such as approach speed, relative humidity and contact potential difference.

Once contact is made between the probe and substrate, one relies on contact mechanics to describe the force vs. distance relationship. The simplest model of contact mechanics is the Hertz model[24] which describes elastic interaction and does

not account for any probe-sample adhesion. According to this model the force depends on the penetration depth (*h*) and the reduced modulus (*E**) through:

$$F = E^* h^{\frac{3}{2}} \sqrt{R} \quad 1.5.$$

The reduced modulus, a composite elastic modulus for both probe and sample, is given by:

$$E^* = \frac{3}{4}\left(\frac{1-\upsilon^1}{E^1} + \frac{1-\upsilon^2}{E^2} \right)^{-1} \qquad 1.6.$$

Here *E* and *v* are the elastic modulus and Poisson ratio of each respective material. When using a probe that has a much higher elastic modulus than the sample, most of the deformation occurs in the sample and the reduced modulus is a fair approximation of the sample only. Common probe materials include Tungsten, diamond, Silicon and Silicon Nitride.

There are two widely used models that extend the Hertz model to account for probe-sample adhesion. The Johnson, Kendall, Roberts[25] (JKR) model accounts only for adhesion within the contact area and allows for probe/sample deformation because of this adhesion. The Derjaguin, Muller, Toropov[20] (DMT) model accounts for only non-contact adhesion and does not allow for deformation from the adhesion. While there are models that treat conditions between JKR and DMT such as the work of Maugis,[26] fitting experimental data with these models is quite cumbersome. It should also be noted that the micron sized tips used with the IFM create conditions where JKR or Hertz theory is often most appropriate. As a rule of

thumb, JKR is appropriate for large soft contacts and DMT works best for small hard contacts. One method to determine which model is appropriate can be found in the work of Carpick[27] where fitting the contact area (or friction) vs. applied load can reveal the appropriate model.

A major problem common to the models above is applying them to thin films. It is generally accepted that these models work well as long as the deformation is less than 10% of the total film thickness. Unfortunately, the thickness of most SAMs is 1-2 nm allowing for contact mechanics to be accurate for only 1-2 Å! Since thin films such as SAMs are often deposited on much harder surfaces, these models usually overestimate the elastic modulus of thin films. The Chadwick[28] model may be able to provide a better estimation of the elastic modulus of thin films. This model implies a constant volume condition for a bonded incompressible elastic film with thickness (t) sandwiched between a rigid (infinite modulus) probe and substrate through the following relationship:

$$F = \frac{2\pi}{3t^3} ER^2 h^3 \qquad 1.7.$$

The limitation of using contact mechanics on nanoscale thin films unfortunately makes comparing results from different experiments fruitless because the probe size can vary over many orders of magnitude. However, using the same technique to compare systems with different properties is usually more rewarding. Further complicating analysis is the roughness of surfaces which can lead to multiple asperity contacts under a much larger stress than predicted through contact

mechanics. Finally, not all forces in contact are repulsive in nature. Once two surfaces touch, wetting of the two surfaces and interfacial bonding can also create adhesion.

Beyond surfaces forces in the direction of the surface normal, I have used the IFM to measure lateral forces such as friction between two interfaces and shearing of a viscous liquid. As mentioned above, friction on the nanoscale level usually involves multiple asperity contact and is characterized by Amonton's "law":[16]

$$F_{\mu} = \mu L \qquad 1.8.$$

While this "law" began as an empirical relationship for the linear response of friction (F_{μ}) to load (L) through the use a friction coefficient (μ), there has been attempts to justify it theoretically. One such theory is that of Bowden and Tabor who took into account plastic deformation of the surfaces.[17] According to this theory the real area of contact (A) is related to the applied load through the yield strength of the material (σ_Y) by:

$$A = \frac{L}{\sigma_Y} \qquad 1.9.$$

They also assume that the friction force is linearly proportional to contact area through the friction shear stress (τ), resulting in:

$$F_{\mu} = A\tau \qquad 1.10.$$

Therefore, once plastic deformation of the contact is occurring, friction vs. load will take a linear relationship. Bowden and Tabor's model also includes plowing of interlocking asperities that may contribute significantly to friction. Another theory is that of Persson[16] who assumed that the real area of contact for macroscale contacts is always linear vs. applied load due to randomly rough surface, again resulting in Amonton behavior. Using various sized tips with the IFM to probe friction, we can probe single and multiple asperity contacts and often use Amontons law or lack there of, to determine the nature of the contact.

Combining contact mechanics and friction measurements allows one to determine the friction shear stress for different materials and to identify the processes that create friction on the molecular level. I have found that it is often of interest to change experimental factors such as temperature, sliding speed and time between cyclic stressing to further explore friction. The later two factors may be explored by using both linescan hysteresis loops and shear modulation to probe friction as outlined in Chapter 7. Both of these methods use the same basic technique to measure lateral forces applied to the IFM probe. When the IFM probe moves laterally an addition torque is applied to the sensor. This torque is proportional the lateral forces and changes sign when the probe reverses direction, creating hysteresis in the total torque applied to the IFM sensor. These two techniques can probe not only sliding friction but also static friction by analyzing data in the time domain. These two types of friction sometimes cannot be decoupled as is the case with slip-stick motion.

As with normal forces, friction forces can also occur out of contact. Such is the case with shear of a liquid between two surfaces. Similar to the aforementioned viscous drainage force, the viscosity of a fluid provides resistance to shear. I have used this technique to measure the viscosity of both fluid films confined between surfaces and the properties of a nanoscale meniscus formed through capillary condensation.[3] The viscosity (η) of a fluid is usually estimated by $\eta = \frac{\tau}{\gamma}$. In this estimation τ is the friction shear stress and γ is the shear rate. As with friction of solids, the friction shear stress is defined as the friction per unit area. While the magnitude of the friction is easy to measure, the area again must be estimated through mechanics. The shear rate also must be estimated, and is often taken to be the sliding rate divided by the interfacial separation. This linear relationship assumes the no-slip boundary condition and may not be true on the nanoscale. Finally, similar to viscous draining, models have been derived by Feibelman[29] to treat the case of probe sliding over a thin film of viscous fluid.

1.3 Brief Review of Publications

Chapters 3-7 of this thesis each encompass a publication of my work on exploring the mechanical properties of soft interfaces. These works begin with two studies on interfaces with water. First I study how water meets a hydrophilic surface such as silicon oxide. In this work I used both viscous drainage and oscillatory shear measurements to probe the properties of interfacial water. I found that water within ~1 nm of a hydrophilic surface exhibits a viscosity increase by ~10^6 times that of bulk water. The increase in viscosity was observed for both a

nanoscale capillary condensate meniscus and for a thin film of water confined between two surfaces. This study also showed that the increase in viscosity is not only due to confinement, as by changing to a hydrophobic surface the increase in viscosity was not observed. My second study on interfacial water explored the so called "liquid-like" layer on the surface of ice. In this work I probed the temperature dependence of the properties of the ice and the "liquid-like" layer created by premelting. Similar to the work on silicon oxide I found that the premelted layer on ice has properties somewhere between that of bulk water and ice, and disappeared at temperature below ~-30°C. Our findings indicate that this layer acts as a lubricant on the macroscale contact with ice, and offers another explanation as why ice is slippery.

Moving on from interfacial water, I have also measured the mechanical properties of several self-assembled thin films. Beginning with supported lipid films, I have studied both monolayers and bilayers of two different phospholipids. These two lipids have the same hydrophilic headgroups and glycerol linkers, only differing in the length of there alkyl tails. The shorter chained lipids tend to form a disordered 2-D fluid phase film at room temperature while the longer chained lipids pack together to form a more ordered 2-D gel. By characterizing the friction, elastic and plastic properties of these films, I am able to correlate their structure and mobility to mechanical properties. Finally, I have studied the mechanical properties of a covalently tethered monolayer, an alkoxy monolayer on silicon. I find that the alkoxy monolayer is able to effectively lubricate and prevent wear of a silicon

surface. This film also shows wear after repeated stressing that decreases the friction, contrary to most wear in which the friction increases.

1.4 References

1 Houston, J.E.; Joyce,S.A. *Rev. Sci. Instrum.* **1991**, *62*, 710.

2 Houston, J.E.,; Michalske, T.A. *Nature* **1992**, *356*, 266-267.

3 Goertz, M. P; Houston J. E; Zhu, X.-Y. *Langmuir* **2007**, *23(10)*, 5491-7.

4 Bhushan, B. *Nanotribology and Nanomechanics an Introduction*; Springer: Hedidelberg, 2005.

5 Dugger, M.T.: Quantification of friction microsystem contacts. In Hsu, S.M., Ying, Z.C (eds.), Nanotribology Critical Assessment and Research Needs, Klower Acedemic Publishers, Boston (2003)

6 Crossley, A.: Johnston, C.; Watson, G.S.; Myhra, S. *Journal of Physics D-Applied Physics.* **1998,** *31*, 1955-1962.

7 Asay, D.B.; Dugger, M.T.; Kim, S.H. *Tribol. Lett*. **2008**, *29*, 67-74.

8 Brian, A.A.; McConnell, H.M.. *Proc. Natl. Acad. Sci. USA*. **1984**, *81*, 6159-63.

9 Simons, K.; Vaz. W.L.C. *Annu. Rev. Biophys. Biomol. Struct*. **2004**, *33*, 269.

10 Deng, Y.; Wang, Y.;Holtz, B.; Li, J.-Y.; Traaseth, N.; Veglia, G.; Stottrup, B.L.; Pei, D.; Elde, R.; Guo, A.; Zhu, X.-Y. *J. Am. Chem. Soc.* **2008**, *130* 6267-6271.

11 Salmeron, M. *Tribology Lett.* **2001**, *10*, 69.

12 Binnig, G.; Quate, C.F.; Gerber, C. *Phys. Rev. Lett.* **1986** *12*, 930.

13 Israelachvili, J.N. *Chemtracts* **1989**, *1*, 1.

14 Schirmeisen, A.; Anczykowski, B., Fucks, H. Scanning Probe Microscopy. In *Applied Scanning Probe Methods*. Eds. Bushan, B.; Fuchs, H.; Hosaka, S. Springer: New York, NY, 2004.

15 Israelachvili, J. N. *Intermolecular and Surface Forces*; 2nd ed.; Academic Press: San Diego, CA, 1992.

16 Persson, B. N. L. *Sliding Friction: Principles and Applications*; Springer: Berlin, 2000.

17 Bowden, F.P., Tabor, D. *The Friction and Lubrication of Solids*, University Press, Oxford , 2001.

18 Butt, H.-J., *Physics and Chemistry of Interfaces*, Wiley-VCH, Weinheim, 2006.

19 Houston, J.E.: Doelling, C.M.: Vanderlick, T.K., Hu: Y., Scoles, G.: Wenzl, I.: Lee T.R. *Langmuir* **2005**, *21*, 3926-3932.

20 Derjaguin B.V.; Muller V.M.; Toropov, Y.P., *J. Colloid. Interface Sci.* **1975**, *53*, 314.

21 Singh, S.; Houston, J.; van Swol, F.; Brinker, C.J. *Nature* **2006**, *442(*3), 526.

[22] Kim, H.I.; Kushmerick, J.G.; Houston. J.E.; Bunker B.C. *Langmuir* **2003**, *19*, 9271.

23 Feibelman, P. J. *Langmuir* **2003**, *20*, 1239-1244.

24 Hertz, H. J. *Reine Angew. Math*. **1882**, *92*, 156. (in German)

25 Johnson, K.L.; Kendall, K.; Roberts, A.D. *Proc. Roy. Soc. London* **1971**, *A 324*, 301.

26 Maugis D.J., *J. Colloid. Interface Sci*. **1992**, *150*, 243.

27 Carpick, R.W.: Ogletree, D.F.: Salmeron, M.J. *J. Colloid Inter. Sci.* **1999**, *211*, 395.

28 Chadwick, R.S. *SIAM Journal on Applied Mathematics.* **2002**, *62(5)*, 1520-1530.

29 Feibelman, P. J. *Langmuir* **2006**, *22*, 2136-2140.

Chapter 2. The Interfacial Force Microscope

2.1 IFM Design

Developed in the lab of Jack Houston at Sandia National Labs, the IFM is a scanning probe instrument. At the heart of the microscope is the differential capacitance sensor that is able to provide an effectively compliance free element by using feedback. A schematic of the sensor is shown in Fig. 2.1. It consists of an etched silicon top plate bonded to a glass substrate. The glass is etched in a manner to create pit, where the capacitors are formed. The fixed capacitors are created by first depositing an adhesive layer of chromium onto the photo-masked glass plate, followed by a much thicker gold layer. The gold layer acts as the top of the face of the two fixed capacitor pads each with an area of 2500 μm^2 and also as the contact for electrical connections. The common center plate is made from a 100 μm sheet of doped Si(001) that is etched by a Bosch process[1] to create a 25 μm wide trench to define the "teeter-totter." The top plate "teeter-totter" is designed to have a little resistance to rotation around the torsion bar axis, while also having no compliance perpendicular to the axis of rotation. The top silicon plate is then anodically bonded to the glass substrate forming two capacitance gaps of ~5 μm, with a capacitance of around 15 pf. A tip, usually an electrochemically etched wire, is mounted (epoxy-glued) on top of one of the capacitors. If a force is applied to the tip, one of the capacitor gaps narrows and the other widens, depending upon the direction of the applied force.

The main advantage of using a dual capacitor sensor is that it allows balancing any changes in capacitance by an AC bridge. By using a bridge (shown in Fig. 2.2), the IFM acts as a null detector and receives output for the transducer as a change in capacitance versus the total capacitance. This method gives the IFM the ability to detect changes on the order of 1ppm of the total capacitance. This gives a spatial resolution on the Ångstrom level, as a one Å change in the differential capacitor gap creates capacitance change of 2.5 ff or 500 μV (with a 10V bridge voltage), which is detectable by a common lock-in amplifier. The AC bridge voltage is created with a function generator and summed on a DC voltage of 10V. This bridge voltage is fed through RF transformers onto the differential capacitor. The bridge voltage, although tunable, is usually 10 V (peak to peak) at a frequency of 1 MHz. The imbalance of the bridge is measured at the common capacitor plate on an oscilloscope. This imbalance signal is first fed into a high-frequency preamplifier and then into a lock-in amplifier for demodulation. The lock-in amplifier is used for phase sensitive detection of only the in-phase reactive signal and to filter out the out-of-phase resistive component. As with all lock-in amplifiers, the input must be tuned to be in-phase with the reference oscillator. A mechanical variable capacitor between one of the RF transformers and a sensor capacitor is used to balance the stray capacitance and the natural imbalance of the differential-capacitor.

The nulled bridge imbalance the lock-in amplifier is fed into a standard proportional-integral-derivative (PID) feedback controller. As previously stated, any

force on the tip will cause a change in the capacitance gaps, which creates another bridge imbalance. The sign of the bridge imbalance is dependant upon the sign of the net force applied to the tip. This imbalance is countered by a restoring feedback voltage applied to only the capacitor beneath the mounted tip to drive the output of the preamplifier to zero. The sign of the PID feedback voltage is determined by the sign of the net applied force acting on the tip. The PID output voltage is proportional to the net applied normal force acting on the tip and can be calibrated for quantitative measurements.

The sensor is calibrated by a laboratory balance using micrometers. The calibration constant can be found by manually displacing the tip and measuring the PID voltage and applied force with the laboratory balance. This is done by plotting the applied force versus the PID voltage and fitting it to the following equation:

$$F_a \equiv G_f [V_0 \Delta V - \frac{\Delta V^2}{2}] \quad 2.1.$$

Here F_a is the net applied force on the tip in μN, G_f is the gain factor in μN/V^2, V_0 is the 10 V DC voltage that the AC bridge is modulated on top of, and ΔV is the PID voltage. This calibration method commonly gives a G_f value around 1.5 μN/V^2 and a working range of 2nN to 1 mN, with a resolution of 2nN. The feedback loop is comprised of mostly proportional and integral gain to control the response time. I use a function generator to input a 10 Hz square wave into the sensor and find that a response time of fewer than 2ms can be achieved. In addition to the feedback voltage applied by the PID controller, an additional DC voltage (labeled e_c in Fig.

2.2) is used to counter any drift and balance the bridge output with zero applied force.

Currently, the sensor assembly is mounted upside-down on a four quadrant piezoelectric outer tube for coarse vertical and lateral movement and an inner piezoelectric tube for fine vertical movement. A sample is mounted directly below the sensor on a stage with inchworm piezo movement in all directions. This setup allows for x-y raster scan imaging in both contact and tapping mode. Environment control is possible by surrounding the microscope head with a chamber wall and mounting the sample on a thermo-electric device. The entire microscope is mounted on a table with vibration-isolation supports. Surrounding the IFM chamber with sound dampening foam insulation provides further acoustic vibration isolation.

2.2 IFM Methods

A wide range of tribology experiments can be performed with the IFM, from 3-D imaging to material relaxation measurements. The most typical IFM experiment is the force profile. A force profile starts with the tip hovering at a constant load, usually in repulsive contact with a sample. The tip is withdrawn a certain distance and then approaches the sample at a constant rate while the force on the tip is recorded. Once the force reaches a specified limit, the tip retracts back the same distance that it approached. Lateral forces can be measured using the IFM in a much different manner than the AFM[2] or the friction force microscope (FFM).[3] Lateral forces, such as friction, are acquired during a force profile by adding a dither

to the tip in the direction perpendicular to the torsion bar axis of rotation. The frequency and amplitude of the dither can be controlled within the range of the feedback loop. However, care must be taken not to mistake a low frequency modulating lateral force as an actual normal force feature. In order to separate the lateral force from the normal force, we feed the PID voltage into another lock-in amplifier. The internal reference oscillator of the lock-in is sent to a high voltage controller to modulate the outer piezo tube at a specified frequency. The frequency of modulation is usually chosen to be 100 Hz so that a lateral friction force would change sign every 10ms, which is slower than the feedback loop response time. The amplitude of the dither can be controlled from no dither to 9nm. The phase between the driving dither and the lateral force can also be collected from the lock-in amplifier. This allows the in-phase and out-of-phase component can be analyzed separately. Even though methods for analysis of the lateral response phase are not yet fully developed, the phase data is helpful in detailing the interaction between the tip and sample during force profiles as well as material response during creep and relaxation profiles. In the simplest model we can treat the lateral modulation of the tip as a spring element being driven laterally. Forces that are proportional to the acceleration of the tip such as mass effects are 180° out of phase with the drive, while forces that are proportional to the speed such as viscous shear forces are 90° out of phase. Once the static friction force becomes large enough the applied lateral spring restoring force cannot overcome it, the tip becomes stuck and the phase drop to 0°.

The friction force F_μ is calibrated by adding another term to account for the distance of the tip from the center of the torsion bar axis (L_p) and the length of the tip (L_t) giving the form:

$$F_\mu \equiv G_f[V_0\Delta V - \frac{\Delta V^2}{2}]\left(\frac{L_p}{L_t}\right) \quad 2.2.$$

Relaxation and creep profiles are also capable of being performed with the IFM. In a relaxation profile, the tip is driven into a sample a set distance and the force on the tip is recorded. A relaxation profile can be taken in either the normal or lateral direction. By fitting the relaxation data to known contact mechanics models, the frequency dependent response of a material can be acquired.[4] This technique allows for the frequency dependent storage and loss modulus of nano-indentation to be obtained. By performing a creep profile, the tip is driven into a sample for a set amount of time at a constant force and the voltage on the inner piezo tube is recorded. The voltage on the inner piezo tube will indicate how the sample and tip are responding spatially to the constant applied force.

The IFM can be used in a manner similar to that of AFM for topographic imaging of a sample. Contact mode AFM imaging is almost always done with a net repulsive load, as maintaining a constant attractive force while scanning is difficult with the AFM. The IFM, with the ability to easily counter attractive loads, is able to image a sample under either a repulsive or attractive net load on the tip. As previously mentioned the IFM is also able to do intermittent force or tapping mode imaging. While imaging, the IFM maintains a constant force set-point on the tip by

moving the entire sensor up or down in the z direction with the inner piezo tube and raster scanning in the x and y directions by varying the voltage in the four quadrant outer piezo tube. The IFM is able to vary the voltage on the inner piezo tube by using a separate image controller. The image controller feedback loop has a range of +10 V to -10 V. The image controller output is directly applied to a high voltage operational amplifier controller and then to the inner piezo tube to maintain the force set-point. If the image controller is saturated while trying to maintain the set-point, a larger step will be taken with the outer piezo tube. A surface force image is acquired by mapping the image controller output at each x-y position during a raster scan. The surface force image is directly related to topography for a homogenous surface. Care must be taken when interpreting an image of an inhomogeneous sample with domains of soft material, as soft materials may be indented with a under a load, giving a falsely lower profile.

Probe tips for the IFM can be made out of almost any solid material, as long as it can be attached to the silicon top plate. The most common IFM tips are made from tungsten or gold wires, or from silica tubes or beads. Tungsten tips are chosen because of their high stiffness, and are electrochemically etched using NaOH or KOH. Though tungsten tips can be directly functionalized,[5] gold tips are used for their ability to be functionalized by using well established Au-S linkages for alkanethiol monolayers.[6] Gold tips are electrochemically etched using a 3:1 H_2SO_4/ 30% H_2O_2 solution. These two metal tips are the most commonly used and can be fashioned to have a radius of curvature at their apex from 100 nm to many microns.

Silica tips are either fabricated by firing the end of a hollow capillary tube with a flame or by using an adhesive to mount a bead of known size to the end of a hollow tungsten tube. The tips are mounted to the silicon top plate using a conductive silver epoxy to minimize charging. The size of the tips can be determined using a scanning electron microscope or using in-situ methods. In-situ methods include scanning the tips of sharp SiN grating or raster scanning over sharp SiN spikes. In both of these methods the SiN grating or spikes are much sharper than the tip, so the scan generates an image of the tip instead of the sample. This method is similar to that used for imaging of AFM tips.[7]

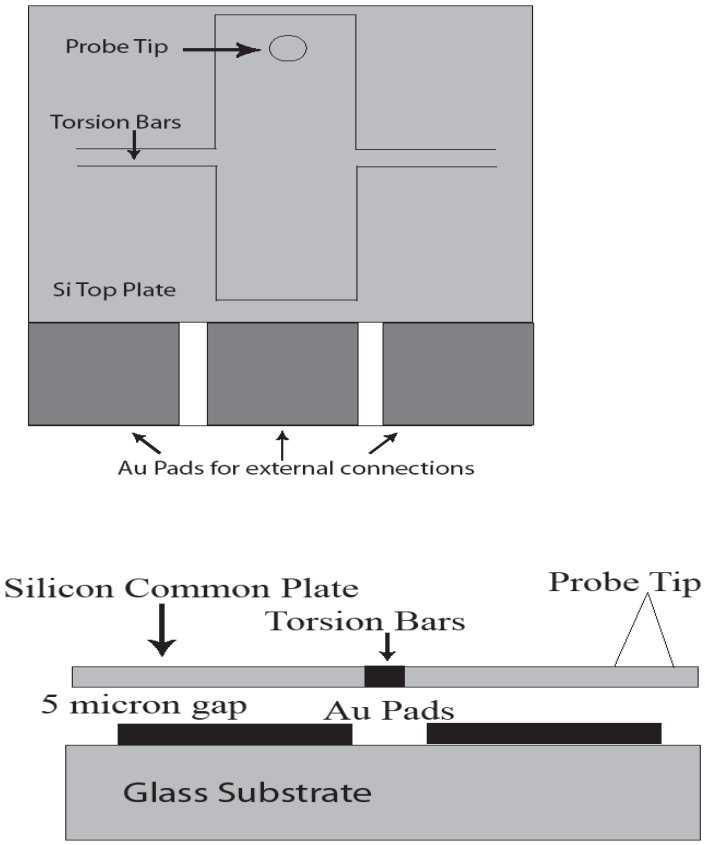

Figure 2.1. Schematic top view (upper) and side view (lower) illustration of the IFM sensor.

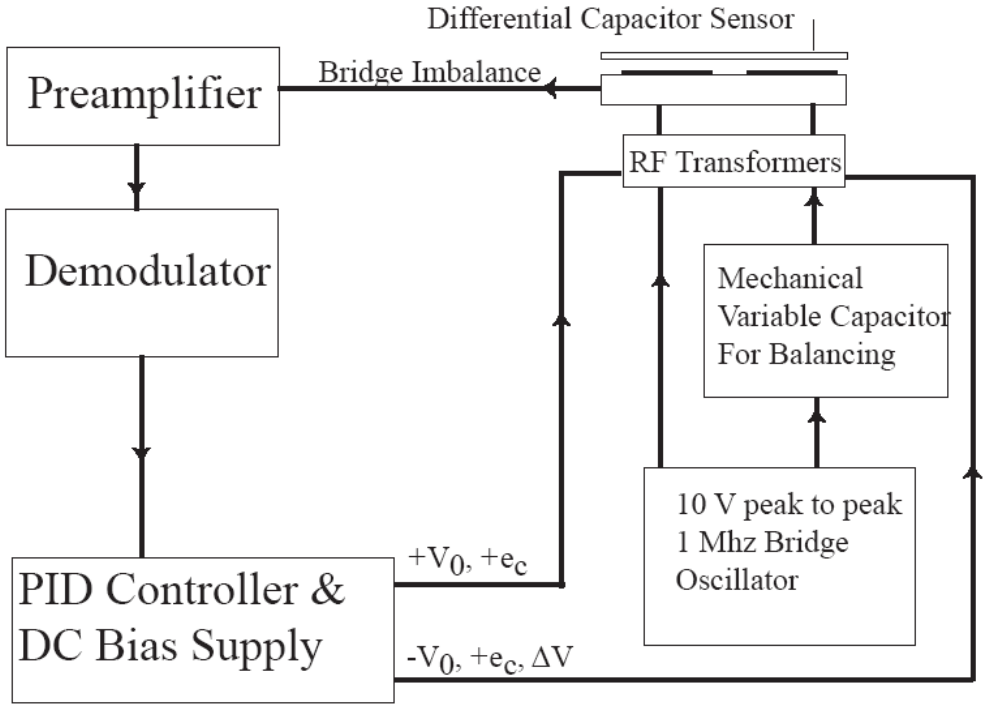

Figure 2.2. A schematic illustration of the IFM controller electronics. An AC bridge is used to detect a change in capacitance. The bridge imbalance is zeroed by applying a DC voltage (ΔV) to one side of the differential capacitor sensor.

2.3 References

1. Bosch, R. (1996) *Method for Anisotropically Etching Silicon*. Patent No. 5501893

2. Carpick, R. W.; Salmeron, M. *Chem. Rev*. **1997**, *97*, 1163-1194

3. Binggeli, M.; Mate, C.M. *Appl. Phys. Lett*. **1994**, *65(4)*, 415.

4. Houston, J.E. J. *Polymer Sci. B.* **2005**, *43(21)*, 2993.

5. Graham, J.F.; Griffiths, M.K.; Norton, P.R.; Ogini, F.; Warrren, O.L. *J. Vac. Sci. Technol*. **1999** *A 17(4)*, 2240.

6. Xu, J.;Li, H.L. *J. Colloid. Interface Sci.* **1995**, *176*, 138.

7. Bhusan, B.: Fuchs, A.H.; Hosaka. S. In *Applied Scanning Probe Methods*; Editor: Villarrubia, J.S.; Nanoscience and Technology; Springer-Verlag: Berlin, 2004.

Chapter 3. Hydrophilicity and the Viscosity of Interfacial Water

3.1 Introduction

Interfacial water is important to a wide range of surface processes such as protein folding,[1-3] stability of colloid suspensions,[2,4] enzyme activity,[5,6] swelling in clays,[7,8] stiction in micro-electromechanical systems (MEMS),[9] and scanning probe microscopy.[10,11] The ordering of water molecules on the nanometer scale next to hydrophilic surfaces has been studied extensively through vibrational spectroscopy,[12-14] scattering techniques,[7,15] atomic force microscopy (AFM) imaging,[16,17] and computer simulations.[18,19] Experiments on the surface of SiO_2, one of the most abundant materials on earth,[20] have revealed a change in intermolecular bonding of interfacial water that is attributed to an increase in the ordering of water molecules near the surface.[11-13] While these results indicated that the interfacial water was "structured", it was unable to solidify to an "ice-like structure" at room temperature and neutral pH. Previous studies concluded that, at intermediate pH values above the isoelectric point of silica (~2-3), there is competition between water molecules hydrogen bonding to protonated silanol (Si-OH) groups with their dipoles pointed away from the surface and water molecules aligning in the electric field of deprotonated silanol anions on the surface with their dipoles pointing into the surface.[12]

Although thin water films adsorbed on silica and other hydrophilic surfaces do not usually solidify at room temperature, they do possess physical properties distinctly different from those of bulk liquid water. It is well known that there is a repulsive force between hydrated surfaces in close proximity of 1-3 nm.[21] Examples include oxides (silica, alumina, mica, clay) and molecules (lipids, DNA, surfactants, etc.). This interfacial repulsion, termed hydration forces or hydration repulsion, has been attributed to the energetic requirement of disturbing the hydration structure near the surface. Force measurements by a number of techniques, including surface force apparatus (SFA), AFM and osmotic stress, have established an exponentially decaying repulsive force between hydrated surfaces, with the decay length in the range of 0.2-1.4 nm. Unlike the long-range electrostatic double-layer force, which depends strongly on ionic strength, the short-range hydration force is independent of ionic strength. While theoretical models, such as the DLVO (Derjaguin, Landau, Verwey, and Overbeek) theory,[22,23] are well established for the electrostatic repulsion, no quantitative theory yet exists for the hydration force.

Shear force measurements have also shown distinctly different mechanical properties of adsorbed water on hydrophilic surfaces. However, experimental results are more varied as compared to those dealing with the hydration force. An earlier measurement by Israelachvili using the SFA technique showed bulk-like viscosity of water confined between two mica surfaces with interfacial separation < 2 nm.[24] Klein and coworkers carried out SFA measurements and reported no appreciable change[25,26] over the viscosity of bulk values for water confined between

two mica surfaces at interfacial separation ≤ 3.5 nm. An AFM study also suggested that adsorbed water on hydrophilic surfaces acts as a lubricant.[27] In contrast, Granick and coworkers found, using SFA, that an ionic water solution compressed by two mica surfaces exhibited azimuthal angle dependent shear viscosity up to three orders of magnitude higher than that of bulk water.[28] This is in agreement with a shear-force microscopy study, which showed the rapid rise in viscosity of confined water as interfacial separation decreases below ~1 nm.[29] It is possible that discrepancies among SFA measurements are due to differences in absolute distance calibration or surface contamination. Nanometer-scale differences in interfacial separation may produce or inhibit the formation of a bulk-like water slip plane between the viscous water layers, since the decay length expected for adsorbed water from hydration-force measurements is on the 0.2-1.4 nm scale. It is also possible that differences in ionic strength may play a role, though previous measurements on hydration repulsion would suggest otherwise. Recently, Butt, Cappella, and Kappl published a comprehensive review of force measurements with the AFM,[30] providing excellent discussions on forces of confined liquids, including water, as well as current theoretical understanding.

We have used interfacial force microscopy (IFM)[31,32] to measure normal and shear forces of water at confined interfaces.[33] The self-balancing force-feedback sensor of the IFM allows for the quantification of the full range of attractive and repulsive forces between a probe tip and substrate. The IFM sensor eliminates the "jump-to-contact" instability that hinders standard compliance-based force-

microscopy techniques such as the AFM and the SFA. Also, the IFM allows the simultaneous measurement of the normal and shear forces. Previous IFM measurements carried out with controlled humidity showed the formation of a water meniscus between two hydrophilic –COOH terminated alkanethiol self-assembled monolayers (SAMs) on a gold substrate and the tip with $\leq$ 1 nm interfacial separation.[33] The simultaneously recorded shear force peaks at ~0.6 nm interfacial separation and corresponds to a viscosity approximately six orders-of-magnitude greater than that of bulk water at room temperature. Interestingly, this exceptionally high viscosity is of the same order as that reported earlier from IFM measurements under water for hydrophilic, oligoethyleneglycol-terminated alkanethiol SAMs on a Au substrate and tip.[34] In this case, the observed repulsive drainage force at the nanometer scale, again, corresponded to an effective viscosity of approximately 10^6 times higher than that of bulk water.

Is the 10^6 increase in the confined-water viscosity from previous IFM measurements unique to surfaces terminated with self-assembled monolayers? One important property of SAMs is that they are structurally ordered in two-dimensions; but, is structural order of the substrate surface important to the formation of the viscous water film? One may expect the answer to be "yes", since most experimental measurements on the mechanical properties of confined liquids have come from SFA experiments using the crystalline mica surface. These measurements have shown the ordering, particularly the layering of liquid

molecules confined between the mica surfaces.[1] The forced structural order under confinement has been used to explain the high viscosity of a variety of liquids.[35]

In order to answer the two questions raised above, we conducted IFM measurements of the viscosity of confined water using an amorphous silica surface (native oxide terminated silicon wafer) and oxide-terminated W tip. We obtained viscosity values from friction force measurements for a water meniscus formed between the tip and the silica surface under ambient conditions, as well as, from friction and normal force measurements for the interfaces under water. In all three types of measurements, we obtained an effective viscosity ~10^6 times greater than that of bulk water for interfacial separation on the nanometer scale. This kind of viscous interfacial water film does not exist when the hydrophilicity of the oxide-terminated silicon surface is degraded, e.g., by terminating the silicon surface with -H or -CH_3. Thus, it is clear that the criterion for the formation of a viscous interphase water film is the hydrophilic nature of the surface. The role of the surface structure is, as yet, not clear.

3.2 Experimental

Force profiles, i.e., normal force versus relative interfacial separation, and viscous drainage experiments were carried out in a manner as previously described.[33,34] Lateral forces were measured by driving the tip laterally with a ~16 Å peak-to-peak dither at 100 Hz and synchronously detecting the force signal with a lock-in amplifier. This method allowed for the magnitude and the phase to be

simultaneously recorded as a function of the normal force. The relative humidity (RH) was controlled in the chamber by using N_2 flow through a water-filled bubbler. For measurements in water, a small amount of ultra-pure water (>18MΩ·cm) was placed between the tip and the surface. All data reported were recorded at room temperature (~25°C).

IFM tips made by electrochemical etching W wire were subsequently imaged with a scanning electron microscopy, as well as optical microscopy, to determine their general morphology and size. Before use, all tips were cleaned in 3:1 concentrated H_2SO_4/30% H_20_2 (Piranha) to remove organic contaminates and thoroughly rinsed in ultra-pure water (Caution! Piranha is a strong oxidant and reacts violently with organic substances). All silicon surfaces were prepared from n-type doped Si(111) wafer (0.8-10 Ω-cm). The surfaces were first sonicated in acetone for 5 minutes to remove particulates, boiled at 100°C in Piranha for 2 hours, and thoroughly rinsed with ultra-pure water. Wafers were then blown dry with high purity N_2. This procedure leaves a very hydrophilic surface with the native oxide of the silicon intact, terminated by hydroxyl groups. We will refer to this surface here as SiO_2-OH. Water wet the oxide surface completely, making contact angle measurement impossible. Hydrogen-terminated silicon surfaces were prepared by placing a clean silicon sample in a 50% HF solution for 1 minute to remove the surface oxide, leaving the surface terminated by hydrogen, referred to here as Si-H (Proper personal protective equipment necessary to minimize exposure to the HF solution). Methyl-terminated surfaces were prepared by first removing the oxide

layer by placing the Si sample in a 40% NH_4F solution for 4 minutes while sparging the solution with high purity Ar. The wafer was briefly rinsed with ultra-pure water and inserted into a vacuum line with a base pressure of ~10 mTorr. The surface was chlorinated by 3 repeated 5 minute exposures to a 6 Torr atmosphere of Cl_2 at 80°C. After chlorination the wafer was placed in a reactor with 10 ml of 3M $ClMgCH_3$ in tetrahydrofuran (THF), along with 40 ml excess anhydrous THF, for 4 hours at 65° C. Unreacted reagents were removed by sonicating the wafer in THF and then briefly rinsing with ultra-pure water. This process resulted in a surface densely covered by terminal $–CH_3$ groups, referred to here as Si-CH_3. Data was taken immediately after preparation to reduce the risk of surface contamination.

3.3 Results

The first set of experiments was carried out under ambient conditions with controlled humidity (RH ~45%). We measured both the normal and lateral forces on the probe tip as it approached contact through water formed by adsorption and capillary condensation. Figure 3.1A shows normal (F_N) and the magnitude of the lateral-force (F_{Mag}) as the W probe tip of radius ~10 µm approaches the SiO_2-OH surface. The lateral force shows a peak at a relative displacement of ~37 Å. The appearance of the peak is similar to that previously observed on hydrophilic SAM terminated surfaces[33] and arises from the probe tip driving laterally through a viscous nanometer size meniscus of water. Although it is difficult to determine the exact point of interfacial contact, it is most likely slightly before the attractive

normal-force maximum, indicated by the dashed vertical line at a relative displacement of ~24 Å. Since energy dissipation (friction), due to the lateral motion, will appear in quadrature (90° out of phase) with the dither drive, we only consider this component when analyzing friction data. The quadrature component, and thus the friction component, of the lateral force is shown in Figure 3.1C and is given by the relation,

$$F_{Fric} = F_{Mag} \cdot \sin(\theta), \qquad (1)$$

where θ is the phase angle shown in Figure 3.1B. The importance of using the quadrature component of the lateral force in data analysis was not appreciated in previous work, in which the analysis was done with F_{mag}, not F_{Fric}.[33] Here, the out-of-contact peak in F_{Fric} is more prominent than that in F_{mag}. We also see additional peak(s) in F_{Fric} after contact is made. The nominal quantity of F_{Fric} in the contact region has complex origins. The tip undergoes stick-slip motion ($\theta > 0$) or is completely stuck ($\theta = 0$) with the substrate surface. In this report, we only focus on the out-of-contact region. We do not attempt a physical interpretation of lateral force after contact is made.

Note that surface cleanness is of critical importance to obtaining reliable data. All measurements shown here are obtained for freshly prepared surfaces. After a period of a few hours, the system (water/surface conditions) deteriorates and the out

of contact peak in F_{Fric} gradually disappears, presumably, because of a decrease in the level of hydrophilicity from adsorbed contaminates.

Previous results have shown that the hydrophilicity of the surface plays a large role in the formation of viscous interphase water.[33,34] In order to investigate this, we degraded the hydrophilicity by terminating the Si surface with –H, instead of the –OH termination on the native oxide surface. We observe that this greatly diminishes the out of contact friction-force peak, as seen in Figure 3.2. The normal force profiles show that the attractive well for the Si-H surface is shallower than that of the SiO_2–OH surface, due to reduction in capillary condensation and the associated Laplace pressure.

As a comparison to results obtained under ambient conditions presumably due to the water meniscus, we carry out measurements for the tip and the surface immersed in water. Figure 3.3 shows the normal and the friction force as a W tip approaches a SiO_2–OH surface submerged in water. Similar to results shown in Figure 3.1C, we observe a rise in the friction force before repulsive contact is made. Again, we focus on the out-of-contact region and do not attempt a physical interpretation of the nominal friction force after contact in made. The gray curve is a fit to be discussed later. For the experiment carried out under submerged conditions, the normal force profiles also provide quantitative information on the physical properties, particularly the viscosity of the hydration layer. This involves the velocity dependent drainage of the viscous interface water layer between the tip and the substrate surface.[34] Figure 3.4 shows the behavior of the normal force for an oxide terminated W probe

tip approaching a hydrophilic SiO_2–OH surface (A) and a hydrophobic Si-CH_3 surface (B) in water. For the hydrophilic surface, the normal force shows a repulsive region that scales positively with approaching speed, v_a. For comparison, the normal force on the Si-CH_3 surface is virtually independent of the speed.

3.4 Discussions

In analyzing the viscous behavior of interfacial water, we first consider the forces at the largest interfacial separations. Figures 3.1A and 3.1B show that as the tip approaches the substrate the lateral force begins to increase with a phase of ~150°. This distance is near the point where the attractive (negative) normal force begins to increase both from contact of the two adsorbed water films and capillary condensation of water in the interfacial gap. We attribute the small increase in lateral force to an inertial effect due to the mass of a water meniscus as we drive the tip back and forth, which would give a phase of ~180°, similar to a mass oscillating on the end of the spring-like tip, and only a small component of friction, as indicated in panel 1C. As the tip approaches the substrate more closely, the lateral force rises and peaks before making interfacial contact, i.e., in the area where only the behavior of the meniscus itself is observed under the influence of the later tip motion.

Assuming the out of contact friction peak of Figure 3.1C is due to the water meniscus, the observed behavior must either by due to a viscous flow pattern within the meniscus itself or, perhaps, to the hysteretic effect of the advancing/receding

contact behavior as the tip moves back and forth. Such behavior is clearly observed if the tip is moved back and forth in a line-scan mode over several tens of Å. If we assume first that the meniscus water has a high viscosity due to it small initial confinement, we can make a crude calculation of what the viscosity would have to be in order to produce the observed results. We start by calculating cross sectional area (A_m) of the water meniscus from the attractive normal force and the Kelvin radius (r_K) of the meniscus given by,[1]

$$r_K = \frac{\gamma_{\mathbf{H_2O}} V_M}{RT \ln(p / p_s)}, \qquad (2)$$

where γ_{H2O}, V_M, R, T, and p/p_s are the surface tension, the molar volume of the water meniscus, the gas constant, the absolute temperature, and the relative humidity, respectively. Using the values of bulk water at 20°C, we have r_K = -1.6 nm at 45% RH. The Laplace pressure[1] of the water meniscus is $P_L = \gamma_{H2O}/r_K$ and the capillary force is $F_N = A_m P_L$. When the out of contact friction force peaks, the corresponding attractive normal force (F_N = -0.8 μN) indicates the size of the meniscus is A_m ~ 7280 nm^2. Note that γ_{H2O} of the nanoscopic meniscus is not known and the calculation uses the value for liquid water. For comparison, the surface tension of ice can be as high as twice that of liquid water. [36]

Under the simple assumption that the velocity profile under shear is linear and given by A_m, the peak friction force value of F_μ = 28 nN, and an experimental shear

velocity of v_s = 3200 nm/s, we can calculate the effective viscosity (η_{eff}) of the water meniscus as,

$$\eta_{eff} = \frac{\textbf{shear stress}}{\textbf{shear rate}} = \frac{(F_\mu / A_m)}{(v_s / d)} = 1.6 \times 10^3 \,\textbf{Pa} \cdot \textbf{s}, \qquad (3)$$

where d (~ 1.3 nm) is the interfacial distance at which the friction force peaks. The effective viscosity of the water meniscus between two hydrophilic surfaces based on this estimate is more than six orders of magnitude higher than the viscosity of bulk water (η_{bulk} = 8.6x10^{-4} Pa·s at room temperature). Within the level of our approximations, these results generally agree with friction-forces measured for a viscous interfacial water meniscus on hydrophilic SAMs, where a value of ~30 kPa·s was obtained.[33] Under this assumption, the fall in friction could be attributed to the growth of the meniscus, which would decrease the level of confinement and, thus, the viscosity. Three other possibilities remain.

The first attributes the friction drop to the increasing shear rate as the tip nears the surface. The shear rate varies as the lateral tip velocity divided by the relative separation of the tip and substrate. As the tip approaches the surface the shear rate dramatically increases. It is possible that there is a threshold shear-rate value where the "no-slip" boundary condition no longer applies and interfacial slip occurs, reducing the friction level.[37] The second also involves the increased shear rate, along with the fact that the tip runs back and forth over the same interfacial

region. This may lead to a degradation of the interphase-water structure, again, reducing the friction level. A final factor is an instrument effect involving the lateral compliance of the tip and sensor. The sensor is being driven in lateral displacement by a constant amplitude sine wave. The detection system can, thus, be modeled by a spring and viscous "dash pot" in series. Under a displacement drive, a very stiff spring (relative to the viscosity), will result in the displacement principally involving the viscous element (in quadrature with the lateral drive). Conversely, a weak spring will cause the displacement to occur mainly in the spring element (in phase with the lateral drive). Therefore, if one plots only the quadrature component of the force resulting from the displacement, the measured friction force will be a maximum at the point where the spring and viscous displacement are equal. In the present case, the spring has a constant compliance coefficient, while the viscosity dramatically increases as the interfaces approach. With lateral tip/sensor compliance, such behavior will always produce a peak in the friction-force signal. However, in actually modeling such a system, the initial rise and narrow nature of the data shown in Figure 3.1C cannot be adequately reproduced. Thus, although this effect may play a role, it does not give an adequate explanation of the out of contact friction behavior. Contrarily, the "in contact" friction peak observed from contact of the tip with the substrate can be adequately modelled with a "dash pot" model as after contact, the phase drops to $\sim 0^{o}$ and F_{mag} settles at a constant level, indicating that the tip is effectively stuck under a high load.

In agreement with previous results[33] we observe that changing the hydrophilicity of the surface affects the viscosity level of the interfacial water. As seen in Figure 3.2, degrading the hydrophilicity of the surface by terminated it with –H, instead of the native oxide, leads to a dramatic decrease in the intensity of the out-of-contact friction peak, implying a reduction in the ability of the surface to from the viscous interfacial-water meniscus. The small peak remaining in the friction force is attributed to the viscous interfacial water present on the hydrophilic tip.

In order to establish that the observed the friction-force behavior seen in Figure 3.1C is not unique to the small water meniscus, we obtain similar data on the same tip/substrate combination while both are immersed in water. The results are shown in Figure 3.3, along with a fit to the model described by Feibelman for a spherical tip moving in shear near a surface both covered by thin interfacial water films having finite thickness and constant viscosity.[38] In this case, the meniscus still exists, but it is large and can be adequately compensated for, since its contribution to the total tip/substrate force is constant over the extent of a force-profile data. This lateral-force model yields the approximate relationship,

$$F_{\eta} = 2\pi\eta\omega x_0 R \ln(\frac{2w}{D}), \tag{4}$$

where η, ω and x_0 are the interphase film viscosity, the angular frequency of the lateral dither and the dither amplitude, respectively. The approximation is accurate for values of 2w/D less than ~0.5.[38] The solid grey line in Figure 3.3 shows a fit to

the initial rise of the friction force peak according to the Feibelman model. The fit reveals an interphase-layer thickness of ~7Å, and a calculated viscosity of ~4.1 kPa·s. Although the Feibelman model is appropriate for a thin film of constant viscosity and discrete thickness, the actual film may not have such attributes.

The results from measurements under submerged conditions in Figure 3.3 appear slightly different than those of Figure 3.1C. The adhesive force, which here should be principally due to a van der Waals interaction, is virtually eliminated by the presence of the intervening water.[1] The friction force has a similar appearance to the meniscus case. In this case, we observe only a single friction peak. The reason for the single peak is that, in this case, the out of contact friction is not from of a viscous meniscus but from contact of two thin films of viscous interfacial water. The level of friction caused by contact of the two interfacial films gives rise to a sharp initial rise starting about 5-6 Å ahead of tip/substrate contact. At this peak in the friction force, the phase dramatically begins to drop to zero because the tip begins to stick during an ever increasing portion of the lateral cycle, causing the phase (not shown) to decease to ~0^{o}. However, the results clearly indicated that the viscous interphase water layer is present at essentially the same level for the SiO_2–OH surface in both the low-level meniscus and tip/substrate immersion cases. As with the meniscus experiment, a control Si-CH_3 under water surface shows no appreciable out of contact friction (not shown).

Further support for a viscous interfacial-water layer on SiO_2–OH comes from drainage-force experiments. A repulsive drainage force that scales directly

with tip approach speed (ν_a) for a tip and substrate immersed in water has been observed in earlier IFM experiments by Kim et al. for an Au tip and an Au substrate both functionalized with a hydrophilic oligoethyleneglycol-terminated SAM film.[34] In the classical example of a sphere approaching a flat surface in a Newtonian liquid (viscosity independent of shear rate), the repulsive force is given by,

$$F_\eta = 6\pi\eta\upsilon_a \frac{R^2}{D}, \tag{5}$$

where η is the viscosity of the liquid; ν_a is the approach speed; R the tip radius and D (<< R) is the interfacial separation.[39] Recently, Feibelman developed a modification to this model to account for the situation where constant-viscosity interphase layers with fixed thicknesses on both tip and substrate approached each other at a constant velocity while immersed in bulk water. The Feibelman drainage model takes the form,[40]

$$F_\eta = 6\pi\eta\ \nu_a \frac{R^2}{D}\left(1-\frac{D}{2w}\right)^2, \tag{6}$$

where η and w are the viscosity and the viscous-layer thicknesses on both hydrophilic surfaces, respectively.

In fitting the experimental data to Eq. 6, we need to take into account the small compliance of the tip and substrate as well as the two SAM films, as described

earlier by Kim, et al.[34] This makes it possible to better isolate the behavior of only the viscous-water layer. The procedure involves first fitting force profiles taken under dry conditions to known contact mechanics models to obtain the in-contact force versus displacement relationship. The Johnson-Kendall-Roberts (JKR)[41,42] model was used for a spherical tip deforming a flat surface in the presence of adhesion. We carry out IFM measurements at low relative humidity (RH <5%) to minimize the possible effect of interfacial water on compliance characterization. We note that even though we use the JRK procedure in order to obtain the compliance behavior in the repulsive region, none of the standard contact mechanics models are able to fit real data in the attractive region. However, since there is negligible adhesion in the present case the JKR or Hertz models will work well in the repulsive region, which is the only region of interest here.

Figure 3.5 shows normal force profiles on the SiO_2-OH surface and the Si-CH_3 surface at <5% RH. The JKR fit to each force profile yields a composite modulus of ~38 GPa for both surfaces. Once the composite modulus is known, it can be removed from the force profiles by adjusting the displacement axis using the Hertzian relationship between force and displacement for the tip and substrate.[34,43] The results are shown in Figure 3.6, which indicates the behavior of the viscous interfacial water corrected for the film/film compliance. The solid lines in Figure 3.6A are fits to Eq. 6, which yield a common value for the effective viscosity of ~7 kPa·s and an interphase water film thickness of ~17 Å. Similar results for the hydrophobic Si-CH_3, are shown in Figure 3.6B, indicating little velocity-dependent

behavior. The small residual velocity-dependent force is attributed to the viscous interphase water present on the hydrophilic W tip.

The estimated viscosity values of 1.6-7 kPa·s for interfacial water on SiO_2-OH from the three types of measurements presented above are of the same order as those on the carboxylic acid- or oligoethyleneglycol-terminated SAMs reported earlier.[33,34] These values are about 6-7 orders-of-magnitude larger than the 0.89 mPa·s of bulk water at 25°C,[44] but still 7 orders-of-magnitude smaller than the 10 GPa·s viscosity reported for bulk ice.[45] The values of ~7-17 Å for the thickness of the viscous water layer also agrees well with the reported value of ~3-4 molecular-layer thicknesses of "ice-like" water films on SiO_2–OH from vibrational spectroscopy.[13]

Contrary to the work of Antognozzi,[29] we do not see evidence of oscillations in the force profiles corresponding to the layering of interfacial water. This difference can be attributed to the size differences of the contact areas between the experiments. The larger contact area in our IFM experiment may allow for interference effects due to unavoidable surface roughness, thus canceling out observations of layering.

Though we have shown an increase in viscosity of water near a hydrophilic surface, the exact cause of this phenomenon is unclear. We propose two explanations for the increase: one is the increase in the intermolecular hydrogen bonding between water molecules at the surface of SiO_2-OH, as observed with attenuated total reflection-infrared (ATR-IR)[13,14] spectroscopy and sum frequency

generation (SFG) spectroscopy.[12] The ATR-IR work has shown that a thin film (~3-4 monolayers) of "ice-like" water is present at a SiO_2/H_2O interface.[13] The SFG experiment also show an increase in order due to hydrogen bonding of water to surface Si-OH groups and electrostatic interaction with charged surface groups.[12] The fact that we see a strongly viscous interphase only for highly hydrophilic surface combinations, supports this explanation. A second possible reason is the slowing of hydrogen bonding and orientation dynamics for nano-confined water.[46] Previous work has shown that the rate of energy transfer for water molecules confined in a "molecular cage" slows down by a factor of 20 over that of bulk water.[46] The reason for this is that in bulk water the energy barriers to hydrogen-bond breaking and the changing of molecular orientation for subsequent hydrogen bond creation is relatively low. In comparison, water molecules under nano-confinement have a higher barrier to hydrogen bond reorganization as the confinement creates less neighboring water molecules spatially available for hydrogen bonding.

Considering the assumptions made in the derivation of our models for using both normal and shear forces in calculating viscosity, our experimentally-derived values should be considered only as order-of-magnitude estimate. As previously stated, we could improve this model by including shear slip,[37] which is likely to occur when the tip moving in shear very close to contact with the substrate, as well as by creating a better model for the mechanical behavior of the tip and sensor. Note also that we are currently limited to using continuum models of our nanoscale

systems. Obvious problems are encountered here, since discrete molecular/atomic models are needed at this length scale.

3.5 Conclusions

We have presented evidence for a viscous, interfacial-water layer on highly hydrophilic surfaces with viscosity values 6-7 orders-of-magnitude larger than that of bulk water. We have conducted two separate experiments that verify these results for both water forming a small meniscus between hydrophilic tip and substrate under humid conditions, as well as for both tip and substrate immersed in bulk water. In contrast, experiments on surfaces modified by hydrophobic films show a dramatic decrease in the viscous behavior. Thus, the strength of the interfacial surface binding with water is a key factor in the formation of the viscous interphase. Previous spectroscopy work in this field has provided insight into the increase in ordering and hydrogen-bond dynamics that are undoubtedly critical to the creation of the observed increase in viscosity. In addition, our values for the thickness of the viscous interfacial-water layer (7-17 Å) agree reasonably well with the ~10 Å thickness determined by spectroscopy. Future work is needed to investigate the details of the viscoelastic behavior of the interfacial water. These will involve detailed relaxation measurements of the draining behavior as the tip is stepped toward and away from the substrate at various levels of separation. Such work is critical to obtaining a microscopic understanding of both the interfacial and intermolecular bonding and how they impact the viscoelastic behavior.

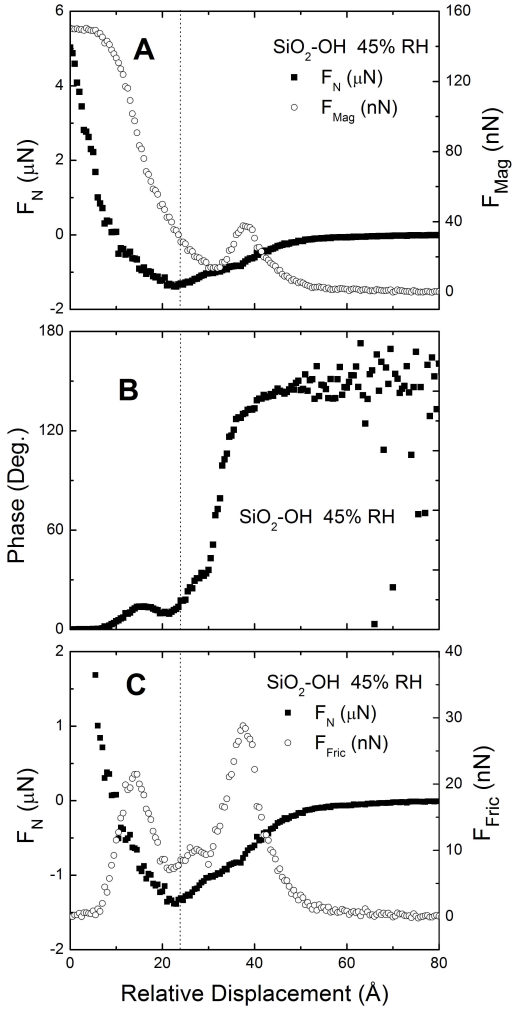

Figure 3.1. (A) Normal force (filled squares) and the magnitude of the lateral-force (open circles) vs. relative tip displacement. (B) Phase between the lateral force and the dither drive vs. relative displacement. (C) Normal force (filled squares) and friction force (open circles) vs. relative displacement. The dashed vertical line is an approximation of tip-substrate contact. Force profiles were taken at ~45% RH on a SiO_2-OH surface with a ~10 μm W tip.

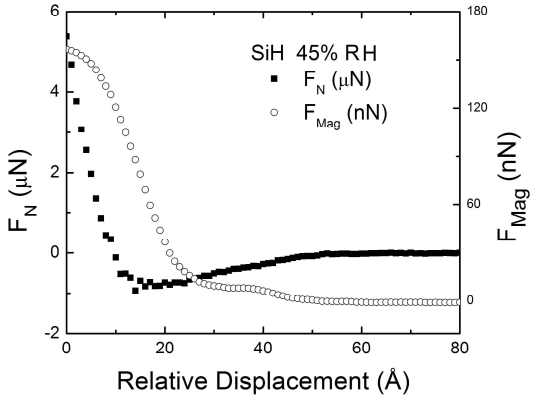

Figure 3.2. Normal force (filled squares) and of the lateral-force magnitude (open circles) vs. relative displacement taken on a Si-H surface at 45% RH ~10 μm W tip.

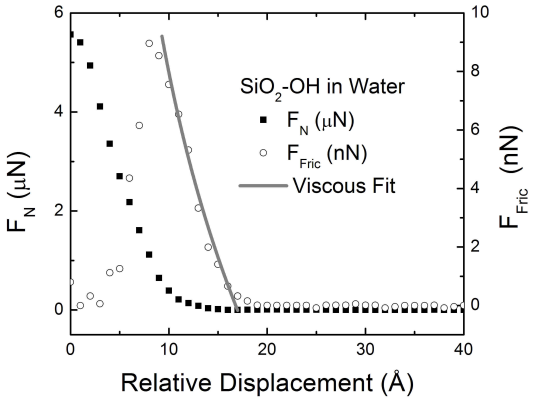

Figure 3.3. Normal force (filled squares) and friction force (open circles) vs. relative separation taken on a SiO_2-OH surface in water with a ~1.3 μm W tip. The solid grey line is fit discussed in the text.

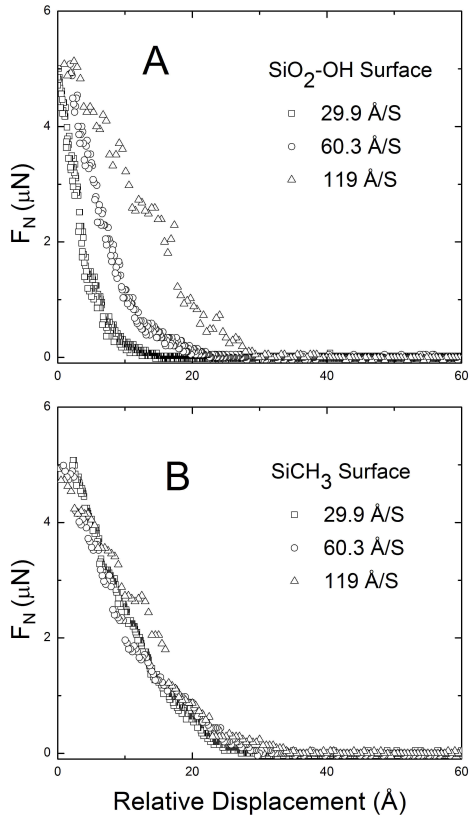

Figure 3.4. (A) Normal force vs. relative displacement as a ~1.3 μm W tip approaches a SiO_2–OH surface in water at varying speeds. An increasing viscous response in the normal force is seen with increasing approach speed. (B) Normal force vs. relative displacement as the tip used in (A) approaches a Si-CH_3 surface in water at varying speeds. The approach-speed dependent viscous drainage force has virtually disappeared.

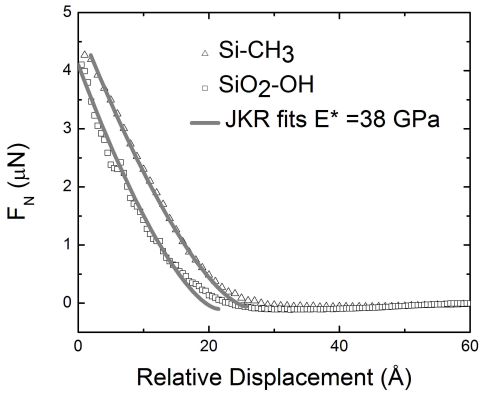

Figure 3.5. Normal force vs. relative displacement for SiO_2-OH (open triangles) and Si-CH_3 (open squares) at 5% RH with a ~1.3 μm W tip. Solid lines indicate fits to the JKR model. The fits for both surfaces yield a composite modulus of ~38 GPa.

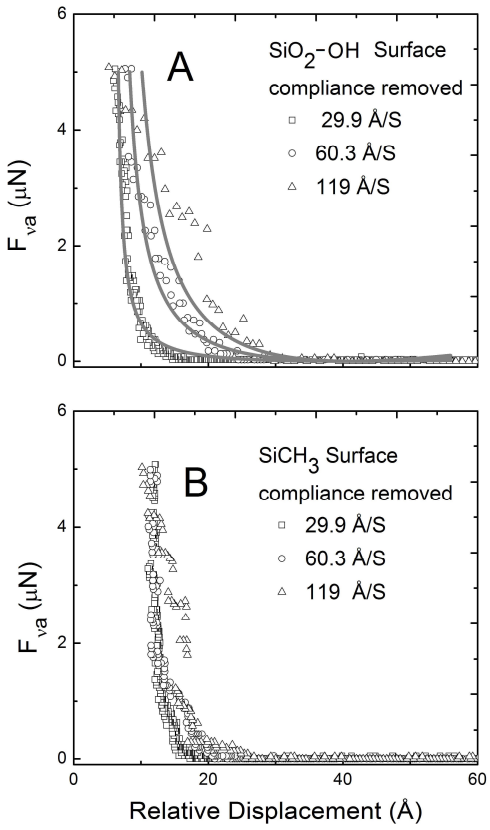

Figure 3.6. Normal force vs. relative displacement as the tip approaches a SiO_2-OH surface in water at varying speeds corrected for the film/film compliance. The solid lines represent a best fit using the Feibelman drainage model with a 17 Å interphase layer having a viscosity of 7 kPa·s. (B) Similar data for the Si-CH_3 surface in water. Force profiles were taken with a ~1.3 μm W tip.

3.6 References

1 Israelachvili, J. *Intermolecular and Surface Forces*; Academic Press: London, 1992.

2 Israelachvili, J.N.; Wennerstrom, H. *Nature* **1996**, *379*, 219.

3 Vogler, E. A. *Adv. Coll. Interface Sci***. 1998**, *71*, 69-117.

4 Crocker, J. C.; Matteo, J. A.; Dinsmore, A. D.; Yodh, A. G. *Phys. Rev. Lett.* **1999**, *82, (21),* 4352-5355.

5 Ramos, A. S. F.; Techert, S. *Biophys. Journal* **2005**, *89*, 19902003.

6 Rao, C. S.; Damodaran, S. *Colloids and Surfaces B* **2005,** *45-1*, 49-55.

7 Fenter, P.; Sturchio, N. C. *Progress in Surface Science* **2004,** *77*, 171-258.

8 Karaborni, S.; Smit, B.; Heidug, W. Urai, J. Van Oort, E. *Science* **1996**, *271*, 1102-1104.

9 Maboudian, R. *Surf. Sci. Rep*. **1998**, *30*, 207-269.

10 Jang, J.; Schaz, G. C.; Ratner, M. A. *J. Chem. Phys.* **2004**, *120*, 1157-1160.

11 Szoszkiewicz, R.; Riedo, E. *Appl. Phys. Lett*. **2005**, *87*, 033105.

12 Du, Q.; Freysz, E.; Shen, Y. R.; *Phys. Rev. Lett.* **1994**, *72,(2)*, 238-241.

13 Asay, D. B.; Kim S.H. *J.Phys. Chem. B.* **2005**, *109*, 16760-16763.

14 Yalamanchili, M. R.; Atia, A. A.; Miller, J. D. *Langmuir* **1996**, *12*, 4176-4184.

15 Bellissent-Funel, M.-E. *Eur. Phys. J. E.* **2003**, *12*, 83.

16 Hu, J.; Xiao, X.-D.; Ogletree, D.F.; Salmeron, M. *Science* **1995**, *268*, 267.

17 Vergaguer, A.; Sacha, G. M.; Bluhm, H.; Salmeron, M. *Chem. Rev.* **2006**, *106*, 1478.

18 Ju, S.-P.; Lin J.-G.; Lin J.-S.; Lin, Y.-S. *J. Chem. Phys.* **2005**, 122, 154707.

19 Gallo, P.; Rapinesi, M.; Rovere, M. *J. Chem. Phys.* **2002**, *117-1*, 369-375.

20 Iler, R.K. *The Chemistry of Silica*; Wiley; New York, 1979.

21 Leikin, S.; Parsegian, V. A.; Rau, D. C.; Rand, R. P. *Annu. Rev. Phys. Chem.* **1993**, *44*, 369.

22 Derjaguin, B. V.; Landau. L. *Acta. Physicochim.* **1941**, *14*, 633.

23 Verwey, E. J. W.; Overbeck, J. T. G. *Theory of the stability of lyophobic colloids*; Elsevier: New York, 1948.

24 Israelachvili, J. N. *J. Coll. Interf. Sci.* **110**, 263 (1986).

25 Raviv, U.; Giasson, S.; Frey, J.; Klein, J. *J. Phys. Condens. Matter* **2002**, *14*, 9275.

26 Raviv, U.; Laurat, P.; Klein, J. *Nature* **2001**, *413*, 54.

27 Binggeli, M; Mate, C.M. *Appl. Phys. Lett.* **1994**, *65*, 415.

28 Zhu, Y.; Granick, S.; *Phys. Rev. Lett*. **2001**, *87(9)*, 096104.

29 Antognozzi, M.; Humphris, A. D. L.; Miles, M. J. *Appl. Phys. Lett.* **2001**, *78*, 300.

30 Butt, H.J.; Cappella, B.; Kappl, M. *Surf. Sci. Rep*. **2005**, *59*, 1.

31 Houston, J. E.; Michalske, T. A. *Nature* **1992**, *356*, 266-267.

32 Houston, J. E.; Joyce, S. A.; *Rev. Sci. Inst*. **1991**, *62-3*, 710-715.

33 Major, R.C.; Houston, J.E.; McGrath, M.J.; Siepmann, J.I.; Zhu, X.-Y. *Phys. Rev. Lett.* **2006**, *96*, 177803.

34 Kim, H.I.; Kushmerick, J.G.; Houston. J.E.; Bunker B.C. *Langmuir* **2003**, *19*, 9271.

35 Hu, H.-W.; Carson, G. A.; Granick S. *Phys. Rev. Lett.* **1991**, *66*, 2758.

36 Douillard, J. M.; Henry, M. *J. Coll. Interface Sci.* **2003**, *263*, 554.

37 Zhu, Y.; Granick, S., *Phys. Rev. Lett.* **2001,** *87,(9)*, 096105.

38 Feibelman, P. J. *Langmuir* **2006**, *22*, 2136-2140.

39 Chan, D. Y. C.; Horn, R. G. *J. Chem. Phys.* **1985**, *83*, 5311-5324.

40 Feibelman, P. J. *Langmuir* **2003**, *20*, 1239-1244.

41 Johnson, K.L.; Kendall, K.; Roberts, A.D. *Proc. Roy. Soc. London* **1971**, *A 324*, 301.

42 Carpick, R. W.; Agrait, N.; Olgeltree, D. G.; Salmeron, M. *J. Vac. Sci, Technol., B* **1996**, *14*, 1289-1295.

43 Hertz, H. *J. Reine Angew. Math* **1882**, *92*, 156.

44 CRC Handbook of Chemistry and Physics, 79th ed.; Lide, D. R., Ed.; CRC Press: Boca Roton, Fl, 1998.

45 Lavrov, V. V. *Deformation and strength of ice*; Israel Program for Scientific Translations: Jerusalem, 1971.

46 Gilijamse, J. J.; Lock, A. J.; Bakker, H. J.; *Proc. Nat. Aced. Sci.* **2005**, *102-9*, 32020-3207.

Chapter 4. Exploring the Liquid-Like Layer on the Ice Surface

4.1 Introduction

The debate on why ice is so slippery has been going on for almost 160 years and is presently thought to be the result of a thin, lubricating water layer on the ice surface even at temperatures well below the melting point.[1,2] This water film, termed a "liquid-like layer" (L-LL), is the result of premelting and is expected to possess physical properties between those of water and ice. The presence of the L-LL has been verified by a wide range of physical techniques, including optical spectroscopy,[3] scattering,[4] proton channeling,[5] ellipsometry,[6] wire regelation,[7] calorimetry,[8] and scanning probe microscopy.[9,10,11,12,13] Several review articles have summarized previous work in this field.[1,2,14,15] The general consensus is that the L-LL exists on the ice surface at temperatures higher than approximately -35^{o}C, and that its thickness increases with temperature. While premelting is common to many solids, only for ice, with a melting point of 0°C, does it have broad consequences, ranging from geological and atmospheric sciences to daily life.

Despite all the physical measurements, surprisingly little is known about the mechanical properties of the L-LL when one brings a solid surface into contact with ice. For example, does the L-LL wet a hydrophilic surface? If so, does the resulting interaction create a meniscus-like attractive force and what are its viscoelastic properties? To shed light on these questions, we carry out quantitative

measurements of the ice surface using Interfacial Force Microscopy (IFM).[16,17] We find that the L-LL is responsible for a thickness dependent adhesive-force behavior, whose general appearance is similar to that of a meniscus formation but, in detail, does not fit the behavior predicted, for example, by a simple Laplace-pressure analysis. In addition, friction measurements, obtained synchronously by imposing a small lateral-dither displacement on the probe, shows a rapid rise in the friction force within ~20 nm of repulsive contact with the solid-ice surface, indicating a viscous near-surface "interfacial" film within the overall L-LL.

4.2 Experimental

The IFM is a scanning force microscope, similar to the atomic force microscope (AFM), but is distinguished by a self-balancing, force-feedback sensor. The unique sensor allows the full range of adhesive and repulsive forces to be measured from ~1 nN to 350 μN, without the typical jump-to-contact instability of spring-based sensors. The probe used here was a pulled glass rod with a ~150 μm spherical-tip radius. The probe was cleaned in Piranha (3:1 conc. H_2SO_4/ 30% H_2O_2; Caution! Piranha solution is a strong oxidant and reacts violently with organic substances) to remove any adventitious adsorbed organic contaminants resulting in a clean-glass surface having a water contact angle of ~0°. Ice samples were grown from drops of Millipore ultra-pure water (18MΩ·cm) on a metal substrate cooled by a Peltier cooler to a temperature as low as -30.0±0.1°C. The ice samples were annealed through multiple thaw/freeze cycles to attain an optically smooth surface. All

measurements were carried out in dry N_2 to minimize condensation at low temperatures.

In the IFM measurements, the sample stage was cooled while the glass tip was not. However, we carried out thermal transport modeling using a finite element code within the COMSOL software package and found that the temperature of the glass tip, while in the vicinity of the ice surface, should be $< 1^oC$ higher than that of the ice surface. For each force profile, the probe approached a freshly annealed ice surface at a constant rate while recording the normal force. Friction forces were simultaneously obtained by driving the sensor laterally with a ~3 nm peak-to-peak, 50-200 Hz dither and synchronously detecting the force signal with a lock-in amplifier. The dissipative, or friction component, of the lateral force signal, was obtained by recording that portion of the signal in quadrature with the dither drive signal.

4.3 Results and Discussion

The presence of a L-LL is evident in the normal force profiles shown in Fig. 4.1(a) as the spherical glass probe approaches the ice surface from left to right. The most prominent feature is an attractive region (negative forces) shrinking in both width and magnitude as the temperature decreases. At -30^oC the attractive force is essentially negligible. The rapid rise in normal force at displacements to the right of zero indicates tip contact to the solid-ice substrate. Initial contact with the L-LL is signaled by a very small but sudden increase in the attractive force only visible in

the profiles when viewed on an expanded force scale. As the tip continues its approach, the attractive force takes on an appearance similar to that of a growing "meniscus", with the depth and range of the adhesive interaction decreasing with decreasing temperature. We take the displacement from the initial attractive-force onset to the bottom of the attractive well to be the thickness of the L-LL, as shown by the vertical dashed lines for T = -10^{o}C in Fig. 4.1. Using values obtain by this approach, we plot in Fig. 4.2 the thickness of the L-LL as a function of temperature. We find that the thickness scales logarithmically with temperature, i.e., $D(nm) = A - \mathrm{B}\ln(T_m - T)$, in agreement with previous reports.[5,10] Here T_m= 0 ^{o}C, the ice melting point. The fit (solid line) in Fig. 4.2 gives A = 140 ± 10 (nm) and B = 41 ± 4 (nm). These thickness values agree well with those found by proton channeling[5] and are about twice those reported in an AFM study.[10]

To quantify the adhesive interaction, we integrated the approach curves in Fig. 4.1a to obtain the work of adhesion at different temperatures. Scaled in absolute magnitude, these values agree very well with those obtained from the separation of two ice surfaces by Hosler, et al.[18] Of course, both measurements have in common the interaction with the ice L-LL. The attractive force must result from the wetting of the hydrophilic tip by the L-LL, as was suggested earlier in atomic force microscopy (AFM) measurements.[10,11] As a first approximation, the behavior of the peak attractive force, commonly referred to as the "pull-off force" when measured by an unstable force sensor like that of the AFM, would be expected to behave as

described, for example, by a Laplace-pressure analysis. For the tip making contact with a liquid surface, the force should be described by the relationship,[19]

$$F = -4\pi R\gamma_{LV}\cos\theta, \tag{1}$$

where γ_{LV} is the surface energy of the liquid-vapor interface, θ is the contact angle of the liquid with the tip and R is the tip radius. We do not have an accurate value for the L-LL/glass tip contact angle, but assume that it should to be close to 0°.

Under this assumption, Eq. 1 predicts a meniscus attractive force more than an order of magnitude larger than those shown in Fig. 4.1. However, Eq. 1 is not appropriate to the present situation. We are not making contact with a liquid surface, where the meniscus is formed by shear flow along the tip surface from the bulk of the liquid. Rather, in our case, we can only have lateral flow along the ice surface involving a very thin L-LL, and the ratio of the tip radius to the layer thickness is almost a factor of 4000 for the thickest film at -10 ^{o}C. Thus, in order to achieve the equilibrium "Laplace" force of Eq. 1 would require the flow of L-LL molecules very far from the tip contact. In addition, this flow would involve a "liquid" film only tens of nm thick, both of which seriously limit the growth rate of the contact area, a situation aptly described as the formation of a "frustrated" capillary.

The formation of such a frustrated capillary is also revealed in the dependence of force profiles on tip speed. Figure 4.3(a) shows the normal force behavior as the tip approaches the surface at speeds varied by a factor of ~5. As expected, the slower speed shows the largest adhesive force, since it allows the accumulation of

more L-LL in the frustrated capillary. The changes are rather small but the time that the tip is in contact with the L-LL, even in the slowest case at -10^{o}C, is only about 200 ms. Unfortunately, we were not able to do a true "creep" measurement to obtain accurate relaxation times for the L-LL because of the rapid recession of the ice surface due to sublimation. Under our experimental conditions, the ice surface recedes at a rate of approximately 10nm/s, which also creates a certain amount of surface instability. This instability at the junction gives rise to a significant noise level in the normal force signal. Attempts to stabilize the rate of surface recession by raising the relative humidity resulted in the rapid micron-level growth of a complex array of interconnected crystallite structures, further interfering with the sensitive measurements of the interfacial mechanical properties. In addition, efforts to stabilize the ice recession by covering the surface with various organic liquids also proved unsuccessful.

We now turn to the behavior of the lateral friction force for the interfacial layer as a function of temperature, as summarized in Fig. 4.1(b). First, note that the friction force begins its rise at a point well within the overall L-LL, reaches a peak very near the adhesive-force maximum and then rapidly decreases as the normal force begins its repulsive rise. This behavior is reminiscent of that found in several earlier studies involving the interfacial water layer confined at the nm level between various hydrophilic surfaces.[20,21] The decrease in friction force is accompanied by a rapid fall in the phase of the synchronous signal, implying that the tip compliance is coming into play. As the repulsive normal force rises the tip begins a "stick-slip"

type behavior as it burrows into the ice surface, giving rise to a falling phase toward 0^o.

As in the earlier studies, viscosity values for the "interfacial" water can be approximated through the use of an equation tailored for such conditions by Feibelman:[22]

$$F_\eta = 2\pi\eta\omega x_0 R \ln(\frac{D}{2w}),$$

(2) where η is the viscosity, ω the angular dither frequency, x_0 is the dither amplitude, R is the tip radius, 2w the total interphase-layer thickness and D the level of tip penetration into the interfacial layer. It is assumed in deriving Equation (2) that the viscosity does not vary with distance from the solid-ice surface and assumes the no-slip boundary condition at both interacting surfaces. Again, notice in comparing Figs. 4.1a and 4.1b, that the rise in friction involves an interfacial layer that is thinner than the L-LL itself and both thicknesses decrease as the temperature is reduced until at -30^o it is difficult to delineate the two. Fitting the Feibelman equation to the -10 ^{o}C friction results in a viscosity value of 220 Pa·s, almost $2.5x10^5$ times larger than that of bulk water or a little over $6x10^4$ times that of super-cooled water.[23] These figures are, of course, rough estimates because of the inherent noise level created by the unstable ice surface and become even worse at the lower temperatures. However, it would appear from the general rate of friction-force increase in this area, that the value of viscosity is remaining essentially constant with temperature. Previous attempts at measuring the viscosity of the L-LL include using shear rheology techniques, which yielded an viscosity values of 1.5-

70 Pa·s,[24] as well as approach speed dependent AFM measurements which found that the viscosity of the L-LL to be at least a factor of 300 greater than that of water (~0.89 mPa·s). These measurements are not without detractors, as many previous authors have assumed that the upper limit of the viscosity of L-LL is that of super-cooled water, which is at most, ~4x the viscosity of bulk water.[7,23,25] The viscous nature of the L-LL is more clearly revealed in the lateral force measurements taken at several lateral-tip speeds, Fig. 4.3(b). The lateral force increases with tip speed, although not exactly according to the` linear relationship expected from a pure viscous response. However, the accurate characterization of this "frustrated-capillary" behavior involves a rather sophisticated hydrodynamic model and is certainly beyond the scope of this contribution.

The lateral force, after contact with the solid-ice substrate, rises in direct proportion to the normal force and, in fact, appears in direct proportion, confirming that the behavior is attributable to the properties of solid-ice surface itself. At the maximum applied force of 5 μN in the -10^{o}C data, the stress applied to the "solid" ice surface is approximately 800 GPa. At this stress, the tip penetrates the solid surface by about 10nm, while the lateral force has a peak value of ~0.4 μN. The situation is a nanoscopic version of the artic explorer's use of crampons for climbing on ice, where multiple asperities penetrate the L-LL and deform the substrate ice resulting in greatly increased traction. In the present case, we have a crampon with only one asperity and the lateral force increases in direct proportion to the normal force. This behavior is often seen in multiple asperity situations and

results in the commonly encountered “Amonton” behavior, i.e., with the friction force directly proportional to the normal force and the proportionality constant defined as the coefficient of friction.

4.4 Conclusions

We have directly shown that a L-LL exists on the surface of ice, with a thickness that varies with temperature as described by a thermodynamic model.[26] This layer gives rise to an attractive force characteristic of a “frustrated capillary”, since the water source to build the capillary involves the axial flow along the ice surface of a very thin, viscous layer. W also find that this layer has a viscosity significantly larger than that of bulk water varying only slightly with temperature. In conclusion, it is compelling to speculate on what the present results contribute to the age-old question as to just why ice is so slippery.[27]

Faraday was the first to suggest the existence of a L-LL on the surface of ice, but was voted down in favor of pressure melting, which held sway for almost a century. At present, it is widely accepted that friction heating is the origin of the effect.[28] However, the existence of the L-LL has been well established in many careful experiments and is clearly present at the surface in the absence of friction. In addition, the common experience of walking on glare or smooth ice clearly shows that pre-sliding is not necessary in order to discover that the erect position can be unstable.

Friction at general interfaces normally involves multi-asperity contacts which extends to the atomic level, as illustrated by the slip friction seen in the shear motion between atomic planes in, for example, graphite or mica. [29] The effect results from the lateral force required to overcome both the adhesive interaction and the mechanical interlocking of the asperity-asperity contacts. [29] This is dramatically demonstrated by the fact that the static coefficient of friction is always greater than that of the "dynamic coefficient"; once the lateral motion sets in, the interaction is more limited and involves contacts between the asperity *peaks* reducing both the adhesive and interlocking effects. It is also the root cause of the commonly observed "Amonton"-behavior, where the friction force is directly proportional to the normal force. [30]

Lubricants for most surfaces are generally viscous, thin-film liquids, able to separate the asperity surfaces with a viscous force that depends on sliding velocity. With respect to this general model, ice with its naturally occurring, viscous L-LL is perhaps the premier example of a "self-lubricating" material, when supporting contact with ordinary surfaces e.g., ice skates. Contact with these surfaces further encourages the maintenance of the L-LL due to the effect of ice creep, where a weight placed on the ice slowly penetrates the surface.[31] In addition, the L-LL has a smoothing effect on the ice surface[32] and sublimation (strictly speaking, evaporation from the L-LL) adds an additional water-vapor boundary layer, concentrated near the surface by the surrounding atmosphere, that could further aid in separating the sliding surface from that of the bulk-ice substrate.

Finally, our results indicated only a very thin L-LL at -30 ^{o}C and leaves open the question as to what the ice surface is like at very low temperatures? A strong hint can be found in the writings of Edward Wilson, Robert Falcon Scott's chief scientist during his final visit to the Antarctica. Scott had earlier described skiing easily at -30 ^{o}C, while Wilson described the snow surface as "sand like" at -46 ^{o}C, presumably resulting from the complete absence of the L-LL.[27]

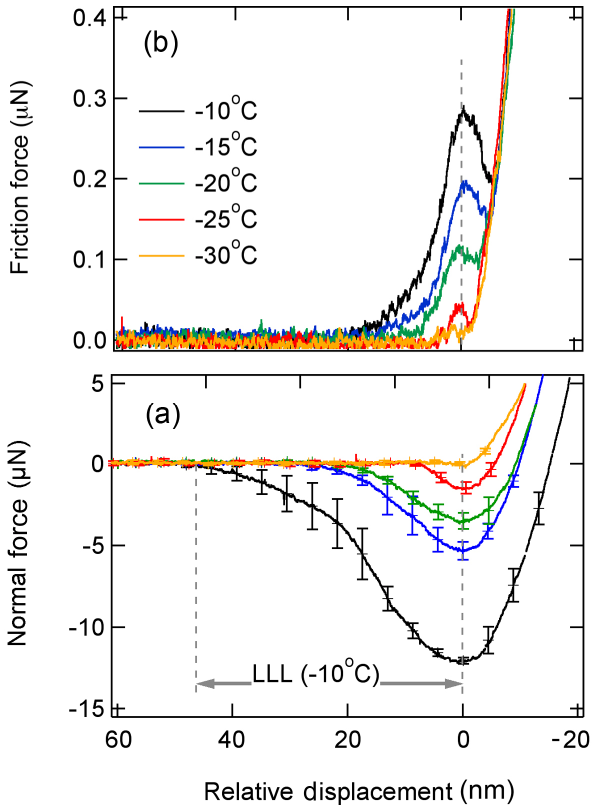

Figure 4.1. The temperature dependence of the normal (a) and frictional (b) force profiles on ice. The grey dashed lines are the approximate points of contact with the L-LL and the underlying ice surfaces.

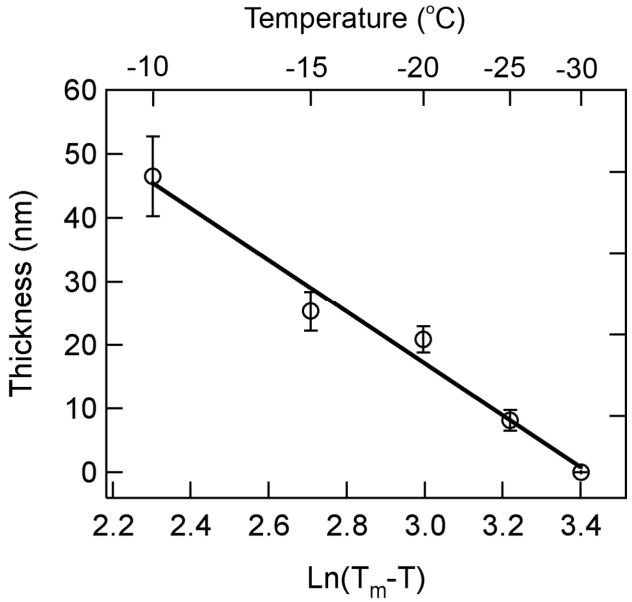

Figure 4.2. Temperature dependence of the L-LL thickness on ice. Error bars represent the standard deviation over 5 measurements.

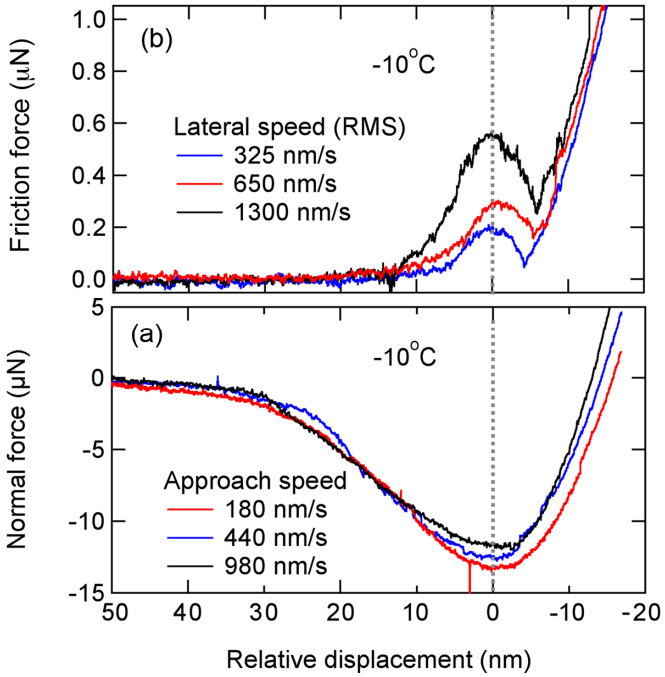

Figure 4.3. (a) Approach speed dependence on the adhesion of the L-LL at -10°C. (b) Lateral tip speed dependence of friction forces on ice at -10°C. Grey dashed line is the approximate point of contact.

4.5 References

1. Dash, J. G. *Science* **1989**, *246*, 1591.
2. Takagi, S. *J. Colloid Interface Sci.* **1990**, *137*, 446.
3. Bluhm, H.; Ogletree, D.F.; Fadley, C.S.; Hussain, Z.; Salmeron, M. *J. Phys. Condens. Matter* **2002**, *14*, L227-L233.
4. Dosch , H.; Lied, A.; Bilgram, J. H. *Phys. Rev. Lett.* **1994**, *72*, 3534.
5. Golecki, I.; Jaccard, C. *Phys. Lett. A* **1977**, *63*, 374.
6. Elbaum, M. Lipson, S.G., Dash, J.G. *Journal of Crystal Growth* **1993**, *129*, 491-505.
7. Gilpin, R.R. *J. Colloid Interface Sci.* **1980**, *77(2)*, 435-448.
8. Wilson, P.W.; Arthur, J.W.; Haymet, A.D.J. *Biophysical Journal* **1999**, *77*, 2850-2855.
9. Doppenschmidt, A.; Kappl, M.; Butt, H.-J. *J. Phys. Chem. B* **1998,** *102*, 7813-7819.
10. Doppenschmidt. A.; Butt, J.-H. *Langmuir* **2000,** *16*, 6709-6714.
11. Petrenko, V. F. *J. Phys. Chem. B* **1997**, *101*, 6276.
12. Pittenger, B.; Fain, Jr., S. C.; Cochran, M. J.; Donev, J. M. K.; Robertson, B. E.; Szuchmacher, A.; Overney, R. M. *Phys. Rev. B* **2001**, *63*, 134102.
13. Bluhm, H,; Inoue, T.; Salmeron, M. *Phys. Rev. B* **2000**, *61*, 7760-7765.
14. Dash, J. G.; Haiying, F.; Wettlaufer, J. S. *Rep. Prog. Phys.* **1995**, *58*, 115.
15. Li, Y.; Somorjai, G. A. *J. Phys. Chem.* **2007,** *111(27)*, 9631-9637.
16. Houston, J. E.; Michalske, T. A. *Nature* **1992**, *356*, 266-267.

17. Houston, J. E.; Joyce, S. A.; *Rev. Sci. Inst*. **1991**, *62-3*, 710-715.

18. Hosler, et al. *Disc. Faraday Soc.* **1961**, *30*, 200.

19. Israelachvili, J. *Intermolecular and Surface Forces*; Academic Press: London, 1992.

20. Major, R.C.; Houston, J.E.; McGrath, M.J.; Siepmann, J.I.; Zhu, X.-Y. *Phys. Rev. Lett.* **2006**, *96*, 177803.

21. Goertz, M.; Houston, J. E.; Zhu, X.-Y. *Langmuir* **2007**, *23*, 5491-5497.

22. Feibelman, P. J. *Langmuir* **2006**, *22*, 2136-2140.

23. Hallett, J. *Proc. Phys. Soc***. 1963**, *82(530)*, 1046.

24. Jellinek, H. H. G. *Colloid Interface Sci.* **1967**, *25*, 192-205.

25. Bluhm, H,; Inoue, T.; Salmeron, M. *Phys. Rev. B* **2000**, *61(11)*, 7760-7765.

26. Weyl, W. A. *J. Coll. Sci.* **1951**, *6*, 389.

27. Rosenberg, R. *Physics Today* **2005**, *58(12)*, 50-55.

28. Bowden, F. P.; Hughes, T. P. *Proc. Roy. Soc. London A.* **1939**, *172*, 280.

29. Persson, B. N. L. *Sliding Friction: Principles and Applications*; Springer: Berlin, 2000.

30. Perrson, B. N. J.; Sivebaek, I. M.; Samoilov, V. N.; Zhao, K.; Volokitin, A. I.; Zhang, Z. *J. Phys. Condens. Matter.* **2008**, *20*, 395006.

31. Telford, J. W.; Turner, J. S. *Philos. Mag.* **1963**, *8*, 527.

32. Hosler, C. L.; Hallgren, R. E. *Disc. Faraday Soc.* **1960**, *30*, 200.

Chapter 5. Density Dependent Friction of Lipid Monolayers

5.1 INTRODUCTION

Thin films have long been studied as boundary lubricants between two solid surfaces. Recent studies have focused on self-assembled monolayers (SAMs) due to their importance as model systems and their applications as boundary lubricants for microscale and nanoscale devices, e.g., micro- or nano-electromechanical systems (MEMS or NEMS).[1,2] Tribological properties of alkanethiol and alkylsiloxane SAMs have been extensively studied by force microscopies to address the dependences of frictional properties on molecular chain length,[3,4,5,6] end group chemistry,[3,7] tip scan velocity,[8] contact area,[9] and anisotropy of crystallographic directions.[10] These SAMs are usually characterized by crystalline order and close packing. In fact, deviation from a well-ordered molecular lattice is believed to be the main reason for increased friction in SAMs, due to the increased freedom of motions for the adsorbed molecules and, thus, more energy dissipation during lateral motion.[11]

In contrast to strongly adsorbed SAMs, much less is known about frictional properties of weakly adsorbed molecular films, e.g., Langmuir-Blodgett (LB) monolayers that lack the crystalline order of SAMs. In biological systems, weakly adsorbed phospholipid monolayers are believed to be common in bio-

lubrication.[12,13] Weakly adsorbed perfluoroalkyl fatty acid monolayers are also critical to the development of the most successful MEMS product on the market today.[14] From a mechanistic perspective, the LB monolayer is an attractive model system for obtaining a molecular level understanding of friction because it allows us to vary molecular density over a much broader range than is possible in SAM systems. Here we report an experimental study, using interfacial force microscopy (IFM)[15,16], of the tribological properties of lipid monolayers over a reasonably broad density range prepared via the LB technique. We show that the normal and friction-force profiles in the compression region can be well-described by the Johnson-Kendall-Roberts (JKR) contact-mechanics model[17] and that the frictional force and friction shear strength scale inversely with the molecular density of the lipid layer.

5.2 EXPERIMENTAL

We investigate the two lipid molecules shown in figure 5.1, 1,2-Dilauroyl-sn-Glycero-3-Phosphocholine (DLPC) and 1,2-Distearoyl-sn-Glycero-3-Phosphocholine (DSPC) (Avanti Polar Lipids, Inc. Alabaster, AL). Isotherms show that DLPC exists in the liquid-expanded (LE) phase over the entire pressure range studied here, conversely DSPC remains in the liquid-condensed (LC) phase over the entire pressure range studied (figure 5.1). We use oxide-terminated silicon wafers as substrates for the lipid LB monolayers. The silicon surface is freshly cleaned in boiling Piranha (3:1 conc. H_2SO_4/ 30% H_2O_2; Caution! Piranha solution is a strong oxidant and reacts violently with organic substances) for one hour and thoroughly

rinsed with 18 MΩ·cm H_2O. Pressure-area isotherms and LB depositions in increments of 10 mN/m were performed using a commercial LB trough (Nima Model 612D, UK) until film collapse. Freshly prepared lipid monolayers are characterized by IFM at room temperature and a relative humidity of ~15%. We record normal and lateral force profiles as previously described[18] using a W tip (radius 1.3 μm, determined from Scanning Electron Microscopy). We obtain the lateral force simultaneously with the normal force by driving the sensor laterally with a ~2 nm peak-to-peak dither at 100 Hz and synchronously detecting the force signal with a lock-in amplifier. Force profiles are repeated 3 times in 3 separate spots, allowing for averaging of 9 independent force profiles per monolayer. The dissipative component of the lateral force signal in quadrature with the drive is used as the friction signal.

5.3 RESULTS & DISCUSSIONS

Figure 5.2 shows a typical normal (A) and friction-force (B) profile for the LB monolayers (DLPC @ 40 mN/m). The fits are to the JKR contact mechanics model, which describes the contact area and deformation as a function of normal force.[17] In order to determine which, if any, contact mechanics models are appropriate, we use the α parameter of Carpick et al.[19] and fit friction as a function of normal force, figure 5.2B. We find that fits to all the lipid monolayers yield an α parameter[19] of 0.9-1.1, indicating that the JKR model (α =1) is most appropriate. This is in contrast

to a previous AFM study which showed that force measurements on LB films could not be adequately described by contact mechanics models.[20]

Most contact mechanics models, such as JKR, are derived from the Hertz theory.[21] These models are only strictly valid for linearly elastic materials, a condition not likely met over the full range of forces probed for the phospholipid monolayers. However, in this case, we find that the JKR model accurately describes the nature of contact after a small initial compression of the LB film. This can be seen in Figure 5.2A in the analysis of the location of F_c, the experimental critical force (maximum adhesion), a good indication of tip/film contact. The location of the critical force is ~5 Å before the contact predicted by the JKR model and ~10 Å before the fit begins to accurately describe the experimental data. This offset results from the fact that JKR theory assumes adhesive forces are very short-ranged, effectively acting only when contact occurs. These normal force features are characteristic of all lipid monolayer samples investigated. In figure 5.2A we observe the normal force after contact slowly rises for ~6 Å and then rises sharply to meet the JKR model. The composite modulus values obtained from JKR fits for the compressed lipid monolayers in the tip/film/substrate combination are 33±4 GPa for DLPC and 49±6 GPa for DSPC; these values are, within experimental uncertainty, independent of surface pressure (10-50 mN/m) used in LB deposition and are much larger than the expected value of $\leq$ 1 GPa for the lipid monolayer itself.[22] Using the JKR model, we can estimate an effective modulus of the lipid film by fitting the first 10 Å of compression, which is dominated by response of the relatively soft LB film.

The fit gives an effective modulus of ~1 GPa for each lipid film, which is also observed to be independent of deposition surface pressure. Upon further compression, the composite modulus of the contact increases, and the force profile is well described by JKR theory (gray curve in figure 5.2A). We have also measured the mechanical properties of the control interface with no LB film; this measurement provided a composite modulus of 110 GPa, much higher than those obtained for the tip/film/substrate combination.

We conclude that the film is confined within the contact junction during compression, i.e., not squeezed out. The repeatability of our experiment in a single spot reveals that the lipid monolayer completely recovers during the time scale (~1 minute) between force profiles. Note that we observe no evidence of discontinuity in force profiles corresponding to lipid membrane rupture as seen in a previous AFM study.[20] This can be attributed to size differences of the tips used in measurements. In the previous AFM experiment, the tip radius of curvature was a few nanometers, more than two orders of magnitude smaller than that used in our IFM experiment. The maximum normal stress of ~10 MPa in IFM measurement is much smaller than the value for membrane rapture of 250MPa estimated from AFM experiments.[23]

Note that the attractive region of the normal force may include contributions from van der Waals, electrostatic, and capillary forces. A further complication is that weakly adsorbed lipid molecules may respond dynamically and reorient under attractive forces. However, we do not observe out of contact friction in the adhesive

region. Due to these complications, we do not attempt to quantitatively analyze the force profiles in the attractive region.

Having addressed the normal force profile, we turn to the frictional force, figure 5.2B. The non-linear behavior of the friction vs. normal force plot and excellent agreement with JKR theory suggests a true single asperity contact.[9] Bowden and Tabor (BT)[1] showed that friction force is related to contact area through $F_f = \tau A$ where A is the contact area and τ is the friction shear strength. The contact area is a function of normal force as described by the JKR model.[19] We find that the experimental data in figure 5.2B is well described by the BT equation with a small friction force offset, Δ_f ($|\Delta_f| \leq 4$ nN). The offset produces a better fit (gray curve in figure 5.2B) than the BT equation alone. Δ_f is negative for DLPC and positive for DSPC monolayers. Though, the meaning of this small offset is unclear, it suggests that the combination of fits (BT and JKR) overestimate the friction (contact area) for the LE phase of the DLPC monolayer and underestimates that for the LC phase of the DSPC film. Further work is required to elucidate the origin of this offset by expanding the range of experimental conditions. After a small initial compression the excellent fit in figure 5.2B indicates that friction shear strength is pressure-independent.[24] Using the above fitting method, we obtain the friction shear strength for the tip/film/substrate combination of each DLPC and DSPC deposition. This allows us to compare shear strength vs. monolayer surface pressure (and thus, molecular-area).

Figure 5.3 shows a plot of friction shear strength as a function of molecular area for both phospholipid monolayers. Here, the molecular area is the surface area per lipid molecule taken from the isotherms shown in figure 5.1. Unlike the composite modulus for the compressed tip/film/substrate interface, we find a nearly linear relationship between friction shear strength and molecular area. Currently, we do not attempt to justify why this relationship is linear, which may only be an empirical result. This trend is more obvious for the LE phase DLPC monolayer than the LC phase DSPC monolayer, due to the much larger variation in molecular area of the former.

We now discuss the molecular origins for this observation. Surface sensitive spectroscopic measurements and computational simulations have revealed the major frictional dissipation mechanisms in the wear-less regime for monolayers confined between two sliding interfaces. These include intra-molecular vibrations, molecular tilting, and other conformational changes.[11,25,26,27] For a nearly close-packed SAM, friction has been found to correlate closely with disorder. Deviation from two-dimensional crystalline-order due to shorter molecular backbones or bulkier terminal groups is believed to result in more conformational freedom for the adsorbed molecules and, thus, more channels for energy dissipation (i.e., higher friction) during sliding motion. The results in figure 5.3 shows the influence of conformational freedom on friction in nearly close-packed SAMs can be extended to a much broader coverage range for LB lipid monolayers, with surface molecule density varying by nearly a factor of two. Note that each lipid molecule consists of

two alkyl chains (18 or 12 carbon each for DSPC or DLPC, respectively). At the smallest molecular area achievable in our LB monolayers, the area per DSPC molecule (two alkyl chains) is 42 $Å^2$. This alkyl packing density is close to that in a typical alkanethiol SAM on Au.[11] Similar relationships between packing density and friction of a boundary lubricant has been observed numerous times, though previous experiments have been limited to strongly bound monolayer films. [3,4,5,6,28]

The friction shear strength for the close-packed, LC phase DSPC monolayer is much lower than that of the LE phase DLPC monolayer. This effect can be explained by both the aforementioned larger variation in packing density of LE phase film and the dramatic increase in ordering between the different phases of LB films. Previous sum frequency generation experiments have shown that the first order transition between LE and LC phase films produces a "strong reorientation" of the alkyl chains of the surfactants.[29,30] The disorder in the LE films influences the ability to create internal conformational defects and changing molecular tilts, which is strongly opposed in well ordered films.[25]

A semi-quantitative way of expressing conformational freedom, and ease of ordering the surfactant film, is compressibility. The compressibility (C), a uniquely measurable quantity of Langmuir films, is defined as $C = -(1/A)*(dA/d\pi)$ where A is the average area per molecule and π is the surface pressure.[31,32] C^{-1} is the effective 2-D compressive modulus of the monolayer. The compressive modulus describes how much 2-D strain per unit of 2-D stress is needed to pack surfactant molecules closer together at the air/water interface. We have converted isotherms (π vs. A) of

each lipid monolayer to the compressive modulus vs. *A*, shown in figure 5.3. Assuming that LB transfer preserves the trends in compressibility, the compressive modulus increases with decreasing molecular area, indicating an inverse relationship between friction shear strength and compressive modulus.

5.4. CONCLUSIONS

We successfully use LB monolayers of lipids as model systems to establish the relationship between molecular density and frictional force for a weakly adsorbed boundary lubricant. We have found that both normal and friction forces are well described by the JKR and BT models, suggesting a single asperity contact with constant friction shear strength is formed in our experiments. The friction shear strength of the monolayer film is proportional to the surface area (42-74 $Å^2$/ molecule) occupied by each molecule over a relatively broad range. The increase in frictional force or shear strength with increasing molecular area can be attributed to the increased conformational freedom of the molecules, and the resulting number of energy-loss modes available.

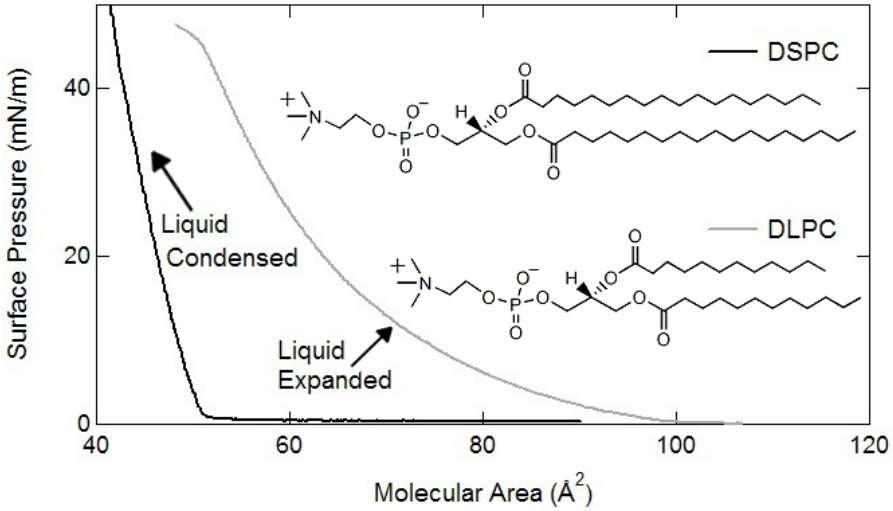

Figure 5.1. Isotherms showing surface pressure vs. molecular area for DLPC (grey line) and DSPC (black line) monolayers on oxide terminated silicon. Molecular Structure of DLPC and DSPC are also shown.

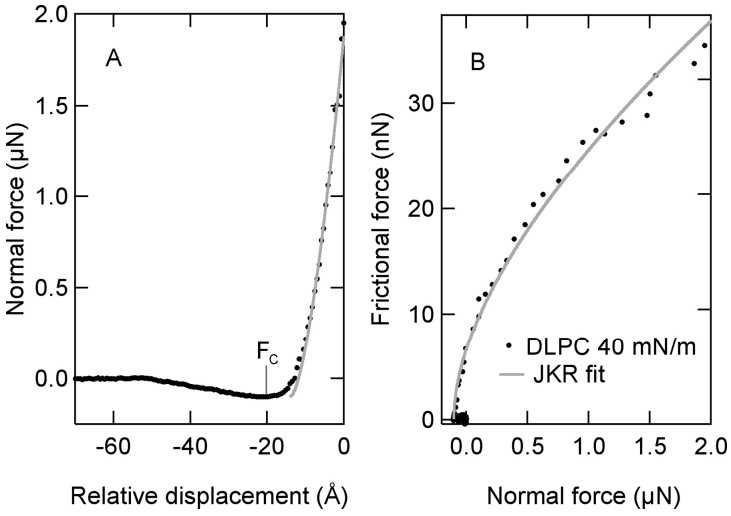

Figure 5.2. Normal force profile (A) and frictional force vs. normal force (B) for a DLPC monolayer deposited on a native oxide terminated Si surface via the LB technique at a surface pressure of 40 mN/m. Fits are to the JKR contact mechanics model.

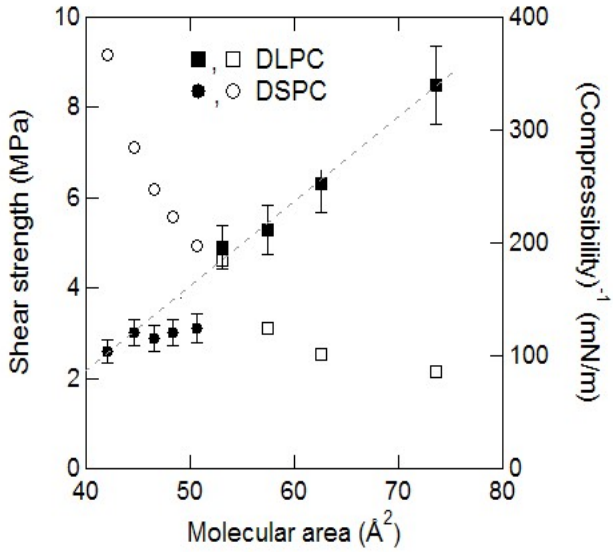

Figure 5.3. Friction shear strength (filled symbols) and Compressibility^{-1} (open symbols) vs. molecular area for DLPC (squares) and DSPC (circles) monolayers on oxide terminated silicon. Dashed line is a guide to the eye for the trend in friction shear strength.

5.5 References

1 Bowden F.P.; D. Tabor, D. *The Friction and Lubrication of Solids*; University Press: Oxford, 2001.

2 Bhushan, B. *Nanotribology and Nanomechanics*; Springer-Verlag: Berlin, Heidelberg, 2005.

3 Brewer, N.J.; Beake, B.D.; Leggett, G.J. *Langmuir* **2001**, *17*, 1970.

4 Lio, A. D.; H. Charych, D.H.; Salmeron M. *J. Phys. Chem. B* **1997**, *101*, 3800-3805.

5 Brewer, N.J.; Foster, T.T.; Leggett, G.L.; Alexander, M.R., McAlpine, E. *J. Phys. Chem. B* **2004**, *108*, 4723-4728.

6 Chandross, M.; Webb, M.E.B.; Stevens, M.J.; Grest. G.S.; Garofalini, S.H. *Phys. Rev. Lett.* **2003**, *93*, 166103.

7 Houston, J.E.; Doelling, C.M.; Vanderlick, T.K., Hu, Y.; Scoles, G. Wenzl, I.; Lee, T.R. *Langmuir* **2005**, *21*, 3926-3932

8 Chen, J.; Ratera, I.; Park, J.Y.; Salmeron, M. *Phys. Rev. Lett.* **2006**, *96*, 236102.

9 Gao, J. Luedtke, W.D.; Gourdon, D.; Ruths, M.; Israelachvili, J.N.; Landman, U. *J. Phys. Chem. B.* **2004**, *108(11)*, 3410.

10 Carpick, R.W.; Sasaki, D.Y.; Burns, A.R. *Tribology Letters* **1999**, *7*, 79

11 Salmeron, M. *Tribology Lett.* **2001**, *10*, 69.

12 Hills, B. A. *Proc. Inst. Mech. Eng.* **2000**, *H214*, 83–94.

13 Sarma, A. V.; Powell, G. L.; LaBerge, M. *J. Orthop. Res.* **2001**, *19*, 671–676.

14 Hornbeck, L. J. *US Patent 5602671* (1997).

15 Houston, J. E.; Michalske, T. A. *Nature* **1992**, *356*, 266-267.

16 Houston, J. E.; Joyce, S. A.; *Rev. Sci. Inst*. **1991**, *62-3*, 710-715.

17 Johnson, K. L.; Kendall, K.; Roberts, A. D. *Proc. R. Soc. London Ser. A* **1971**, *324*, 301.

18 Goertz, M. P.; Houston, J.E.; Zhu, X.-Y. *Langmuir* **2007**, *23*, 5491 - 5497.

19 Carpick, R.W.; Ogletree, D.R.; Salmeron, M.J. *J. Colloid Inter. Sci.* **1999**, *211*, 395.

20 Oncins, G.; Torrent-Burgués, J.; Sanz, F. *Tribology Letters* **2006**, *21(3)*, 175.

21 Hertz, H. *J. Reine Angew. Math* **1882**, *92*, 156.

22 Zanoni, R.; Naselli, C.; Bell, J. Stegeman, G.I.; Seaton, C.T. *Phys. Rev. Lett.* **1986**, *57(22)*, 2838.

23 Franz, V.; Loi, S.; Müller, H.; Bamberg, E.; Butt, H.-J. *Colloids and Surfaces B: Biointerfaces* **2002,** *23*, 191–200.

24 Piétrement, O.; Troyon, M. *Langmuir* **2001**, *17*, 6540-6546.

25 Du, Q.; Xiao, X.-d.; Charych, D.; Wolf, F.; Frantz, P.; Shen, Y.R., Salmeron, M. *Phys. Rev. B.* **1995**, *51(12)*, 7456.

26 Mikulsi, P.T.; Harrison, J.A. *J. Am. Chem. Soc.* **2001**, *123*, 6873-6881.

27 Siepman, J.I.; McDoland, I.R. *Phys. Rev. Lett*. **1993**, *70(4)*, 453.

28 Lee, S.; Shon, Y.-S.; Colorado, R .Jr.; Guenard, R.L. Lee, T.R.; Perry. S.S. *Langmuir* **2000,** *16*, 2220-2224.

29 Guyot-Sionnest, P. Hunt, J.H.; Shen, Y.R. *Phys. Rev. Lett.* **1987**, *59(14)*, 1597.

30 Ma, G.; Allen, H. *Langmuir* **2006**, *22*, 5341-5349

31 Behroozi, F. Langmuir **1996**, 12, 2289-2291.

32 Tshoegl, N.W. *J. Colloid Sci.* **1958**, *13*, 500-507.

Chapter 6. Nanomechanical Contrasts of Gel and Fluid Phase Supported Lipid Bilayers

Reproduced with permission from [Journal of Physical Chemistry B], submitted for publication

6.1 INTRODUCTION

Amphiphilic lipid molecules are a structural component within cell plasma membranes. These molecules self-assemble into a supermolecular interface which serves as a cellular barrier and forms a matrix hosting biomolecules such as steroids and membrane proteins. Cell membranes act as a complex composite fluid exhibiting dynamic behavior and lateral inhomogeneities that are intricately involved in cell functions (1). The structural complexity of the cell membrane is reflected in the mechanical diversity that is intimately related to cell function. Past studies on the mechanical properties of cell membranes have relied on physical probes on the macroscopic and microscopic scales, such as osmotic stress (2) and micropipeting (3), that probe average mechanical properties. The development of supported lipid bilayers (SLBs) (4) as a mimic of the cell membrane, and the advent of the atomic force microscope (AFM) (5) has enabled extensive studies of the model cell membrane on the nanoscopic scale (6,7). The AFM technique promises to resolve the structural complexity and the associated physical properties on a nanometer scale based on imaging and localized force probing. These studies have greatly advanced our understanding of the model cell membrane (for a review see refs. 6,8). One limitation of the AFM technique in probing the mechanical

properties of soft interfaces is the compliance of the cantilever sensor. This compliance results in mechanical instabilities such as the “jump-to-contact.” These instabilities complicate the analysis of both elastic and plastic deformation of SLBs. We use the Interfacial Force Microscope (IFM) to quantitatively establish the mechanical properties and, particularly, explore structure-property relationships. We compare and contrast the mechanical properties of SLBs in both the ordered gel phase and the disordered fluid phase. The IFM uses a self-balancing, force-feedback sensor which eliminates the mechanical instability problem and allows measurements of normal and lateral frictional forces throughout the entire range of interfacial separation (9,10). As no stored energy is released from the IFM sensor to the SLB during plastic relaxation events, this allows for careful measurement of failure of SLBs. We measure both the elastic response and plastic yield of these films as well as their frictional properties. We find significant differences in both the yield stress and recovery timescales between the two SLBs. These differences can be accounted for by differences in the lateral mobility of the lipid molecules.

6.2 EXPERIMENTAL

We form the gel and fluid phase SLBs using the vesicle fusion method from two lipid molecules (Fig. 6.1), 1,2-Distearoyl-sn-Glycero-3-Phosphocholine (DSPC) and 1,2-Dilauroyl-sn-Glycero-3-Phosphocholine (DLPC) (Avanti Polar Lipids, Inc. Alabaster, AL), on oxide-terminated silicon wafers. These two lipids molecules have the same hydrophilic headgroup and glycerol linker, differing only by the

length of their hydrophobic alkyl tails. The silicon surfaces are cleaned by boiling in Piranha (3:1 conc. H_2SO_4/ 30% H_2O_2; Caution! Piranha solution is a strong oxidant and reacts violently with organic substances) for one hour and thoroughly rinsed with 18 MΩ·cm H_2O. Lipids dissolved in chloroform are first dried under N_2 for ~1 hour and suspended in aqueous buffer (100mM NaCl, 50mM Tris, 5mM $CaCl_2$, pH~7.5) and sonicated for ~1min to create a 100mM vesicle suspension. We prepare solutions of small unilamellar vesicles (SUV) by extruding the lipid solution 11 times through a 100 nm polycarbonate filter. A sufficient amount of the SUV solution is then incubated with a clean silicon surface for three hours at room temperature. Excess vesicles are removed from the surface by flushing with copious amounts of water. The mobility/immobility of DLPC/DSPC SLBs is verified by fluorescence recovery after photobleaching (FRAP, not shown). As expected, fluid phase DLPC SLB shows high lipid mobility with a lateral diffusion constant of ~2 $\mu m^2/s$ while the gel phase DSPC does not.

We use IFM to characterize freshly prepared SLBs under water at room temperature using a Tungsten (W) tip with a 500 nm spherical radius (determined by Scanning Electron Microscopy). We obtain the lateral force simultaneously with the normal force by driving the sensor laterally with a ~2 nm peak-to-peak dither at 100 Hz and synchronously detecting the force signal with a lock-in amplifier. Experimental details of the IFM have been described elsewhere (11).

6.3 RESULTS AND DISCUSSION

6.3.1 Mechanical Responses: gel vs. fluid

6.3.1.1 Contrasts in normal force profiles

The distinctively different mechanical properties of the two SLBs are revealed in normal force measurements. The top panel in Fig. 6.2 shows typical normal force profiles on a gel phase DSPC SLB. As the tip approaches the bilayer we measure a monotonic increase of repulsive force until ~2 μN; this region is indicative of a nearly elastic response. Beyond this region, the normal force plateaus for ~3 nm, corresponding to plastic deformation of the bilayer under the stress of the approaching tip. With further loading, the supported lipid bilayer is squeezed out of the contact area and the tip contacts the silicon substrate. At this point the repulsive force profile becomes identical to that of a bare Si control. The normal force profile upon retraction shows significant hysteresis and is much closer to that of the bare silicon surface than the approach profile. Clearly, the SLB does not recover on the time scale of the measurement (~ 1 minute). As shown below, no recovery is observed on much longer time scales.

The fluid DLPC SLB shows very different normal force responses (lower panel of Fig. 6.2). When the tip initially approaches the SLB, there is only a small region of repulsive response until ~0.3 μN. Beyond this point, the normal force decreases and becomes attractive, indicating that the fluid SLB has collapsed under the normal load. Since the measurement is carried out under water, and the formation of a normal capillary condensate meniscus is not possible, the attractive force must arise

from lipid assemblies bridging the tip-substrate gap. Further approach results in the contact of the tip with the silicon substrate. Upon retraction, the normal force profile shows hysteresis, but not as significant as for DSPC. The main features during retraction include an attractive and a repulsive region as during approach, however with a stretched length scale. This result suggests that the fluid SLB partially recovers as the tip is retracted from the surface. Further support for this interpretation is shown below.

6.3.1.2 Contrasts in membrane recovery

The mechanical contrast of the gel and fluid phase SLBs is obvious in the recovery time after indentation. Fig. 6.3 shows repeated force profiles at the same location for DSPC (top) and DLPC (bottom) SLBs. As expected for the solid-like behavior of the gel phase DSPC SLB, the thin film does not recover in subsequent force profiles after plastic deformation in the first approach. Normal force profiles in the second and third measurements show completely different behavior. Note that the length of time between measurements is ~ 10 minutes and each approach-retract cycle takes ~ 1 min. In contrast, the fluid phase DLPC SLB completely recovers from measurement to measurement. Within experimental uncertainty, the force profiles are identical for repeated measurements at the same location.

6.3.1.3 Contrasts in friction

The mechanical difference in the two SLB phases is also revealed in the friction force profiles, Fig. 6.4. The fluid DLPC SLB shows negligible friction force in the entire range of tip-SLB contact, while the gel DSPC SLB shows significant friction over the entire range of tip-SLB contact, including both the elastic and the plastic regions. The observation in Fig. 6.4, that fluidic DLPC SLB shows much less (if any) friction compared to the gel phase DSPC, is in direct contrast with our previous studies on supported monolayers (12). Experiments on monolayers of these films show the opposite trend: A DSPC monolayer shows less friction than that of a DLPC monolayer does.

Contrast between the friction forces observed in these two experiments is not unexpected. When probing monolayers, the tip directly contacts the hydrophobic tails of the lipids and the friction is proportional to the surface area occupied by and the associated conformational freedom of each lipid molecule (12). However, by performing experiments on SLBs underwater to maintain hydration, it is likely the slip plane changes. While the major energy dissipation mechanisms that creates sliding friction on monolayers occurs at the tip/lipid tail interfaces, sliding over the hydrated lipid headgroups may contribute to friction of bilayers. This phenomenon has been observed before with adsorbed surfactants under water (13).

The contrast in friction for DSPC vs. DLPC bilayers is attributed to the difference in both there mobility and mechanical strength. With a relatively low yield strength and high mobility, DLPC is easily displaced by the tip sliding through it and, while being stressed elastically, may even be able to slide along the substrate

surface with the tip. In comparison the low mobility limits the ability for DSPC to slide with the tip at light loads, while the high yield strength provides more resistance to the tip sliding through and displacing the SLB. Both of these effects lower the friction of the tip in contact with DLPC relative to DSPC, as it takes less energy to slide on/through the fluid phase SLB compared to the gel.

6.3.2 Quantitative Analysis

Having established the solid- and liquid-like behaviors for the two SLBs, we now turn to quantitative analysis. While no single model can describe force profiles (reproduced in Fig. 6.5) over the entire range of contact, we can identify four distinct regions: 1) an out-of-contact region; 2) an elastic region; 3) a plastic deformation or collapse region; and finally 4) an elastic region due to direct tip-silicon contact.

The tip-sample separation shown in Fig. 6.5 is a relative scale, where the "0" distance is only a reference point, without physical meaning. In the presentation, we line up the leading edges of the initial rise in normal force for the two force profiles for DSPC and DLPC. We define the bottom of the SLB as the position where the normal force starts to rise rapidly due to contact with the silicon substrate (terminated with silicon oxide and a hydration layer). For DSPC and DLPC SLBs, the turning points (boundary between regions 3 & 4) are at ~0.8 and 2.3 nm, respectively. The top of the SLB is defined at the position when the normal force initially begins its rapid rise, due to the elastic-response of each SLB. This position

is the boundary between regions 1 & 2 and is at ~ 5.2 nm. Thus, the thicknesses of the SLBs are 4.4 and 3.9 nm for DSPC and DLPC, respectively, consistent with those expected from the length of the lipid molecules used (14). Note that the separation of regions 1 & 2 is not abrupt. In the out-of-contact region 1, we observe a small but measureable repulsive force for both SLBs. We believe that the lack of abruptness in the transition from the non-contact to the contact regions results from long range and weak interactions due to thermal fluctuation and the dynamic roughness of the SLBs (15), the structured hydration layer (16) and adventitious adsorbed molecules (e.g., lipids) on the tip.

6.3.2.1 *DSPC: Elastic-Plastic*

In region 2, the tip comes into contact with the SLBs and deformation occurs. The repulsive force over the range of ~1.8 nm can be described by the Hertz model (gray curve) (17), which is valid for homogenous and linearly elastic materials. Thus, over a vertical strain equaling ~1/3 of the total thickness, the SLBs behave elastically. The fit gives a reduced modulus of 35 GPa. The reduced modulus is a composite value that includes deformation of the SLB, the hydration layer, the tip, and the underlying substrate. It is also of interest to compare this work to our previous studies of supported monolayer of the same lipid. The supported monolayers showed a similar force profile when stressed elastically and gave the same reduced modulus (33-49 GPa) (12).

Further deformation beyond 1.8 nm results in an abrupt transition to the plastic region 3 where the normal force remains constant with increasing strain. Based on the Hertz model for elastic deformation, the contact area is $A=\pi hR$, where h is deformation and R is the tip radius. At the point of elastic-to-plastic transition, the deformation is h_p = 1.8 nm and the normal force is F_p = 2.0 μN. This gives a yield stress of s_p = 710 MPa. We must point out, however, that the two-dimensional plastic behavior is not observed in IFM measurement under ambient conditions of a Langmuir monolayer of the same lipid supported on the oxide-terminated silicon surfaces as stresses of only >10 MPa were used in the previous experiment (12).

Plastic deformation of the DSPC SLB continues for 2.6 nm, until lipid molecules are mostly squeezed out of the contact area. At the end of region 3, we see another abrupt transition and the normal force rises rapidly. The normal force profile in region 4 is, within experimental uncertainty, identical to that of a bare silicon substrate. Fitting the force profile in region 4 with the Hertz model gives a reduced modulus of 110 GPa, which is very close to previously reported values for bare Si (18). The mechanical responses of the gel phase DSPC SLB to the approaching tip are summarized in Figure 6.6a.

6.3.2.2 *DLPC: Elastic-collapse*

For the fluidic DLPC SLB, tip-membrane contact leads to an initial rise in the normal force to a maximum value of ~ 0.3 μN. This rise tracks that of the gel phase DSPC, until the point where the normal force for DLPC abruptly decreases while

that of DSPC continues to rise. For DLPC, the very limited range of data before membrane collapse does not permit us to reliably carry out an analysis with the Hertz model, but the repulsive nature of the normal force suggests that the mechanical response is partly elastic. This can be attributed to the cohesive nature of the fluidic SLB. Since the two force profiles from DLPC and DSPC overlap until the point of divergence (h_c = 0.8 nm), we can use the fit to DSPC to approximate the contact area for DLPC. This gives a yield stress of s_c = 240 MPa for the DLPC SLB. This value is very close to the yield stress obtained by AFM for other fluidic phase SLBs (19), where Franz, et al. observed a yield stress of 259 MPa for the fluidic dioleoyloxypropyl-trimethylammonium chloride (DOTAP) SLB on mica. It is interesting to note that the AFM measurement used tip sizes ~10x smaller than that employed here for IFM. Thus, in our measurement, the number of molecules in the contact area is as high as ~100x more than those in AFM experiments. The same yield stress from both measurements indicates the importance of nearest neighbor interaction in determining local nanomechanical properties that are representative of those over a much larger scale.

For deformations > 0.8 nm, the fluidic DLPC SLB collapses, as evidenced by a decrease in normal force in region 3. The mobile lipid molecules are squeezed out of the tip/substrate contact area. Interestingly, the normal force even decreases to a negative value before the tip contacts the hard substrate surface. A possible explanation for this adhesion is that the fluidic lipid bilayer reforms around the tip, resulting in a “meniscus” like structure. The negative curvature of the lipid bilayer

bridging the tip and the silicon substrate gives rise to the adhesion. Figure 6.6b summarizes the mechanical responses of the fluidic DLPC SLB to the approaching tip.

6.4 SUMMARY

We use interfacial force microscopy to correlate mechanical properties with the two-dimensional phase behavior of supported lipid bilayers. Upon indentation by a 500 nm W tip, the gel phase DSPC SLB behaves as a thin solid film, with an elastic response at low load and two-dimensional plasticity above a threshold stress. Consistent with its solid character, the frictional force scales with the area of the tip-SLB contact and the deformed SLB does not recover within experimental time scale of minutes. In contrast, the fluid phase DLPC SLB behaves as a liquid with an initial elastic-like response at very light load and collapse of the thin film above a much lower threshold stress than DSPC, as well as almost no observed friction while in contact with the SLB. The relatively high mobility of the DLPC SLB provides almost no observable friction, while in contact with the SLB and allows for the collapsed SLB to quickly recover within minutes following indentation.

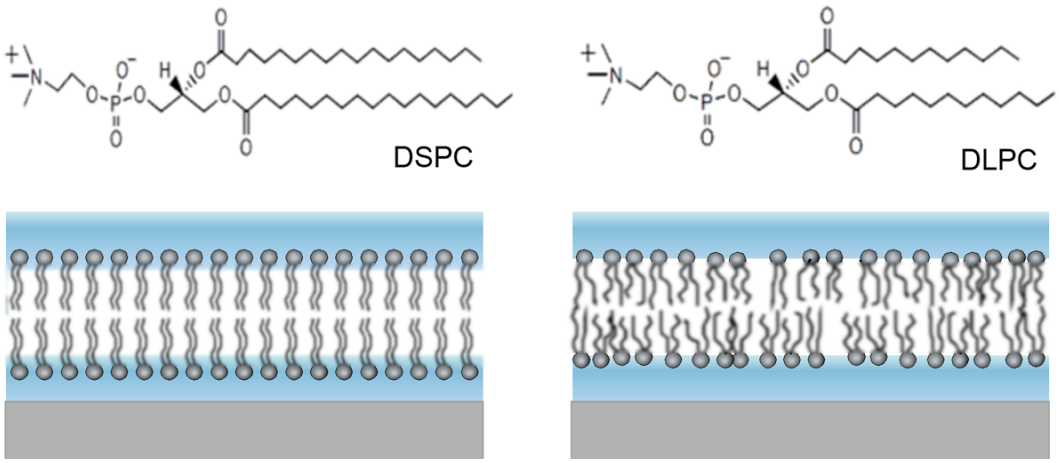

Figure 6.1 The two lipid molecules used to form the gel (left) and fluid (right) phases of supported lipid bilayers on the hydrophilic oxide terminated silicon surface.

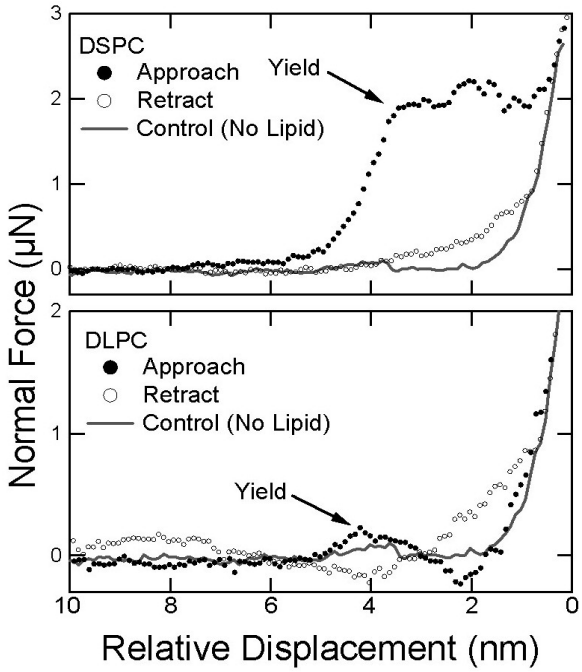

Figure 6.2 Normal force profiles during an approach(●)/ retract(○) cycle for DSPC (top) and DLPC (bottom). Approach on silicon is shown as a control (—).

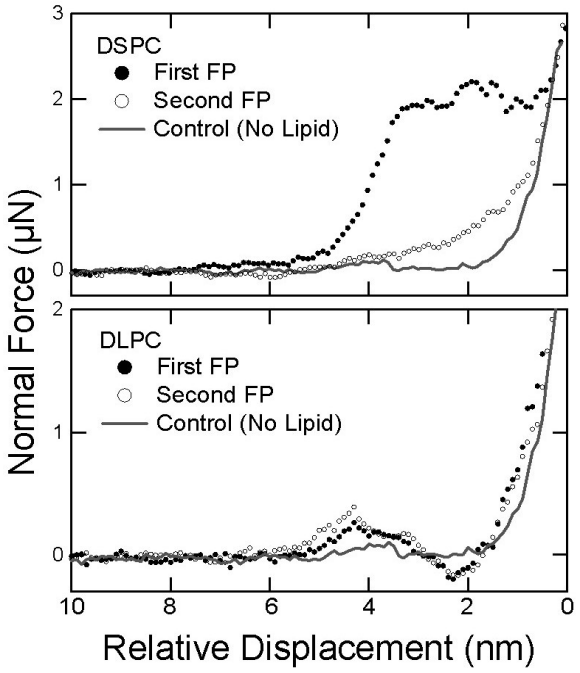

Figure 6.3 Successive approach force profiles in a single location of DSPC (top) and DLPC (bottom). Silicon is shown as a contrast in both figures (—). Significant hysteresis is observed only on DSPC.

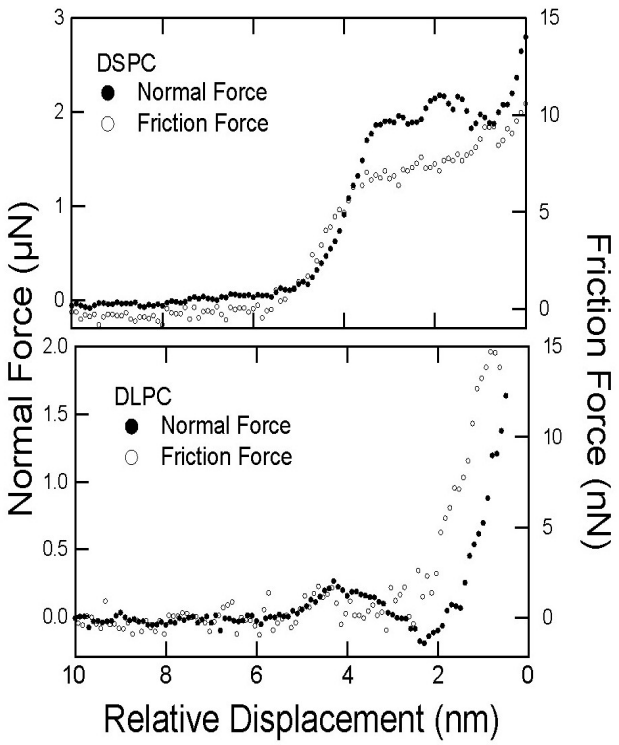

Figure 6.4 Overlay of Normal (●) and Friction (○) Force Profiles for DSPC (top) and DLPC (bottom) during approach.

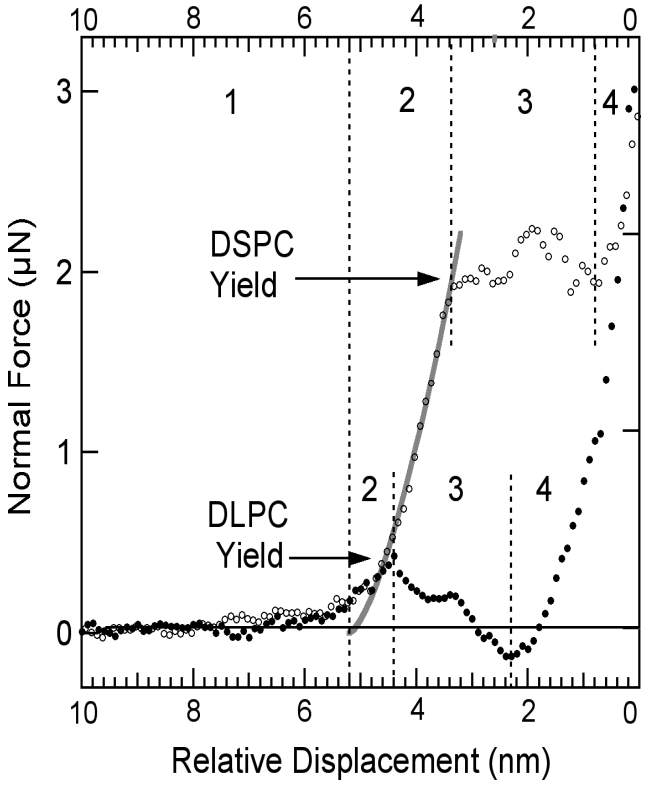

Figure 6.5 Normal force profiles for DSPC (○) and DLPC (●). Dashed lines indicate fits of force vs. displacement according to Hertz theory. Interaction regions as defined in the text are shown for both lipids.

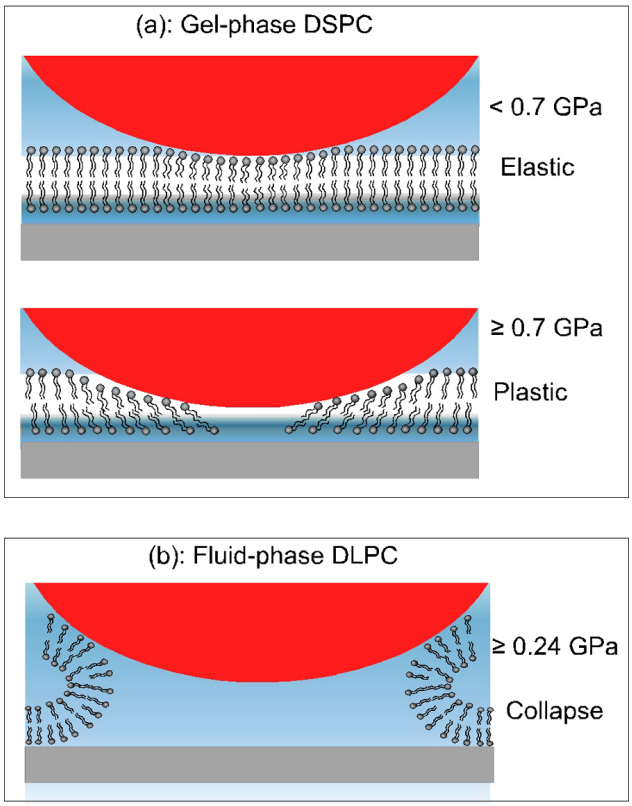

Figure 6.6 Schematic representation of the collapse of DSPC (a) and DLPC (b).

6.5 References

1. Simons, K., and W. L. C. Vaz. 2004. Model systems, lipid rafts, and cell membranes. Annu. Rev. Biophys. Biomol. Struct. 2004, 33:269.

2. Le Neveu, D. M., R. P. Rand, and V.A. Parsegian. 1979. Measurement of forces between lecithin bilayers. Nature 259:601-603.

3. Evans, E. A. 1980 Analysis of adhesion of large vesicles to surfaces. Biophysical Journal. 31:425-432.

4. Brian, A. A., and H. M. McConnell. 1984. Allogenic stimulation of cytoxic T cells by supported planar membrane. Proc. Natl. Acad. Sci. USA. 81:6159-63.

5. Binnig, G., C. F. Quate, and C. Gerber. 1986. Atomic force microscope. Phys. Rev. Lett. 56:930.

6. Butt, H.J., and A.-K. Awizio. 2006. Atomic Force Microscopy of Lipid Bilayers. In

Advances in Planar Lipid Bilayers and Liposomes, Volume 3. Leitmannova Liu, A., editor. Elsevier/North Holland, Amsterdam. 220–249.

7. Seantier, B., M.-C. Giocondi, C. Le Grimellec, and P.-E. Milhiet. 2008. Probing supported model and native membranes using AFM, Current Opinion in Colloid & Interface Science 13:326–337.

8. Butt, H.-J., B. Cappella, M. Kappl. 2005. Force measurements with the atomic force microscope: technique, interpretation and applications. Surf. Sci. Rep. 59:1-152.

9. Houston, J. E., and T. A. Michalske. 1992. The interfacial-force microscope. Nature. 356:266-267.

10. Houston, J. E., and S. A. Joyce. 1991. A new force sensor incorporating force-feedback control for interfacial force microscopy. Rev. Sci. Inst. 62-3:710-715.

11. Goertz, M. P., J. E. Houston, and X.-Y. Zhu. 2007 Hydrophilicity and the viscosity of interfacial water. Langmuir. 23:5491-5497.

12. Goertz, M. P., B. L. Stottrup, J. E. Houston, and X.-Y. Zhu. 2007. Density dependent friction of lipid monolayers. J. Phys. Chem. A. 111(49):12423-12426.

13. Briscoe, W. H., S. Tutmuss, F. Tiberg, R. K. Thomas, D. J. McGillivray, and J. Klein. 2006. Boundary lubrication under water. Nature. 444: 191-194.

14. Lin, W.-C., C. D. Blanchette, T. V. Ratta, and M. L. Longo. 2006 Lipid asymmetry in DLPC/DSPC-supported lipid bilayers: a combined AFM and fluorescence microscopy study. Biophysical Journal. 90:228-237.

15. Groves, J.T. 2007. Bending mechanics and molecular organization in biological membranes. Annu. Rev. Phys. Chem. 58:697–717.

16. Higgins, M. J., M. Polcik, T. Fukuma, J. E. Sader, Y. Nakayama, and S. P. Jarvis, 2006. Structured water layers adjacent to biological membranes. Biophysical Journal. 91:2532-2542.

17. Hertz, H. J. 1882. Uerber die berührung fester elastischer körper (in German). Reine Angew. Math. 92:156.

18. Goertz, M. P., X.-Y. Zhu, and J. E. Houston, 2008. Friction, wear, and aging of an alkoxy-monolayer boundary lubricant on silicon. Tribology Letters. 30:205-213.

19. Franz, V., S. Loi, H. Müller, E. Banber, and H.-J. Butt. 2002. Tip penetration through lipid bilayers in atomic force microscopy. Colloids and Surfaces B. 23:191-200.

Chapter 7. Friction, wear and aging of an alkoxy-monolayer boundary lubricant on silicon

7.1 Introduction

In the last decade Microelectromechanical Systems (MEMS) have transformed from tools of basic research into commercial products. As the scale of these devices continues to diminish, their levels of friction, stiction and wear become ever more important. As a result, the commercial success of MEMS has been largely limited to devices with large component separations and limited sliding contacts. Research into the details of molecular-level friction, and its associated wear, is essential for the further commercial development of these important systems (for a comprehensive review see Bhushan 2005 [1]).

One of the most common techniques for reducing friction in MEMS is the use of molecular-level boundary lubricants. Self assembled monolayers (SAMs) on Si have been widely studied because of their ease of self assembly and unique lubricating properties [2,3]. Common SAMs used for this purpose have involved attaching alkylsilanes to the native oxide of Si [4,5,6,7]. Though alkylsilanes are commonly used, their large bonding groups and tendency to polymerize when exposed to water vapor often leads to unfavorable surface reactions and poor long-term performance [8,9,10,11]. In order to mitigate the difficulties with alkylsilanes, we have studied the friction, wear and aging properties of SAMs created by attaching an alcohol (1-dodecanol) head group, to create a direct Si-O-C bond, resulting in a considerably more robust system.

Although the contacts between moving parts in MEMS devices are small, it is often found that friction obeys Amontons's "law", the empirical observation that the friction force is linearly proportional to load, i.e.,

$$F_f = \mu L . \qquad (1)$$

Here F_f is the friction force, L is the normal force (load) and μ is the friction coefficient [12]. This equation holds true for many macroscopic systems but fails to address how friction is changed by such factors as adhesion, sliding speed, roughness, stick-slip and contact area.

In the macroscopic regime, the true contact area usually involves multiple asperities and applying load increases the total contact area in direct proportion to the load giving rise to the Amonton behavior. However, smooth single asperity contacts deviate from Amontons's "law" and the friction force scales with the contact area according to Eq. 2,

$$F_f = \tau A , \qquad (2)$$

where A is the contact area and τ is the friction shear strength of the interface [12,13]. While these two equations are helpful for quantitative analysis of friction, they do not describe all observations. Using force microscopy to work at the micro or nanoscale, we can reliably create single asperity contacts and study the associated

friction. This method has been applied numerous times to study friction at surfaces that have scientific and technological importance [1,5,14,15].

In this letter we focus on the tribological properties of an alkoxy monolayer on a Si(111) surface. We explore the differences in the friction measured by (1) having a tip slide over large distances (50 nm) along the surface at a constant load and speed and (2) oscillating the tip in the lateral direction with molecular-level amplitudes (~2 nm) as the tip is brought into contact with the surface at a single location. Although the first of these measurement methods has been thoroughly studied, the results from small-range oscillatory motions are not as well characterized. Here we show considerable differences between the two results for the alkoxy monolayer, but not for a bare Si surface. We relate these differences to film deformation dynamics at the molecular level. In addition, we explore the wear resistance of the C_{12}-alkoxy monolayer through repeated long-range scanning over the same area at large applied stresses. We find evidence for film wear and a surprising reduction in the level of friction, which again, is not observed for the bare Si surface. These findings clearly show the advantage of monolayer lubricant layers designed with head-group bonding specifically tailored to the Si surface. And finally, we perform preliminary aging experiments to establish, at least for a rather limited time frame, the robustness of the alkoxy bonding.

7.2 Experimental

7.2.1 Sample Preparation

The procedure for the formation of alkoxy monolayers on Si was described in detail previously [16] and is adapted here. Briefly, Si surfaces (slices of a P-doped Si(111) wafer) were first cleaned in Piranha (3:1 conc. H_2SO_4/30% H_2O_2 Caution! Piranha is a strong oxidant and reacts violently with organic substances) for 2 hours and rinsed with copious amounts of ultra-pure (>18MΩ cm) water. Alkoxy monolayers were assembled by first removing the surface oxide with exposure to 40% $NH_4F_{(aq)}$ for 5 minutes, leaving a Si-H terminated surface. The H-Si(111) surfaces were then placed in a vacuum system and exposed to 0.5 Torr of $Cl_{2(g)}$ for 12 minutes at ~80° C, resulting in a Si-Cl terminated surface. The Cl-Si(111) samples were transferred to a glove box and immersed in a solution of 0.1M 1-docecanol in CaH_2 dried iso-octane (with .001M pyridine as a catalyst) for 16 hours at 70° C. The reaction resulted in a monolayer of Si-O-$(CH_2)_{11}CH_3$ [16], which we refer to as a C_{12}-alkoxy monolayer. The C_{12}-alkoxy covered Si surfaces were rinsed and sonicated multiple times with CH_2Cl_2 to remove loosely bound contaminates and stored in sealed test tubes until use.

7.2.2 Experimental Procedure

We performed all experiments using an Interfacial Force Microscope (IFM) [17,18] with a Berkovich style diamond tip (spherical end radius of ~400 nm) at room temperature and standard atmospheric pressure. We conducted two types of

measurements on a C_{12}-alkoxy monolayer to determine the frictional properties. In the first, we oscillated the tip with a lateral amplitude of ~2 nm (peak-to-peak), while measuring the normal force during a loading cycle and synchronously detecting the lateral force using a lock-in amplifier. This method is similar to shear modulation microcopy [19,20]. However, this method has a limited range of friction that can be measured during the load cycle, since at high loads the static friction force becomes large and the tip begins to show a stick-slip type motion which complicates data analysis. Using this method, the dissipative, or friction, component of the lateral force signal is measured in quadrature with respect to the displacement drive. In the second experiment, we measure friction from line-scan hysteresis loops over a 50 nm scan range, a method similar to friction measurement from conventional atomic force microscopy (AFM) techniques [14]. Here, the width of the hysteresis loop is proportional to the friction force. In fitting friction data taken with line-scans, we must account for the fact that the applied load changes slightly with changes in the line-scan direction. A procedure to account for this is outlined in the supporting materials. The lateral tip speed in the experiments was 50 nm/s and 62 nm/s root mean square (rms) for line-scans and lateral-oscillation, respectively. In the wear experiments, we performed 200 consecutive line-scans under a specific load at a single location and then imaged the same area at a lower load. The set of wear measurements were then periodically repeated over a period of three months, with the samples stored under ambient conditions.

7.3 Results

We first investigate friction through both force profiles with molecular-level lateral-oscillations and constant load line-scans for both supported monolayers and the bare Si control surface. Figure 7.1 shows plots of friction as a function of load for single force profiles, the first of the experimental methods. The measured friction for the C_{12}-alkoxy monolayer is significantly lower than that of the Si(111) control surface and friction is clearly not linear with applied load, consistent with a single asperity contact. The fits shown are based on Eq. 2 with the contact area calculated as discussed later in the text. Figure 7.2 shows results from the second method, individual line-scans taken at several loads for the two surfaces. An example linescan is shown in the inset of Fig. 7.2. The advantage of this technique is that we are able to probe friction at higher loads than is possible with the small-amplitude, lateral-oscillation method. Again, we observe lower friction for the C_{12}-alkoxy monolayer than for the Si control surface. The fits shown in Fig. 7.2 are detailed in the supporting materials.

In the second experiment, we investigate the stability of the SAM against wear from multiple line-scans at a single location. Figure 7.3 shows plots of loop height (proportional to friction) versus line-scan number for 200 consecutive line-scans on a C_{12}-alkoxy monolayer at loads of 2, 10 and 20 μN. We observe a decrease in friction during repeated scanning at 10 μN and 20 μN, while the friction value at 2 μN load remains nearly constant. The decrease in friction is more pronounced at the highest load and reaches a constant value after ~50 scans. As a

comparison, Fig. 7.4 shows results for similar measurements taken on bare Si. The control sample shows no observable decrease in friction over 200 line-scans. Figure 7.5 shows .1μm x .1μm images of the C_{12}-alkoxy monolayer surface before and after the wear test at 20 μN. The image was obtained at a lower load (1μN) to avoid further damage to the film. All images are taken in derivative mode to enhance topographic contrast. The image after the wear test indicates the creation of a wear track along with pile-up of the material at the edges of the track.

We repeated the wear experiments on films aged 1 and 3 months. As shown in Fig. 7.3, there is no significant difference in both the magnitude of friction and the occurrence of wear between the freshly prepared and the aged samples.

7.4 Discussion

7.4.1 Friction of the SAM

We first focus discussion on the experiment probing friction for both molecular-level oscillations and larger range line-scans. For both surfaces studied, friction is not linearly dependent upon load, justifying the use of Eq. 2 to describe the friction behavior. Since Eq. 2 describes friction per unit contact area, we must first investigate how the contact area changes with load for each sample.

We use the method outlined by Carpick et al. to determine the nature of contact [21]. This procedure can be used to determine which model of contact mechanics, if any, is appropriate to describe the contact area in relation to load and interfacial energy. The two models considered are those of Johnson-Kendall-

Roberts (JKR) and Derjaguin-Müller-Toporov (DMT) [22,23]. Both are based on Hertz contact mechanics [24], expanded to include the role of adhesion. These models represent limiting cases of forces and resulting deformations. The JKR model accounts for only contact forces that cause deformations of the tip and substrate. Alternatively, DMT theory accounts for long range forces while maintaining Hertzian contact geometry.

Note that both models assume a linearly elastic response over the entire contact range, a condition which may not be met by viscoelastic monolayer films or control surfaces. Despite the limitation of these models, they are useful in comparing similar systems and their associated properties. Carpick et at. proposed a parameter α that is used to quantify the behavior of the contact [21]. Experimentally α can be determined by fitting the friction versus load with the following equation:

$$\sqrt{F} = \sqrt{F_0}\left(\frac{\alpha + \sqrt{1-\frac{L}{L_c}}}{1+\alpha}\right)^{\frac{2}{3}} \qquad (3)$$

where F is the friction force, F_0 is the friction force at zero load, L is the load and L_C is the load at maximum adhesion. Accordingly, as α goes to 0, the DMT model describes the contact, and as α goes to 1, the JKR model is appropriate. Applying Eq. 3 to both plots of Fig. 7.1, we obtain an α parameter of ~1 for both the C_{12}-alkoxy monolayer and the Si control. This indicates that the both surfaces can be accurately modeled with JKR theory.

Having established the appropriate contact mechanics for each sample, we can characterize the amount of friction measured using both experimental methods. Fitting normal force profiles for each surface (not shown) to the JKR model gives composite modulus values of 27 GPa and 107 GPa for the C_{12}-alkoxy monolayers and Si control sample, respectively. The work of adhesions for the two surfaces are 1.72×10^{-16} J (C_{12}-alkoxy monolayer) and 1.44×10^{-15} J (Si surface). The lateral force vs. normal force data in Fig. 7.1 obtained with lateral-oscillations of the tip can be well described by Eq. 2, with the contact area given by the JKR model. These fits yield friction shear strengths of 18.5 MPa for the C_{12}-alkoxy SAM and 380 MPa for Si. Similarly, from line-scan hysteresis in Fig. 7.2 we extract the friction shear strength based on Eq. 2 and the method outlined in supporting materials. This analysis of line scans give shear strengths ranging from 45 to 62 MPa for the C_{12}-alkoxy SAM, with an average of 54 MPa, and 368 to 415 MPa for the Si control, with an average of 387 MPa. From both tip oscillation and line scan measurements, we conclude that the friction of the tip-alkoxy or tip-Si contact can be adequately described by a constant shear strength over the entire range of forces probed. The lowering of friction of Si by approximately an order of magnitude through coating with a C_{12}-alkoxy monolayer is similar to the lubrication effect of alkylsilanes on oxide-terminated Si [25,26].

The significant reduction in friction shown in Figs. 7.1 and 7.2 upon alkoxy monolayer formation clearly demonstrates the lubrication effects of molecular film. Previous studies have used AFM, IFM and the Surface Force Apparatus (SFA) to

perform similar measurements to those of Fig. 7.2 and the results showed similar lubrication effects of adsorbed monolayers [5,6,7,24,27,28]. In addition, IFM experiments have shown that friction of the interface has both chemical and mechanic contributions [29]. As a result, the reduction in friction with a monolayer lubricant is primarily from two mechanisms, i.e., the interfacial energy and energy losses inherent in the mechanical deformation of the film under tip motion.

Though there is not a simple relationship between interfacial energy (adhesion) and friction, a reduction in the inter-film bonding usually causes a reduction in friction [12,30]. In many cases, this type of friction is the result of making and breaking of interfacial bonds, giving rise to energy dissipation and friction. However, the methyl-terminated alkoxy monolayer forms no interfacial bonds with the diamond tip, other than an overall Van der Waals interaction. This is clearly indicated by the fact that the work of adhesion for the monolayer surface is reduced by ~90% (from 1.44×10^{-15} to 1.72×10^{-16} J) of that found for the Si control surface. Although it has been shown that the van der Waals force can give rise to "out-of contact" friction [31], only a very small amount of this friction is measured for the alkoxy monolayer film. Thus, for the tip-monolayer contact, the friction must result primarily from energy dissipation during the deformation of the film itself under the laterally-moving tip. The small amount of "out-of contact" friction on the hydrophilic, native oxide terminated Si control surface can be attributed to layer of adsorbed water [32] and other contaminants.

It should be noted that we obtain the work of adhesion values quoted above do not assume the JKR model for calculating these parameters from the "pull-off" force, but were obtained by integrating the adhesive portion of the force profile from the equilibrium of zero normal force to large separations in order to obtain the true work of adhesion. In contrast, fitting to the JKR model gives interfacial energies per unit contact area of 358 mJ/m^2 and 92 mJ/m^2 for the control and film surface, respectively. The deviations in the calculated work of adhesion from their actual measured values further validates previous work, which concluded that, while contact mechanics may fit force profiles quite well in the repulsive regime, it seldom provides accurate estimates for the work of adhesion [33].

The remaining mechanism for the film friction involves the details of the mechanical deformation of the film. While the two experimental approaches both show the lubricating effects of the C_{12}-alkoxy monolayer, they differ in the amount of friction measured for the lubricant, resulting from differences in the way the film is deformed. Line-scans on the C_{12}-alkoxy monolayer show a factor of ~3x higher friction shear strengths than that observed with the oscillation experiment, as summarized in Table 1. The difference is virtually absent for the Si/diamond control surface. To the authors' knowledge, this is the first study utilizing the contrast provided by these two methods to investigate the nature of friction of a lubricant.

To explain the differences in friction properties for the C_{12}-alkoxy monolayer between the two experiments, we consider, in more detail, the

deformation mechanics. In the lateral-oscillation experiment, the IFM probe is oscillated with a small sinusoidal amplitude and varying load at the same average tip position. Using this method, the sliding velocity of the interface is constantly changing and, by taking the dissipative component of the lateral force signal, we obtain the rms value of the kinetic friction. In contrast, the line-scan method measures the average kinetic friction as the probe slides across the surface. As a result, the line-scans constantly disturb new areas of the film, and the time elapsed between a particular region being successively disturbed is on the order of many seconds. In contrast, the lateral oscillations involve deforming the same overall area and a given tip location is revisited every 10ms. Thus, if the film deformation during sliding is not totally elastic, a given region may not have time to relax before the tip revisits the same area. Indeed, previous IFM studies have shown that alkanethiols on Au, another commonly studied SAM, are viscoelastic materials and thus have properties that are shear rate dependent [34]. Though a spectrum of relaxation rates was observed for these monolayers, the relaxations could be fit with a single time constant of ~80ms. Assuming that our monolayers have a similar relaxation rate, with a relaxation time of 80ms, the film will be able to relax very little if it is revisited every 10ms. Affectively, the oscillating tip produces a compressed region of the film, which expands with increasing load. This produces a kinetic friction force only as a result of repeated “rubbing” over the floor of the compressed region. Compared to an unperturbed monolayer, as probed in the line-scan experiment, the compressed film in the oscillating tip experiment permits less

energy dissipation and leads to less friction. Although the shear rate dependence of friction has been observed previously [35], our results show that, even with similar tip speeds between experimental methods, dramatic differences in friction shear strength can result from the extent of film deformation.

7.4.2 Wear of the SAM

We now focus on the wear of the C_{12}-alkoxy monolayer. Wearing of a micro/macroscale interface is commonly accompanied by an increase in friction [12]. This type of wear often results from interfacial damage and usually occurs at loads higher than used in our experiment. The wear of the C_{12}-alkoxy monolayer observed in Figs. 7.3 and 5 shows that, even though material is removed from the interface, the friction *decreases* as a result of wear. The low loads used in our experiment make it likely that the wear observed in Fig. 7.5 is only from removal and subsequent reorganization of the C_{12}-alkoxy monolayer and does not involve damage to the underlying Si. Wear plots from Fig. 7.4 and images of Si after 200 line-scans (not shown) also justify this, showing no friction change or surface damage. This type of wear has been seen before with aged alkanethiols and was attributed to a reduction in volume of the film under contact and a subsequent reordering of the residual film to a more well ordered layer [36]. A similar mechanism can explain the observation here.

As described earlier, the image of Fig. 7.5 shows that material is lost from the contact area of the line-scan and piles up at the edges resulting in a decrease in

friction. The friction reduction diminishes after ~50 scans and the virtually linear reduction rate over this region suggests that the tip removes a rather constant volume of material during each line-scan. A series of images taken every 10 scans clearly demonstrates this process, whereas, after ~50 scans the wear track does not visibly change. We also explored short-term "healing" by letting the sample sit for up to 30 minutes after completing a set of line-scans. However, the wear track remained unchanged, indicating that the wear was irreversible, at least at room temperature and over this brief period. Removal of interfacial material, and the subsequent reordering of the remaining film, has been observed in many earlier studies [37,38,39,40,41].

Figure 7.3 also shows that there is a minimum threshold stress needed to begin the wear process. Wear plots showed a decrease in friction only for loads of 10 μN and 20 μN. The calculated mean normal stresses for these two loads are 0.7 GPa and 2.3 GPa, respectively. Both of these are higher than the typical operational stress for MEMS [42]. The stress needed to wear the C_{12}-alkoxy monolayer corresponds well to the ~3.7 GPa needed to damage and wear alkanethiol monolayers [36].

7.4.3 Aging of the SAM

In order for the C_{12}-alkoxy monolayer to be reliably used as lubricants they must offer stability not only to wear, but also to aging (exposure to ambient conditions). By repeating the wear experiment for films aged up to three months

(see Fig. 7.3) there is no observable change in the friction behavior. Neither the level of friction nor the tendencies for the friction to decrease with wear changed over this period. While we only probe a limited aging time, it is clear that the stability of the film can be directly attributed to the robustness of the direct alkoxy bond of the monolayer to the Si surface.

7.5 Conclusions

We have shown that a carefully prepared C_{12}-alkoxy monolayer can act as an excellent boundary lubricant for the Si surface, even at stress levels above those normally encountered in MEMS devices. These films provide similar lubricating properties to those associated with alkylsilanes without the deposition problems and environmental sensitivity. Using the IFM, we performed two contrasting experiments to reveal insight into the nature of the friction of the lubricant. The friction of the C_{12}-alkoxy monolayer measured with large range line-scans was ~3x higher than with a molecular-level oscillation experiment. This difference is attributed to the contrast in the deformation dynamics of the monolayer film under the conditions of the two experiments. Also, through repeated scanning of the tip over the same area at elevated stress levels, we were able to wear the monolayer, but not the underlying substrate. During the wear process, we observed up to a ~50% decrease in friction over the first ~50 scans depending on the level of the load. In addition, these results indicate that wear of the film can actually improve the level of lubrication by thinning the film and increasing its molecular order. Repeating

these experiments on films aged in a laboratory environment, over a limited time, showed that the robust alkoxy-Si bond creates a film of considerable stability. We have shown that by specifically tailoring the headgroup of a monolayer, we can create a robust lubricant that effectively reduces both friction and wear of a Si surface.

7.6 Supporting Materials

When using the IFM to measure friction through line-scan hysteresis loops we must account for the fact that the IFM can only measure the total torque applied to the sensor. This torque is a combination of normal and lateral forces. When the IFM performs a normal force profile, the sensor only moves vertically, creating no torque from lateral forces (friction). Alternatively, when the sensor moves laterally, there is an additional torque created from friction. The sign of this torque is directionally dependent. Because of this, and the fact the IFM cannot separate normal and lateral contributions to the torque, the applied load changes with line-scan direction. When the sensor is moving in the one direction the force applied to the tip equals $F_n+F_f(l/d)$, where F_n is the load, F_f is the friction force, l is the length of the tip, and d is the distance of the tip from the axis of the torsion bar. When the line-scan switches direction, the force on the sensor becomes $F_n-F_f(l/d)$. Since the friction force is dependent upon the load, we can establish a method for compensating for the changing load.

When extracting friction from a line-scan, we first plot the tip vertical position versus the lateral tip position as previously described [36]. The vertical position shows how far from the average load the sensor is displaced to compensate for the addition torque from lateral forces. Using a normal force profile to get the force-displacement relationship, we then convert this plot to the total force on the sensor versus lateral tip position.

When friction is described by Eq.1, we calculate the friction coefficient, μ, though Eq. 4 at different values of average load F_n^0.

$$\mu = \left(1 - \frac{F_n^{\,0}}{F_n^{\,+}}\right)\left(\frac{d}{l}\right) \qquad (4)$$

Here F_n^+ is the maximum load while performing a line-scan in the + direction. When the line-scan changes direction the applied load switches to its minimum level, F_n^-, and Eq. 4 becomes

$$\mu = \left(1 + \frac{F_n^{\,0}}{F_n^{\,-}}\right)\left(\frac{d}{l}\right) \qquad (5)$$

In principal, these two friction coefficients should be the same.

Alternatively, when friction is described by Eq. 2, we can establish a similar method for treating linescan measurements. The contact area, A, during the linescan can be found by taking the indentation of the tip, δ, the tip radius, R, and the approximation $A=\pi R\delta$ for the contact area. This approximation is valid when

$\delta << R$, which is certainly satisfied in the present case. Similar to the method above, the friction shear strength, τ, at the maximum load and maximum indentation, δ^+, is given in Eq.6.

$$\tau = \frac{F_n^{+} - F_n^{0}}{\pi \delta^{+} R}\left(\frac{d}{l}\right) \qquad (6)$$

Again, reversing the line-scan direction to get the minimum force and minimum indentation, δ^-, should give the same friction shear strength.

$$\tau = \frac{F_n - F_n^{-}}{\pi \delta^{-} R}\left(\frac{d}{l}\right) \qquad (7)$$

For line-scan measurements shown in Fig. 7.2, the results of Eq. 6 and 7 were averaged to find the friction shear strength at each load. The result indicates that the difference in shear strength measured in either direction less than 7% of the mean.

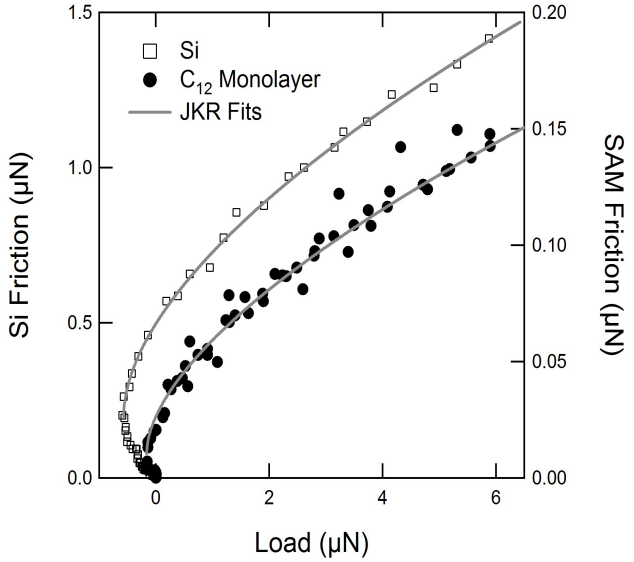

Figure 7.1 Friction force as a function of load for the C_{12}-alkoxy monolayer (●, right axis) and Si (□, left axis) control surfaces as measured using a ~2nm lateral tip oscillation. Fits of friction vs. load used Eq. 2, with the contact area as a function of load as described in text by the JKR model (solid lines).

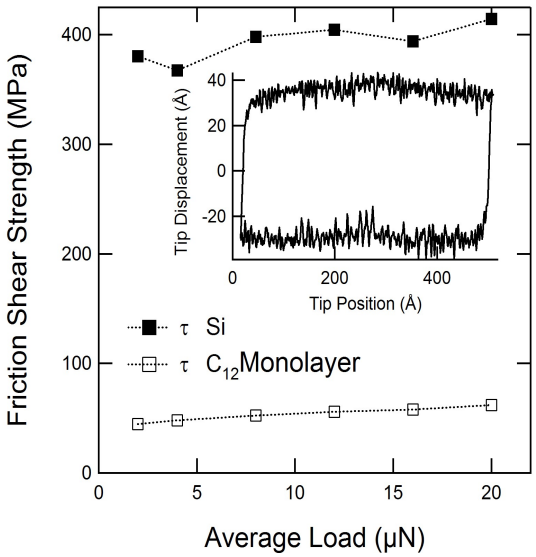

Figure 7.2 Friction shear strength as a function of average load for the C_{12}-alkoxy monolayer (□) and Si (■) as measured using 50nm line-scans. Shear strengths were calculated by averaging Eqs.6 and 7 for each load. An example line-scan hysteresis loop is shown in the inset.

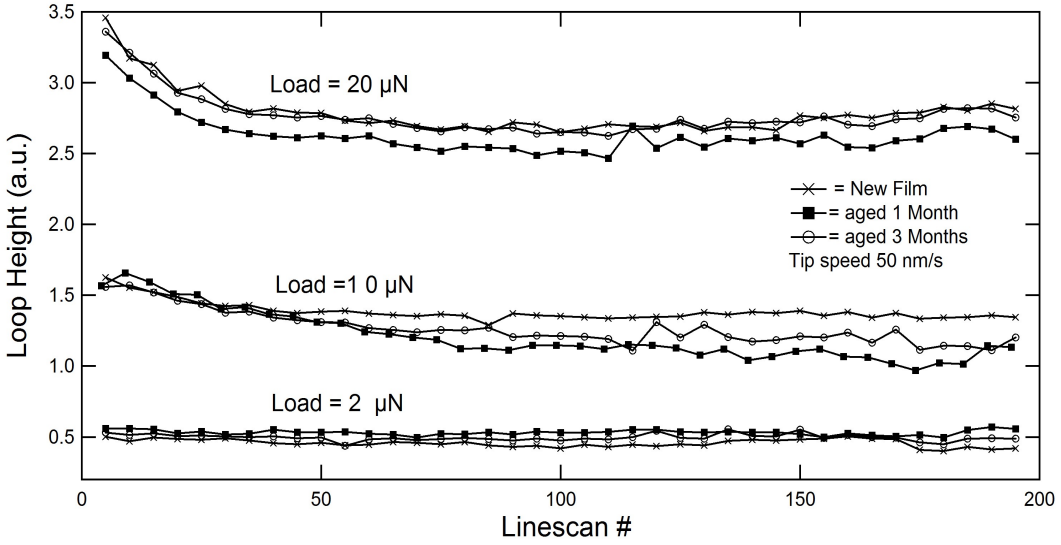

Figure 7.3 Wear plots for the C_{12}-alkoxy monolayer at 2 µN, 10 µN, and 20 µN. Line-scan loop height (friction) is plotted vs. line-scan # for 200 consecutive scans. A decrease in friction is seen during the first ~50 scans for the two highest loads. Experiments were performed on new samples (x), and films aged one (■) and three (○) months, respectively.

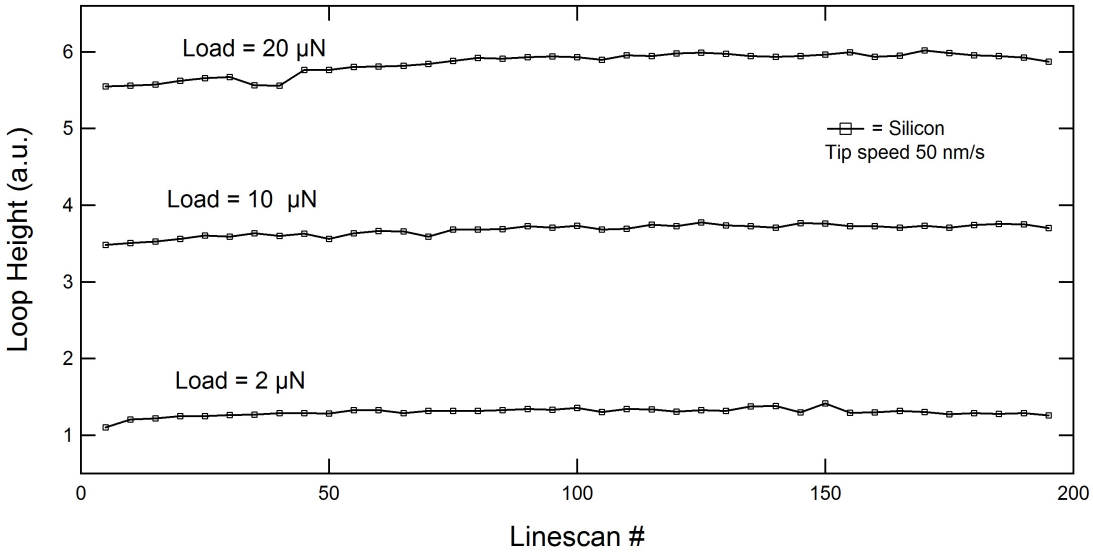

Figure 7.4 Wear plots for the Si/diamond interface at 2 µN, 10 µN, and 20 µN. Line-scan loop height (friction) is plotted vs. line-scan # for 200 consecutive scans. Virtually no change is friction is observed over the 200 scans.

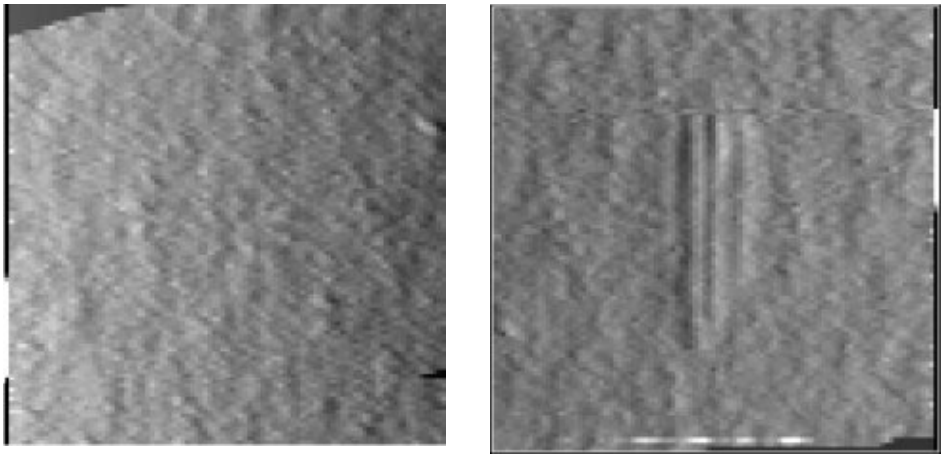

Figure 7.5 Images of a C_{12}-alkoxy monolayer before (left) and after (right) 200 line-scans taken at a normal load of 10μN. Line-scans and the associated wear tracks are ~500 Å long. Images are 0.1μM x 0.1μM and were taken at a load of 1μN . Images were taken in derivative mode to enhance the contrast of topographic features on the surface.

Surface	E* (GPa)	Work of Adhesion (J)	τ (MPa) line-scan	τ (MPa) lateral-oscillation
C_{12}-alkoxy monolayer	27	$1.72x10^{-16}$	54	18.5
Si	107	$1.44x10^{-15}$	387	380

Table 7.1 A compilation of our results for both the C_{12}-alkoxy monolayer and Si control surface as probed using the IFM and a diamond tip with a ~400nm tip radius.

7.7 References

[1] Bhushan, B.: Self-assembled monolayers for controlling adhesion, friction and wear. In Bhushan, B. Nanotribology and Nanomechanics an Introduction, Springer, Heidelberg (2005)

[2] Maboudian, R.: Surface processes in MEMS technology. Surf. Sci. Rep. 30, 207 (1998)

[3] Maboudian, R., Carraro, C.: Surface chemistry on tribology of MEMS. Ann. Rev. Phys. Chem. 55, 35 (2004)

[4] Ulman, A.: Introduction to Ultrathin Organic Films: From Langmuir-Blodgett to Self-Assembly, Academic Press, San Diego (1991)

[5] Bhushan, B.: Tribological properties of self assembled monolayers. In Bhushan, B. (ed.), Springer Handbook of Nanotechnology, Springer, Berlin, pp. 1389-1410 (2007)

[6] Liu, H., Bhushan, B.: Investigation of nanotribological properties of self-assembled monolayers with alkyl and biphenyl spacer chains. Ultramicroscopy 91, 185 (2002)

[7] Bhushan, B., Israelachvili, J.N., Landman U.: Nanotribology: friction, wear and lubrication at the atomic scale. Nature 374, 607 (1995)

[8] Cave, N.G., Kinloch, A.J.: Self-assembling monolayer silane films as adhesion promoters. Polymer 33, 1162 (1992)

[9] Gray, D.E., Casegreen, S.C., Fell, T.S., Dobson, P.J., Southern, E.M.: Ellipsometric and interferometric characterization of DNA probes immobilized on a combinatorial array. Langmuir 12, 2833 (1997)

[10] Stevens, M.J.: Thoughts on the structure of alkylsilane monolayers. Langmuir 15, 2773 (1999)

[11] Bunker, B. C., Carpick, R. W.; Assink, R. A., Thomas, M. L., Hankins, M. G., Voigt, J. A., Sipola, D., de Boer, M. P., Gulley, G. L.: The impact of solution agglomeration on the deposition of self-assembled monolayers. Langmuir 16, 7742 (2000)

[12] Bowden, F.P., Tabor, D.: The Friction and Lubrication of Solids, University Press, Oxford (2001)

[13] Persson, B.N.J.: Sliding Friction, Springer-Verlag, Berlin (2000)

[14] Carpick R.W., Salmeron, M.: Scratching the surface: fundamental investigations of tribology with atomic force microscopy. Chem. Rev. 97, 1163 (1997)

[15] Butt, H.-J., Cappella, B., Kappl, M.: Force measurements with the atomic force microscope: Technique, interpretation and applications. Surf. Sci. Rep. 59, 1-152 (2005)

[16] Zhu, X.-Y., Boiadjiev, V., Mulder, J.A., Hsung, R.P., Major, R.C.: Molecular assemblies on silicon surfaces via Si-O linkages. Langmuir 16, 6766-6772 (2000)

[17] Joyce, S.A., Houston, J.E.: A new force sensor incorporating force-feedback control for interfacial force microscopy. Rev. Sci. Instrum. 62, 710 (1991)

[18] Houston, J.E., Michalske, T.A.: The interfacial-force microscope. Nature 356, 266 (1992)

[19] Carpick, R.W., Ogletree, D.F., Salmeron, M.: Lateral stiffness: A new nanomechanical measurement for the determination of shear strengths with friction force microscopy. Appl. Phys. Lett. 70-12, 1548 (1997)

[20] Lantz, M.A., O'Shea, S.J., Hoole, A.C.F., Welland, M.E.: Lateral stiffness of the tip and tip-sample contact in frictional force microscopy. Appl. Phys. Lett. 70-8, 970 (1997)

[21] Carpick, R.W., Ogletree, D.F., Salmeron, M.J.: A general equation for fitting contact area and friction vs load measurements. J. Colloid Inter. Sci. 211, 395 (1999)

[22] Johnson, K.L., Kendall, K., Roberts, A.D.: Surface energy and the contact of elastic solids. Proc. R. Soc. London Ser. A324, 301 (1971)

[23] Derjaguin, B.V., Müller, V.M., Toporov, Y.P.: Effect of contact deformations on the adhesion of particles. J. Colloid Inter. Sci. 53, 314 (1975)

[24] Israelachvili, J.: Intermolecular & Surface Forces, Academic Press, New York (1992)

[25] Cha, K.-H., Kim, D.-E.: Investigation of the tribological behavior of octadecyltrichlorosilane deposited on silicon. Wear 251, 1169–1176 (2001)

[26] Tambe, N.S., Bhushan, B.: Nanotribological characterization of self-assembled monolayers deposited on silicon and aluminum substrates. Nanotechnology 16**,** 1549–1558 (2005)

[27] Kiely, J.D., Houston, J.E., Mulder, J.A., Hsung R.P., Zhu, X.-Y.: Adhesion, deformation and friction for self-assembled monolayers on Au and Si surfaces. Tribology Letters 7, 103–107 (1999)

[28] Major, R.C., Kim, H.I., Houston J.E., Zhu, X.-Y.: Tribological properties of alkoxyl monolayers on oxide terminated silicon. Tribology Letters 14, 237-244 (2003)

[29] Kim, H.I., Houston J.E.: Separating mechanical and chemical contributions to molecular-level friction. J. Am. Chem. Soc. 122, 12045 (2000)

[30] Yoshizawa, H., Chen, Y.-L., Israelachvili, J.: Fundamental mechanisms of interfacial friction. 1. Relation between adhesion and friction. J. Phys. Chem. 97, 4128-4140 (1993)

[31] Burns, A.R., Houston, J.E., Carpick, R.W., Michalske, T.A.: Friction and molecular deformation in the tensile regime. Phys. Rev. Lett. 82-6, 1181 (1999)

[32] Goertz, M.P., Houston, J.E., Zhu X.-Y.,: Hydophilicity and the viscosity of interfacial water. Langmuir 23, 5491-5497 (2007)

[33] Houston, J.E., Doelling, C.M., Vanderlick, T.K., Hu, Y., Scoles, G., Wenzl, I., Lee T.R.: Comparative study of the adhesion, friction, and mechanical properties of CF_3- and CH_3-terminated alkanethiol monolayers. Langmuir 21, 3926-3932 (2005)

[34] Joyce, S.A., Thomas, R.C., Houston, J.E., Michalske, T.A., Crooks, R.M.: Mechanical relaxation of organic monolayer films measured by force microscopy. Phys. Rev. Lett. 68-18, 2790 (1992)

[35] Chen, J., Ratera, I., Park, J.Y., Salmeron, M.J.: Velocity dependence of friction and hydrogen bonding Effects. Phys. Rev. Lett. 96-23, 236102 (2006)

[36] Kiely, J.D., Houston, J.E.: Contact hysteresis and friction of alkanethiol self-assembled monolayers on gold. Langmuir 15, 4513 (1999)

[37] Brewer, N.J., Beake, B.D., Leggett, G.J.: Friction force microscopy of self-assembled monolayers: Influence of adsorbate alkyl chain length, terminal group chemistry, and scan velocity. Langmuir 17, 1970 (2003)

[38] Lio, A.D., Charych, D.H., Salmeron, M.J.: Comparative atomic force microscopy study of the chain length dependence of frictional properties of alkanethiols on gold and alkylsilanes on mica. J. Phys. Chem. B 101, 3800-3805 (1997)

[39] Brewer, N.J., Foster, T.T., Leggett, G.J., Alexander, M.R., McAlpine, E.: Comparative investigations of the packing and ambient stability of self-assembled monolayers of alkanethiols on gold and silver by friction force microscopy. J. Phys. Chem. B 108, 4723-4728 (2004)

[40] Chandross, M., Webb, M.E.B., Stevens, M.J., Grest, G.S, Garofalini, S.H.: Systematic study of the effect of disorder on nanotribology of self-assembled monolayers. Phys. Rev. Lett. 93, 166103 (2003)

[41] Goertz, M.P., Stottrup, B.L., Houston, J.E., Zhu, X.-Y.: Density dependent friction in lipid monolayers. J. Phys. Chem. A 111, 12423-12426 (2007)

[42] Dugger, M.T.: Quantification of friction microsystem contacts. In Hsu, S.M., Ying, Z.C (eds.), Nanotribology Critical Assessment and Research Needs, Klower Acedemic Publishers, Boston (2003)

Chapter 8 Bibliography

Chapter 1 References

1 Houston, J.E.; Joyce,S.A. *Rev. Sci. Instrum.* **1991**, *62*, 710.

2 Houston, J.E.,; Michalske, T.A. *Nature* **1992**, *356*, 266-267.

3 Goertz, M. P; Houston J. E; Zhu, X.-Y. *Langmuir* **2007**, *23(10)*, 5491-7.

4 Bhushan, B. *Nanotribology and Nanomechanics an Introduction*; Springer: Hedidelberg, 2005.

5 Dugger, M.T.: Quantification of friction microsystem contacts. In Hsu, S.M., Ying, Z.C (eds.), Nanotribology Critical Assessment and Research Needs, Klower Acedemic Publishers, Boston (2003)

6 Crossley, A.: Johnston, C.; Watson, G.S.; Myhra, S. *Journal of Physics D-Applied Physics.* **1998,** *31*, 1955-1962.

7 Asay, D.B.; Dugger, M.T.; Kim, S.H. *Tribol. Lett*. **2008**, *29*, 67-74.

8 Brian, A.A.; McConnell, H.M.. *Proc. Natl. Acad. Sci. USA*. **1984**, *81*, 6159-63.

9 Simons, K.; Vaz. W.L.C. *Annu. Rev. Biophys. Biomol. Struct*. **2004**, *33*, 269.

10 Deng, Y.; Wang, Y.;Holtz, B.; Li, J.-Y.; Traaseth, N.; Veglia, G.; Stottrup, B.L.; Pei, D.; Elde, R.; Guo, A.; Zhu, X.-Y. *J. Am. Chem. Soc.* **2008**, *130* 6267-6271.

11 Salmeron, M. *Tribology Lett.* **2001**, *10*, 69.

12 Binnig, G.; Quate, C.F.; Gerber, C. *Phys. Rev. Lett.* **1986** *12*, 930.

13 Israelachvili, J.N. *Chemtracts* **1989**, *1*, 1.

14 Schirmeisen, A.; Anczykowski, B., Fucks, H. Scanning Probe Microscopy. In *Applied Scanning Probe Methods*. Eds. Bushan, B.; Fuchs, H.; Hosaka, S. Springer: New York, NY, 2004.

15 Israelachvili, J. N. *Intermolecular and Surface Forces*; 2nd ed.; Academic Press: San Diego, CA, 1992.

16 Persson, B. N. L. *Sliding Friction: Principles and Applications*; Springer: Berlin, 2000.

17 Bowden, F.P., Tabor, D. *The Friction and Lubrication of Solids*, University Press, Oxford , 2001.

18 Butt, H.-J., *Physics and Chemistry of Interfaces*, Wiley-VCH, Weinheim, 2006.

19 Houston, J.E.: Doelling, C.M.: Vanderlick, T.K., Hu: Y., Scoles, G.: Wenzl, I.: Lee T.R. *Langmuir* **2005**, *21*, 3926-3932.

20 Derjaguin B.V.; Muller V.M.; Toropov, Y.P., *J. Colloid. Interface Sci.* **1975**, *53*, 314.

21 Singh, S.; Houston, J.; van Swol, F.; Brinker, C.J. *Nature* **2006**, *442(*3), 526.

[22] Kim, H.I.; Kushmerick, J.G.; Houston. J.E.; Bunker B.C. *Langmuir* **2003**, *19*, 9271.

23 Feibelman, P. J. *Langmuir* **2003**, *20*, 1239-1244.

24 Hertz, H. J. *Reine Angew. Math*. **1882**, *92*, 156. (in German)

25 Johnson, K.L.; Kendall, K.; Roberts, A.D. *Proc. Roy. Soc. London* **1971**, *A 324*, 301.

26 Maugis D.J., *J. Colloid. Interface Sci*. **1992**, *150*, 243.

27 Carpick, R.W.: Ogletree, D.F.: Salmeron, M.J. *J. Colloid Inter. Sci.* **1999**, *211*, 395.

28 Chadwick, R.S. *SIAM Journal on Applied Mathematics.* **2002**, *62(5)*, 1520-1530.

29 Feibelman, P. J. *Langmuir* **2006**, *22*, 2136-2140.

Chapter 2 References

1. Bosch, R. (1996) *Method for Anisotropically Etching Silicon*. Patent No. 5501893

2. Carpick, R. W.; Salmeron, M. *Chem. Rev*. **1997**, *97*, 1163-1194

3. Binggeli, M.; Mate, C.M. *Appl. Phys. Lett*. **1994**, *65(4)*, 415.

4. Houston, J.E. J. *Polymer Sci. B.* **2005**, *43(21)*, 2993.

5. Graham, J.F.; Griffiths, M.K.; Norton, P.R.; Ogini, F.; Warrren, O.L. *J. Vac. Sci. Technol*. **1999** *A 17(4)*, 2240.

6. Xu, J.;Li, H.L. *J. Colloid. Interface Sci.* **1995**, *176*, 138.

7. Bhusan, B.: Fuchs, A.H.; Hosaka. S. In *Applied Scanning Probe Methods*; Editor: Villarrubia, J.S.; Nanoscience and Technology; Springer-Verlag: Berlin, 2004.

Chapter 3 References

1 Israelachvili, J. *Intermolecular and Surface Forces*; Academic Press: London, 1992.

2 Israelachvili, J.N.; Wennerstrom, H. *Nature* **1996**, *379*, 219.

3 Vogler, E. A. *Adv. Coll. Interface Sci***. 1998**, *71*, 69-117.

4 Crocker, J. C.; Matteo, J. A.; Dinsmore, A. D.; Yodh, A. G. *Phys. Rev. Lett.* **1999**, *82, (21),* 4352-5355.

5 Ramos, A. S. F.; Techert, S. *Biophys. Journal* **2005**, *89*, 19902003.

6 Rao, C. S.; Damodaran, S. *Colloids and Surfaces B* **2005,** *45-1*, 49-55.

7 Fenter, P.; Sturchio, N. C. *Progress in Surface Science* **2004,** *77*, 171-258.

8 Karaborni, S.; Smit, B.; Heidug, W. Urai, J. Van Oort, E. *Science* **1996**, *271*, 1102-1104.

9 Maboudian, R. *Surf. Sci. Rep*. **1998**, *30*, 207-269.

10 Jang, J.; Schaz, G. C.; Ratner, M. A. *J. Chem. Phys.* **2004**, *120*, 1157-1160.

11 Szoszkiewicz, R.; Riedo, E. *Appl. Phys. Lett*. **2005**, *87*, 033105.

12 Du, Q.; Freysz, E.; Shen, Y. R.; *Phys. Rev. Lett.* **1994**, *72,(2)*, 238-241.

13 Asay, D. B.; Kim S.H. *J.Phys. Chem. B.* **2005**, *109*, 16760-16763.

14 Yalamanchili, M. R.; Atia, A. A.; Miller, J. D. *Langmuir* **1996**, *12*, 4176-4184.

15 Bellissent-Funel, M.-E. *Eur. Phys. J. E.* **2003**, *12*, 83.

16 Hu, J.; Xiao, X.-D.; Ogletree, D.F.; Salmeron, M. *Science* **1995**, *268*, 267.

17 Vergaguer, A.; Sacha, G. M.; Bluhm, H.; Salmeron, M. *Chem. Rev.* **2006**, *106*, 1478.

18 Ju, S.-P.; Lin J.-G.; Lin J.-S.; Lin, Y.-S. *J. Chem. Phys.* **2005**, 122, 154707.

19 Gallo, P.; Rapinesi, M.; Rovere, M. *J. Chem. Phys.* **2002**, *117-1*, 369-375.

20 Iler, R.K. *The Chemistry of Silica*; Wiley; New York, 1979.

21 Leikin, S.; Parsegian, V. A.; Rau, D. C.; Rand, R. P. *Annu. Rev. Phys. Chem.* **1993**, *44*, 369.

22 Derjaguin, B. V.; Landau. L. *Acta. Physicochim.* **1941**, *14*, 633.

23 Verwey, E. J. W.; Overbeck, J. T. G. *Theory of the stability of lyophobic colloids*; Elsevier: New York, 1948.

24 Israelachvili, J. N. *J. Coll. Interf. Sci.* **110**, 263 (1986).

25 Raviv, U.; Giasson, S.; Frey, J.; Klein, J. *J. Phys. Condens. Matter* **2002**, *14*, 9275.

26 Raviv, U.; Laurat, P.; Klein, J. *Nature* **2001**, *413*, 54.

27 Binggeli, M; Mate, C.M. *Appl. Phys. Lett.* **1994**, *65*, 415.

28 Zhu, Y.; Granick, S.; *Phys. Rev. Lett*. **2001**, *87(9)*, 096104.

29 Antognozzi, M.; Humphris, A. D. L.; Miles, M. J. *Appl. Phys. Lett.* **2001**, *78*, 300.

30 Butt, H.J.; Cappella, B.; Kappl, M. *Surf. Sci. Rep*. **2005**, *59*, 1.

31 Houston, J. E.; Michalske, T. A. *Nature* **1992**, *356*, 266-267.

32 Houston, J. E.; Joyce, S. A.; *Rev. Sci. Inst*. **1991**, *62-3*, 710-715.

33 Major, R.C.; Houston, J.E.; McGrath, M.J.; Siepmann, J.I.; Zhu, X.-Y. *Phys. Rev. Lett.* **2006**, *96*, 177803.

34 Kim, H.I.; Kushmerick, J.G.; Houston. J.E.; Bunker B.C. *Langmuir* **2003**, *19*, 9271.

35 Hu, H.-W.; Carson, G. A.; Granick S. *Phys. Rev. Lett.* **1991**, *66*, 2758.

36 Douillard, J. M.; Henry, M. *J. Coll. Interface Sci.* **2003**, *263*, 554.

37 Zhu, Y.; Granick, S., *Phys. Rev. Lett.* **2001,** *87,(9)*, 096105.

38 Feibelman, P. J. *Langmuir* **2006**, *22*, 2136-2140.

39 Chan, D. Y. C.; Horn, R. G. *J. Chem. Phys.* **1985**, *83*, 5311-5324.

40 Feibelman, P. J. *Langmuir* **2003**, *20*, 1239-1244.

41 Johnson, K.L.; Kendall, K.; Roberts, A.D. *Proc. Roy. Soc. London* **1971**, *A 324*, 301.

42 Carpick, R. W.; Agrait, N.; Olgeltree, D. G.; Salmeron, M. *J. Vac. Sci, Technol., B* **1996**, *14*, 1289-1295.

43 Hertz, H. *J. Reine Angew. Math* **1882**, *92*, 156.

44 CRC Handbook of Chemistry and Physics, 79th ed.; Lide, D. R., Ed.; CRC Press: Boca Roton, Fl, 1998.

45 Lavrov, V. V. *Deformation and strength of ice*; Israel Program for Scientific Translations: Jerusalem, 1971.

46 Gilijamse, J. J.; Lock, A. J.; Bakker, H. J.; *Proc. Nat. Aced. Sci.* **2005**, *102-9*, 32020-3207.

Chapter 4 References

1. Dash, J. G. *Science* **1989**, *246*, 1591.
2. Takagi, S. *J. Colloid Interface Sci.* **1990**, *137*, 446.
3. Bluhm, H.; Ogletree, D.F.; Fadley, C.S.; Hussain, Z.; Salmeron, M. *J. Phys. Condens. Matter* **2002**, *14*, L227-L233.
4. Dosch , H.; Lied, A.; Bilgram, J. H. *Phys. Rev. Lett.* **1994**, *72*, 3534.
5. Golecki, I.; Jaccard, C. *Phys. Lett. A* **1977**, *63*, 374.
6. Elbaum, M. Lipson, S.G., Dash, J.G. *Journal of Crystal Growth* **1993**, *129*, 491-505.
7. Gilpin, R.R. *J. Colloid Interface Sci.* **1980**, *77(2)*, 435-448.
8. Wilson, P.W.; Arthur, J.W.; Haymet, A.D.J. *Biophysical Journal* **1999**, *77*, 2850-2855.
9. Doppenschmidt, A.; Kappl, M.; Butt, H.-J. *J. Phys. Chem. B* **1998,** *102*, 7813-7819.
10. Doppenschmidt. A.; Butt, J.-H. *Langmuir* **2000,** *16*, 6709-6714.
11. Petrenko, V. F. *J. Phys. Chem. B* **1997**, *101*, 6276.
12. Pittenger, B.; Fain, Jr., S. C.; Cochran, M. J.; Donev, J. M. K.; Robertson, B. E.; Szuchmacher, A.; Overney, R. M. *Phys. Rev. B* **2001**, *63*, 134102.
13. Bluhm, H,; Inoue, T.; Salmeron, M. *Phys. Rev. B* **2000**, *61*, 7760-7765.
14. Dash, J. G.; Haiying, F.; Wettlaufer, J. S. *Rep. Prog. Phys.* **1995**, *58*, 115.
15. Li, Y.; Somorjai, G. A. *J. Phys. Chem.* **2007,** *111(27)*, 9631-9637.
16. Houston, J. E.; Michalske, T. A. *Nature* **1992**, *356*, 266-267.

17. Houston, J. E.; Joyce, S. A.; *Rev. Sci. Inst*. **1991**, *62-3*, 710-715.

18. Hosler, et al. *Disc. Faraday Soc.* **1961**, *30*, 200.

19. Israelachvili, J. *Intermolecular and Surface Forces*; Academic Press: London, 1992.

20. Major, R.C.; Houston, J.E.; McGrath, M.J.; Siepmann, J.I.; Zhu, X.-Y. *Phys. Rev. Lett.* **2006**, *96*, 177803.

21. Goertz, M.; Houston, J. E.; Zhu, X.-Y. *Langmuir* **2007**, *23*, 5491-5497.

22. Feibelman, P. J. *Langmuir* **2006**, *22*, 2136-2140.

23. Hallett, J. *Proc. Phys. Soc***. 1963**, *82(530)*, 1046.

24. Jellinek, H. H. G. *Colloid Interface Sci.* **1967**, *25*, 192-205.

25. Bluhm, H,; Inoue, T.; Salmeron, M. *Phys. Rev. B* **2000**, *61(11)*, 7760-7765.

26. Weyl, W. A. *J. Coll. Sci.* **1951**, *6*, 389.

27. Rosenberg, R. *Physics Today* **2005**, *58(12)*, 50-55.

28. Bowden, F. P.; Hughes, T. P. *Proc. Roy. Soc. London A.* **1939**, *172*, 280.

29. Persson, B. N. L. *Sliding Friction: Principles and Applications*; Springer: Berlin, 2000.

30. Perrson, B. N. J.; Sivebaek, I. M.; Samoilov, V. N.; Zhao, K.; Volokitin, A. I.; Zhang, Z. *J. Phys. Condens. Matter*. **2008**, *20*, 395006.

31. Telford, J. W.; Turner, J. S. *Philos. Mag.* **1963**, *8*, 527.

32. Hosler, C. L.; Hallgren, R. E. *Disc. Faraday Soc.* **1960**, *30*, 200.

Chapter 5 References

1 Bowden F.P.; D. Tabor, D. *The Friction and Lubrication of Solids*; University Press: Oxford, 2001.

2 Bhushan, B. *Nanotribology and Nanomechanics*; Springer-Verlag: Berlin, Heidelberg, 2005.

3 Brewer, N.J.; Beake, B.D.; Leggett, G.J. *Langmuir* **2001**, *17*, 1970.

4 Lio, A. D.; H. Charych, D.H.; Salmeron M. *J. Phys. Chem. B* **1997**, *101*, 3800-3805.

5 Brewer, N.J.; Foster, T.T.; Leggett, G.L.; Alexander, M.R., McAlpine, E. *J. Phys. Chem. B* **2004**, *108*, 4723-4728.

6 Chandross, M.; Webb, M.E.B.; Stevens, M.J.; Grest. G.S.; Garofalini, S.H. *Phys. Rev. Lett.* **2003**, *93*, 166103.

7 Houston, J.E.; Doelling, C.M.; Vanderlick, T.K., Hu, Y.; Scoles, G. Wenzl, I.; Lee, T.R. *Langmuir* **2005**, *21*, 3926-3932

8 Chen, J.; Ratera, I.; Park, J.Y.; Salmeron, M. *Phys. Rev. Lett.* **2006**, *96*, 236102.

9 Gao, J. Luedtke, W.D.; Gourdon, D.; Ruths, M.; Israelachvili, J.N.; Landman, U. *J. Phys. Chem. B.* **2004**, *108(11)*, 3410.

10 Carpick, R.W.; Sasaki, D.Y.; Burns, A.R. *Tribology Letters* **1999**, *7*, 79

11 Salmeron, M. *Tribology Lett.* **2001**, *10*, 69.

12 Hills, B. A. *Proc. Inst. Mech. Eng.* **2000**, *H214*, 83–94.

13 Sarma, A. V.; Powell, G. L.; LaBerge, M. *J. Orthop. Res.* **2001**, *19*, 671–676.

14 Hornbeck, L. J. *US Patent 5602671* (1997).

15 Houston, J. E.; Michalske, T. A. *Nature* **1992**, *356*, 266-267.

16 Houston, J. E.; Joyce, S. A.; *Rev. Sci. Inst.* **1991**, *62-3*, 710-715.

17 Johnson, K. L.; Kendall, K.; Roberts, A. D. *Proc. R. Soc. London Ser. A* **1971**, *324*, 301.

18 Goertz, M. P.; Houston, J.E.; Zhu, X.-Y. *Langmuir* **2007**, *23*, 5491 - 5497.

19 Carpick, R.W.; Ogletree, D.R.; Salmeron, M.J. *J. Colloid Inter. Sci.* **1999**, *211*, 395.

20 Oncins, G.; Torrent-Burgués, J.; Sanz, F. *Tribology Letters* **2006**, *21(3)*, 175.

21 Hertz, H. *J. Reine Angew. Math* **1882**, *92*, 156.

22 Zanoni, R.; Naselli, C.; Bell, J. Stegeman, G.I.; Seaton, C.T. *Phys. Rev. Lett.* **1986**, *57(22)*, 2838.

23 Franz, V.; Loi, S.; Müller, H.; Bamberg, E.; Butt, H.-J. *Colloids and Surfaces B: Biointerfaces* **2002,** *23*, 191–200.

24 Piétrement, O.; Troyon, M. *Langmuir* **2001**, *17*, 6540-6546.

25 Du, Q.; Xiao, X.-d.; Charych, D.; Wolf, F.; Frantz, P.; Shen, Y.R., Salmeron, M. *Phys. Rev. B.* **1995**, *51(12)*, 7456.

26 Mikulsi, P.T.; Harrison, J.A. *J. Am. Chem. Soc.* **2001**, *123*, 6873-6881.

27 Siepman, J.I.; McDoland, I.R. *Phys. Rev. Lett*. **1993**, *70(4)*, 453.

28 Lee, S.; Shon, Y.-S.; Colorado, R .Jr.; Guenard, R.L. Lee, T.R.; Perry. S.S. *Langmuir* **2000,** *16*, 2220-2224.

29 Guyot-Sionnest, P. Hunt, J.H.; Shen, Y.R. *Phys. Rev. Lett.* **1987**, *59(14)*, 1597.

30 Ma, G.; Allen, H. *Langmuir* **2006**, *22*, 5341-5349

31 Behroozi, F. Langmuir **1996**, 12, 2289-2291.

32 Tshoegl, N.W. *J. Colloid Sci.* **1958**, *13*, 500-507.

Chapter 6 References

1. Simons, K., and W. L. C. Vaz. 2004. Model systems, lipid rafts, and cell membranes. Annu. Rev. Biophys. Biomol. Struct. 2004, 33:269.

2. Le Neveu, D. M., R. P. Rand, and V.A. Parsegian. 1979. Measurement of forces between lecithin bilayers. Nature 259:601-603.

3. Evans, E. A. 1980 Analysis of adhesion of large vesicles to surfaces. Biophysical Journal. 31:425-432.

4. Brian, A. A., and H. M. McConnell. 1984. Allogenic stimulation of cytoxic T cells by supported planar membrane. Proc. Natl. Acad. Sci. USA. 81:6159-63.

5. Binnig, G., C. F. Quate, and C. Gerber. 1986. Atomic force microscope. Phys. Rev. Lett. 56:930.

6. Butt, H.J., and A.-K. Awizio. 2006. Atomic Force Microscopy of Lipid Bilayers. In

Advances in Planar Lipid Bilayers and Liposomes, Volume 3. Leitmannova Liu, A., editor. Elsevier/North Holland, Amsterdam. 220–249.

7. Seantier, B., M.-C. Giocondi, C. Le Grimellec, and P.-E. Milhiet. 2008. Probing supported model and native membranes using AFM, Current Opinion in Colloid & Interface Science 13:326–337.

8. Butt, H.-J., B. Cappella, M. Kappl. 2005. Force measurements with the atomic force microscope: technique, interpretation and applications. Surf. Sci. Rep. 59:1-152.

9. Houston, J. E., and T. A. Michalske. 1992. The interfacial-force microscope. Nature. 356:266-267.

10. Houston, J. E., and S. A. Joyce. 1991. A new force sensor incorporating force-feedback control for interfacial force microscopy. Rev. Sci. Inst. 62-3:710-715.

11. Goertz, M. P., J. E. Houston, and X.-Y. Zhu. 2007 Hydrophilicity and the viscosity of interfacial water. Langmuir. 23:5491-5497.

12. Goertz, M. P., B. L. Stottrup, J. E. Houston, and X.-Y. Zhu. 2007. Density dependent friction of lipid monolayers. J. Phys. Chem. A. 111(49):12423-12426.

13. Briscoe, W. H., S. Tutmuss, F. Tiberg, R. K. Thomas, D. J. McGillivray, and J. Klein. 2006. Boundary lubrication under water. Nature. 444: 191-194.
14. Lin, W.-C., C. D. Blanchette, T. V. Ratta, and M. L. Longo. 2006 Lipid asymmetry in DLPC/DSPC-supported lipid bilayers: a combined AFM and fluorescence microscopy study. Biophysical Journal. 90:228-237.
15. Groves, J.T. 2007. Bending mechanics and molecular organization in biological membranes. Annu. Rev. Phys. Chem. 58:697–717.
16. Higgins, M. J., M. Polcik, T. Fukuma, J. E. Sader, Y. Nakayama, and S. P. Jarvis, 2006. Structured water layers adjacent to biological membranes. Biophysical Journal. 91:2532-2542.
17. Hertz, H. J. 1882. Uerber die berührung fester elastischer körper (in German). Reine Angew. Math. 92:156.
18. Goertz, M. P., X.-Y. Zhu, and J. E. Houston, 2008. Friction, wear, and aging of an alkoxy-monolayer boundary lubricant on silicon. Tribology Letters. 30:205-213.
19. Franz, V., S. Loi, H. Müller, E. Banber, and H.-J. Butt. 2002. Tip penetration through lipid bilayers in atomic force microscopy. Colloids and Surfaces B. 23:191-200.

Chapter 7 References

[1] Bhushan, B.: Self-assembled monolayers for controlling adhesion, friction and wear. In Bhushan, B. Nanotribology and Nanomechanics an Introduction, Springer, Heidelberg (2005)

[2] Maboudian, R.: Surface processes in MEMS technology. Surf. Sci. Rep. 30, 207 (1998)

[3] Maboudian, R., Carraro, C.: Surface chemistry on tribology of MEMS. Ann. Rev. Phys. Chem. 55, 35 (2004)

[4] Ulman, A.: Introduction to Ultrathin Organic Films: From Langmuir-Blodgett to Self-Assembly, Academic Press, San Diego (1991)

[5] Bhushan, B.: Tribological properties of self assembled monolayers. In Bhushan, B. (ed.), Springer Handbook of Nanotechnology, Springer, Berlin, pp. 1389-1410 (2007)

[6] Liu, H., Bhushan, B.: Investigation of nanotribological properties of self-assembled monolayers with alkyl and biphenyl spacer chains. Ultramicroscopy 91, 185 (2002)

[7] Bhushan, B., Israelachvili, J.N., Landman U.: Nanotribology: friction, wear and lubrication at the atomic scale. Nature 374, 607 (1995)

[8] Cave, N.G., Kinloch, A.J.: Self-assembling monolayer silane films as adhesion promoters. Polymer 33, 1162 (1992)

[9] Gray, D.E., Casegreen, S.C., Fell, T.S., Dobson, P.J., Southern, E.M.: Ellipsometric and interferometric characterization of DNA probes immobilized on a combinatorial array. Langmuir 12, 2833 (1997)

[10] Stevens, M.J.: Thoughts on the structure of alkylsilane monolayers. Langmuir 15, 2773 (1999)

[11] Bunker, B. C., Carpick, R. W.; Assink, R. A., Thomas, M. L., Hankins, M. G., Voigt, J. A., Sipola, D., de Boer, M. P., Gulley, G. L.: The impact of solution agglomeration on the deposition of self-assembled monolayers. Langmuir 16, 7742 (2000)

[12] Bowden, F.P., Tabor, D.: The Friction and Lubrication of Solids, University Press, Oxford (2001)

[13] Persson, B.N.J.: Sliding Friction, Springer-Verlag, Berlin (2000)

[14] Carpick R.W., Salmeron, M.: Scratching the surface: fundamental investigations of tribology with atomic force microscopy. Chem. Rev. 97, 1163 (1997)

[15] Butt, H.-J., Cappella, B., Kappl, M.: Force measurements with the atomic force microscope: Technique, interpretation and applications. Surf. Sci. Rep. 59, 1-152 (2005)

[16] Zhu, X.-Y., Boiadjiev, V., Mulder, J.A., Hsung, R.P., Major, R.C.: Molecular assemblies on silicon surfaces via Si-O linkages. Langmuir 16, 6766-6772 (2000)

[17] Joyce, S.A., Houston, J.E.: A new force sensor incorporating force-feedback control for interfacial force microscopy. Rev. Sci. Instrum. 62, 710 (1991)

[18] Houston, J.E., Michalske, T.A.: The interfacial-force microscope. Nature 356, 266 (1992)

[19] Carpick, R.W., Ogletree, D.F., Salmeron, M.: Lateral stiffness: A new nanomechanical measurement for the determination of shear strengths with friction force microscopy. Appl. Phys. Lett. 70-12, 1548 (1997)

[20] Lantz, M.A., O'Shea, S.J., Hoole, A.C.F., Welland, M.E.: Lateral stiffness of the tip and tip-sample contact in frictional force microscopy. Appl. Phys. Lett. 70-8, 970 (1997)

[21] Carpick, R.W., Ogletree, D.F., Salmeron, M.J.: A general equation for fitting contact area and friction vs load measurements. J. Colloid Inter. Sci. 211, 395 (1999)

[22] Johnson, K.L., Kendall, K., Roberts, A.D.: Surface energy and the contact of elastic solids. Proc. R. Soc. London Ser. A324, 301 (1971)

[23] Derjaguin, B.V., Müller, V.M., Toporov, Y.P.: Effect of contact deformations on the adhesion of particles. J. Colloid Inter. Sci. 53, 314 (1975)

[24] Israelachvili, J.: Intermolecular & Surface Forces, Academic Press, New York (1992)

[25] Cha, K.-H., Kim, D.-E.: Investigation of the tribological behavior of octadecyltrichlorosilane deposited on silicon. Wear 251, 1169–1176 (2001)

[26] Tambe, N.S., Bhushan, B.: Nanotribological characterization of self-assembled monolayers deposited on silicon and aluminum substrates. Nanotechnology 16**,** 1549–1558 (2005)

[27] Kiely, J.D., Houston, J.E., Mulder, J.A., Hsung R.P., Zhu, X.-Y.: Adhesion, deformation and friction for self-assembled monolayers on Au and Si surfaces. Tribology Letters 7, 103–107 (1999)

[28] Major, R.C., Kim, H.I., Houston J.E., Zhu, X.-Y.: Tribological properties of alkoxyl monolayers on oxide terminated silicon. Tribology Letters 14, 237-244 (2003)

[29] Kim, H.I., Houston J.E.: Separating mechanical and chemical contributions to molecular-level friction. J. Am. Chem. Soc. 122, 12045 (2000)

[30] Yoshizawa, H., Chen, Y.-L., Israelachvili, J.: Fundamental mechanisms of interfacial friction. 1. Relation between adhesion and friction. J. Phys. Chem. 97, 4128-4140 (1993)

[31] Burns, A.R., Houston, J.E., Carpick, R.W., Michalske, T.A.: Friction and molecular deformation in the tensile regime. Phys. Rev. Lett. 82-6, 1181 (1999)

[32] Goertz, M.P., Houston, J.E., Zhu X.-Y.,: Hydophilicity and the viscosity of interfacial water. Langmuir 23, 5491-5497 (2007)

[33] Houston, J.E., Doelling, C.M., Vanderlick, T.K., Hu, Y., Scoles, G., Wenzl, I., Lee T.R.: Comparative study of the adhesion, friction, and mechanical properties of CF_3- and CH_3-terminated alkanethiol monolayers. Langmuir 21, 3926-3932 (2005)

[34] Joyce, S.A., Thomas, R.C., Houston, J.E., Michalske, T.A., Crooks, R.M.: Mechanical relaxation of organic monolayer films measured by force microscopy. Phys. Rev. Lett. 68-18, 2790 (1992)

[35] Chen, J., Ratera, I., Park, J.Y., Salmeron, M.J.: Velocity dependence of friction and hydrogen bonding Effects. Phys. Rev. Lett. 96-23, 236102 (2006)

[36] Kiely, J.D., Houston, J.E.: Contact hysteresis and friction of alkanethiol self-assembled monolayers on gold. Langmuir 15, 4513 (1999)

[37] Brewer, N.J., Beake, B.D., Leggett, G.J.: Friction force microscopy of self-assembled monolayers: Influence of adsorbate alkyl chain length, terminal group chemistry, and scan velocity. Langmuir 17, 1970 (2003)

[38] Lio, A.D., Charych, D.H., Salmeron, M.J.: Comparative atomic force microscopy study of the chain length dependence of frictional properties of alkanethiols on gold and alkylsilanes on mica. J. Phys. Chem. B 101, 3800-3805 (1997)

[39] Brewer, N.J., Foster, T.T., Leggett, G.J., Alexander, M.R., McAlpine, E.: Comparative investigations of the packing and ambient stability of self-assembled monolayers of alkanethiols on gold and silver by friction force microscopy. J. Phys. Chem. B 108, 4723-4728 (2004)

[40] Chandross, M., Webb, M.E.B., Stevens, M.J., Grest, G.S, Garofalini, S.H.: Systematic study of the effect of disorder on nanotribology of self-assembled monolayers. Phys. Rev. Lett. 93, 166103 (2003)

[41] Goertz, M.P., Stottrup, B.L., Houston, J.E., Zhu, X.-Y.: Density dependent friction in lipid monolayers. J. Phys. Chem. A 111, 12423-12426 (2007)

[42] Dugger, M.T.: Quantification of friction microsystem contacts. In Hsu, S.M., Ying, Z.C (eds.), Nanotribology Critical Assessment and Research Needs, Klower Acedemic Publishers, Boston (2003)